

國立交通大學

光電工程研究所

博士論文

硒化鎵晶體中遠紅外波段的光學性質與應用



A study of optical properties and application of GaSe crystal in the  
mid- and far-infrared

研究生：陳晉瑋

指導教授：潘犀靈 教授

中華民國九十七年六月

碲化鎘晶體中遠紅外波段的光學性質與應用

A study of optical properties and application of GaSe crystal in the mid- and far-infrared

研究生：陳晉瑋

Student : Ching-Wei Chen

指導教授：潘犀靈 教授

Advisor : Prof. Ci-Ling Pan



Submitted to Department of Photonics &  
Institute of Electro-Optical Engineering  
College of Electrical Engineering  
National Chiao Tung University  
In partial Fulfillment of the Requirements  
for the Degree of  
Doctor of Philosophy  
in  
Electro-Optical Engineering

June 2008

Hsinchu, Taiwan, Republic of China  
中華民國九十七年六月

# 硒化鎵晶體中遠紅外波段的光學性質與應用

研究生：陳晉璋

指導教授：潘犀靈 教授

國立交通大學光電工程研究所

## 摘要

在本論文中，主要重點在探討由實驗室自製的高品質硒化鎵單晶於中遠紅外光波段範圍的光學性質與應用。利用硒化鎵晶體其高非線性的特質與低吸收係數的特性來結合非線性光學的過程來產生同調的光源。首先，利用傅利葉變換紅外光譜儀(FTIR)與兆赫時域光譜儀(THz-TDS)來研究硒化鎵晶體於此寬波段的光學性質。並針對實驗數據的擬合提出硒化鎵晶體於此波段的常態與非常態介電函數修正方程式。對於晶體在高吸收區域，也以實驗檢視出橫向與縱向聲子振動模態分別為6.39 and 7.62 THz。此外，於兆赫波段的一個位於0.586 THz的低頻聲子模態，可進一步確認硒化鎵晶體為 $\epsilon$ 型式的晶相。我們也針對Sellmeier方程式提出了修正的參數，並能夠有效地描述晶體的色散特性。在本研究中所提出硒化鎵晶體的介電函數修正方程式能利用於兆赫波段實際光學組件的應用設計。

近一步，我們利用此材料良好的性質並結合非線性光學中差頻的技術來產生同調的紅外光源輸出，其可調範圍從2.4到28  $\mu\text{m}$ 。而237.0  $\text{cm}^{-1}$  和 213.5  $\text{cm}^{-1}$ 兩個紅外波段的吸收聲子模態也和光色散性質相互關聯。而Sellmeier方程式常態與非常態折射率的兩個吸收峰的波長分別為42.2  $\mu\text{m}$ 和46.8  $\mu\text{m}$ 。其中，常態色散的吸收峰符合於紅外聲子模態的E'對稱，並反應出硒化鎵晶體內鎵原子與硒原子於鍵結平面上的交互振盪。另一方面，Sellmeier方程式非常態色散的吸收峰符合於紅外聲子模態的A<sub>2</sub>'對稱，並反應出硒化鎵晶體內鎵原子與硒原子於光軸上垂直方向的交互振盪。另外，我們並完成了利用硒化鎵晶體產生同調紅外光源時，光學吸收特性對輸出特性所造成的影響。輸出範圍從紅外光至兆赫輻射波段的同調光源，其輸出功率的變化和此非線性差頻過程的增益相關，並且和硒化鎵晶體本身的吸收係數也有關聯。而吸收係數對差頻過程所造成的影響，進一步可利用在硒化鎵晶體內微量摻雜鉕原子來做部分地補償。

接著，我們在實驗與理論上提出利用多級的光整流技術於硒化鎵晶體中產生同調的兆赫輻射光源，利用精確地調控兩級中激發光源的時間延遲，可將來自硒化鎵晶體中產生的第二級兆赫輻射，同調疊加於第一級兆赫輻射光場。此兩級之間的高同調特性證實了光整流的同調過程，並可應用於兆赫輻射的光譜調控技術。此多級的光整流技術不但可以克服晶體長度與群速度色散的限制，此技術亦有發展高功率兆赫輻射光

源輸出的潛力。並在此研究中進一步討論雙光子吸收所產生的自由載子對兆赫輻射輸出的影響，並定量計算出兆赫輻射於硒化鎵晶體中的非線性吸收截面係數 $\sigma_{THz}$ ，其估計範圍為 $(1.3-5.9)\times 10^{-17} \text{ cm}^2$ 。

我們也架設了一套由高功率飛秒雷射聚焦游離空氣產生電漿，以空氣的三階非線性係數滿足四波混頻的兆赫輻射產生源。改變雷射基頻及二倍頻間的相位差、偏振方向夾角以及量測進入BBO晶體之前激發光源與產生兆赫輻射強度之間的功率相依關係，來量測以此方法所產生兆赫輻射的特性。此外，硒化鎵晶體為產生高功率兆赫輻射的良好非線性介質，並利用來做兆赫輻射光參數放大的研究。本研究中，實驗上證實了兆赫輻射的放大現象，初步結果顯示中心頻率於1 THz的兆赫輻射經過此光參數放大器後有2.7倍的功率增益。此技術提供了一個方法來提昇兆赫輻射的電場強度以利用於未來兆赫輻射非線性光譜學的應用。



# A study of optical properties and application of GaSe crystal in the mid- and far-infrared

Student: Ching-Wei Chen

Advisor: Prof. Ci-Ling Pan

Institute of Electro-Optical Engineering  
College of Electrical Engineering and Computer Science  
National Chiao Tung University

## Abstract

In this dissertation, the optical properties and applications of high quality, home-made GaSe single crystals are investigated in the mid- to far-infrared ranges. The major part of this study is focused on the coherent light generation by means of the nonlinear optical processes associated with the GaSe crystal, which possesses the promising characteristics including high nonlinearity and low absorption properties. First, the optical constants of a GaSe crystal are measured by the Fourier-transform infrared spectrometer (FTIR) and terahertz time-domain spectroscopy (THz-TDS) in a wide frequency range. Based on experimental data, a modified complex ordinary and extraordinary dielectric function of GaSe is presented. The transverse and longitudinal optical phonons in the reststrahlen band for the ordinary refraction index are experimentally determined to be 6.39 and 7.62 THz, respectively. Besides, a low-frequency rigid-layer phonon mode at 0.586 THz confirms the pure GaSe crystal to be in the  $\epsilon$ -phase. Furthermore, the revised parameters of Sellmeier equation, which is expressed in an empirical formula form and that effectively describes the dispersion of this GaSe crystal, is also reported. The proposed dielectric functions of the  $\epsilon$ -GaSe crystal in this study are applicable to practical photonic devices at terahertz frequencies.

Moreover, we apply this promising material for the generation of coherent infrared radiation widely tunable from 2.4 to 28  $\mu\text{m}$  through difference-frequency generation (DFG). The infrared-active modes of  $\epsilon$ -GaSe crystal at 237.0  $\text{cm}^{-1}$  and 213.5  $\text{cm}^{-1}$  were found to be

responsible for the observed optical dispersion and infrared absorption edge. The poles of the modified Sellmeier equations occur at 42.2  $\mu\text{m}$  for the e-ray and 46.8  $\mu\text{m}$  for the o-ray, respectively. The pole of the o-ray dispersion corresponds to an infrared active mode of  $E'$ -symmetry with vibration involving both Ga and Se atoms on the basal plane of GaSe crystal. The pole of the e-ray dispersion corresponds to an infrared active mode of  $A_2''$ -symmetry with vibration involving both Ga and Se atoms along the optical axis (c-axis). We perform a study of the effect of optical absorption on generation of coherent infrared radiation from mid-IR to THz region from GaSe crystal. The output power variation with wavelength can be properly explained with the spectral shape of parametric gain and absorption coefficient of GaSe. The adverse effect of infrared absorption on DFG process can partially be compensated by doping GaSe crystal with erbium ions.

Subsequently, we propose and experimentally demonstrate the generation of single-cycle terahertz radiation with two-stage optical rectification in GaSe crystals. By adjusting the time delay between the pump pulses employed to excite the two stages, the terahertz radiation from the second GaSe crystal can constructively superpose with the seeding terahertz field from the first stage. The high mutual coherence between the two terahertz radiation fields is ensured with the coherent optical rectification process and can be further used to synthesize a desired spectral profile of output coherent THz radiation. The technique is also useful for generating high amplitude single-cycle terahertz pulses, not limited by the pulse walk-off effect from group velocity mismatch in the nonlinear optical crystal used. In addition, free carriers induced nonlinear absorption of THz radiation is also investigated in this study. The absorption cross-section,  $\sigma_{THz}$ , of GaSe at terahertz frequency in the presence of free carriers are estimated in the range of  $(1.3 - 5.9) \times 10^{-17} \text{ cm}^2$ .

Specially, femtosecond laser induced plasma in ambient air based on the third order nonlinearity is employed to construct a THz-TDS system in this study. The properties of the THz radiation from this configuration are characterized by altering the phase shift, the angle between polarizations of the fundamental and second harmonic beams. The dependence of the THz signal as a function of the fundamental pulse energy before the BBO crystal is also examined. Furthermore, GaSe crystal is a promising nonlinear optical medium to perform the generation of intense THz radiation. Herein, we report the experimental demonstration of terahertz wave amplification in GaSe crystal. Terahertz power amplification factor of about 2.7 times is preliminarily performed under the phase matching condition around 1 THz. The demonstration provides a potential way to further increase the terahertz electric field for nonlinear spectroscopic applications with a desktop femtosecond laser system.



# Acknowledgement

本研究論文的完成，也意味著我博士生涯告一段落，在這多年的研究與求學過程中，得到太多人的提攜與幫忙，在此獻上我深深的感謝之意：首先，要感謝我的指導教授潘犀靈教授，由於您當年的提攜，讓我有這個機會進入光電的奧妙領域，謝謝您多年來提供我研究上的資源與設備，且您對研究品質的堅持與細心更是影響我甚巨，在此，我由衷地感謝您。再來，我要感謝多年來在研究領域中給予我諸多指導與方向的黃中壺教授，您對實驗技術與數據的動悉能力和對物理的敏感度，更是讓我打從心裡地佩服，學生我在此對您獻上最高的敬意。在我的實驗過程裡，我最要感謝張振雄教授與徐裕奎學長，謝謝你們實驗室提供我研究的硒化鎵晶體，愉快的合作經驗與實驗討論過程，更是讓我受益良多。另外，要感謝張景園教授在我博士班中期，在光參數放大與差頻技術的實驗觀念上給予我的教導，謝謝您提供多元的研究點子與討論的對象。特別要感謝客座教授嚴立教授在我博士班後期的合作與討論，讓我在光學理論與多級光整流實驗上有進一步的認知。另外，我要感謝實驗上合作者顏順通教授與鐘佩鋼學弟，提供我傅利葉變換紅外光譜儀系統與量測技術。謝謝實驗室的安惠榮教授，平時對我實驗上的建議與生活上的鼓勵。感謝李晁達教授在我博士班後期，生活在高雄的那段時間，提供我實驗上的設備，讓我實驗能夠更加地順利完成。這本論文在最後階段能順利完成，要特別感謝我的口試委員：孔慶昌教授、黃衍介教授、趙如蘋教授、謝文峰教授的指導，謝謝你們的建議與指教，讓我對未來的路途更具信心，也更虛心地了解到需要再多加地充實自我的能力。

當然我要感謝多年來和我一起完成眾多實驗成果的學長與學弟妹們，有你們的陪同，讓我在這求學路途中不再孤單；感謝劉子安學長教導我架設超快雷射的相關技術；感謝王怡超同學多年來於課業與實驗上的討論與協助；感謝黃龍進學弟於光參數放大理論與實驗上的共同努力；感謝江文智學弟於新型基因演算法程式上的討論與幫忙；感謝許乃今學妹於奈米晶體實驗上的共同努力完成；感謝許哲睿學弟於兆赫輻射光參數放大的全力幫忙與協助；感謝林育賢學弟於多級光整流實驗與理論計算上的協助；感謝湯宗達、謝卓帆、林家任學弟們於兆赫時域光譜儀實驗與程式上的幫忙；感謝林松輝學弟於傅利葉變換紅外光譜理論程式分析上的大力協助；同時也感謝歷屆學弟妹們在研究上的經驗分享與課餘時間的相互照顧。接著，我要對我的好友們致上謝意，感謝你們在我博士班多年來的過程中生活上的參與，有你們的日子真的很溫馨很快樂，在我無助時得到支持，在我失意時得到鼓勵，在我快樂時有你們分享，謝謝你們：富美、秉其、建勳、志偉、倩如、冠文、志成、淑惠、材俊、惠鄉。有你們陪伴的日子，讓我的博士求學生涯更多采多姿，也顯得更有意義。

最後，僅將我這個小小的榮耀獻給我最愛的家人：爸爸、媽媽，你們的期待與體諒，是支持我繼續走下去的動力，感謝你們多年來的培育，我目前擁有的這一切是您們的功勞，深深地感謝你們！特別感謝姐姐與姐夫和眾多的親朋好友們的鼓勵與關愛，我會繼續再努力加油的。相信此時，不是終點，而是另一個階段的起點，我會在未來的人生路途上為您們帶來更多的驚喜與光采！

晉瑋 於 新竹交通大學 2008年6月

## Contents Page

|  |            |
|--|------------|
| <b>Abstract (Chinese)</b> .....  | <b>i</b>   |
| <b>Abstract (English)</b> .....  | <b>iii</b> |
| <b>Acknowledgement</b> .....   | <b>v</b>   |
| <b>Contents</b> .....  | <b>vi</b>  |
| <b>List of Figures</b> .....   | <b>x</b>   |
| <b>List of Tables</b> .....  | <b>xiv</b> |
| <b>Chapter 1 Introduction</b> .....  | <b>1</b>   |
| 1.1 Background .....   | 1          |
| 1.2 Motivation .....   | 5          |
| 1.3 Organization of thesis .....   | 6          |
| References .....   | 8          |
| <b>Chapter 2 Overview of the radiation light sources of mid-infrared to far-infrared (terahertz)</b> ..... | <b>10</b>  |
| 2.1 Introduction .....   | 10         |
| 2.2 Overview of coherent mid-infrared generation .....   | 13         |
| 2.3 Overview of coherent terahertz generation and detection .....  | 17         |
| 2.3.1 Generation by photoconductive antenna .....  | 17         |
| 2.3.2 Generation by optical rectification .....  | 19         |
| 2.3.3 Generation by laser induced plasma .....   | 20         |
| 2.3.4 Detection by photoconductive antenna .....   | 22         |



|   |           |
|---|-----------|
| 2.3.5 Detection by electro-optical sampling .....   | 22        |
| References .....  | 26        |
| <b>Chapter 3 Optical properties and potential applications of <math>\epsilon</math>-GaSe crystal in terahertz frequencies .....</b> | <b>30</b> |
| 3.1 Introduction .....  | 30        |
| 3.2 Sample preparation and experimental method .....  | 31        |
| 3.3 Analysis model of optical constant from THz-TDS .....   | 32        |
| 3.4 Results and Discussions .....   | 34        |
| 3.4.1 Raman spectroscopy .....  | 34        |
| 3.4.2 Optical constant measurement by THz-TDS .....   | 35        |
| 3.4.3 Optical properties measurement by transmitted FTIR .....  | 38        |
| 3.4.4 Optical properties measurement by reflected FTIR .....  | 39        |
| 3.4.5 Ordinary and extraordinary dielectric function determination .....  | 40        |
| 3.4.6 Sellmeier equations determination .....   | 44        |
| 3.4.7 Potential application of GaSe in terahertz frequencies .....  | 46        |
| 3.5 Summary .....   | 47        |
| References .....  | 49        |
| <b>Chapter 4 Generation properties of coherent infrared radiation in the optical absorption region of GaSe crystal .....</b>        | <b>52</b> |
| 4.1 Introduction .....  | 52        |
| 4.2 Experimental methods .....  | 53        |
| 4.3 Results and Discussions .....   | 56        |

|  |           |
|--|-----------|
| 4.3.1 Optical properties of pure and Erbium doped GaSe crystals measured by transmitted type FTIR and THz-TDS .....                    | 56        |
| 4.3.2 Effective nonlinear coefficient ( $d_{eff}$ ) determined by SHG .....  | 58        |
| 4.3.3 Picosecond mid-infrared generation by difference frequency mixing .....  | 60        |
| 4.3.4 Sellmeier equations determination .....  | 61        |
| 4.3.5 Relation between infrared absorption edge and optical dispersion .....   | 63        |
| 4.3.6 Parametric gain and output power calculation .....   | 66        |
| 4.4 Summary .....  | 68        |
| References .....   | 69        |
| <b>Chapter 5 Coherent generation and spectral synthesis of terahertz radiation with multiple stages of optical rectification .....</b> | <b>72</b> |
| 5.1 Introduction .....   | 72        |
| 5.2 Theoretical model and experimental method .....  | 73        |
| 5.3 Results and Discussions .....  | 75        |
| 5.3.1 THz generation by optical rectification with azimuthal $\phi$ angle dependence .....   | 75        |
| 5.3.2 High coherence between multiple stages of optical rectification .....  | 76        |
| 5.3.3 THz coherent superposition and spectral synthesis by multiple stages of optical rectification .....                              | 77        |
| 5.3.4 Nonlinear absorption of THz wave in GaSe crystal .....   | 82        |
| 5.3.5 Pump power and absorption dependence of the THz wave output .....  | 84        |
| 5.4 Summary .....  | 86        |
| References .....   | 87        |

|  |            |
|--|------------|
| <b>Chapter 6 The study of THz optical parametric amplification in <math>\epsilon</math>-GaSe crystal .....</b> | <b>89</b>  |
| 6.1 Introduction .....   | 89         |
| 6.2 Theoretical model and experimental method .....  | 92         |
| 6.2.1 The principle of OPA process .....   | 92         |
| 6.2.2 Satisfactory phase matching condition .....  | 94         |
| 6.2.3 Experimental setup .....   | 95         |
| 6.3 Results and Discussions .....  | 98         |
| 6.3.1 The characteristic of THz generation by laser induced plasma by four wave mixing .....                   | 98         |
| 6.3.2 GaSe crystal length determination by GVM .....   | 101        |
| 6.3.3 Pump depleted gain prediction by taking account of the linear and nonlinear absorption .....             | 101        |
| 6.3.4 THz amplification experimental achievement .....   | 103        |
| 6.4 Summary .....  | 104        |
| References .....   | 105        |
| <b>Chapter 7 Conclusions and future works .....</b>  | <b>107</b> |

## List of Figures Page

### Chapter 1

|                 |   |   |
|-----------------|---|---|
| <b>Fig. 1-1</b> | Layer structure of $\epsilon$ -GaSe crystal .....   | 2 |
| <b>Fig. 1-2</b> | Absorption coefficients versus wavelength for several nonlinear crystals, some of which were frequently used for terahertz generation. The absorption spectrum for CdSe available covers a narrow wavelength range of 63–71 $\mu\text{m}$ ..... | 4 |
| <b>Fig. 1-3</b> | A cleaved surface of the as-grown $\epsilon$ -GaSe crystal .....  | 5 |

### Chapter 2

|                 |  |    |
|-----------------|--|----|
| <b>Fig. 2-1</b> | Overview of frequency regions .....  | 11 |
| <b>Fig. 2-2</b> | Generated frequency ranges for several NLO crystals in mid-infrared generation .....   | 17 |
| <b>Fig. 2-3</b> | Schematic of PC antenna .....  | 18 |
| <b>Fig. 2-4</b> | Illustration of terahertz radiation by optical rectification .....   | 19 |
| <b>Fig. 2-5</b> | Schematic of the THz generation via four-wave mixing in a plasma. The pulse at the fundamental contains wavelengths between 770 and 830 nm, the second harmonic between 385 and 415 nm ..... | 21 |
| <b>Fig. 2-6</b> | The scheme of EO sampling setup .....  | 23 |
| <b>Fig. 2-7</b> | Angles of the THz wave and probe beam polarization directions .....  | 25 |

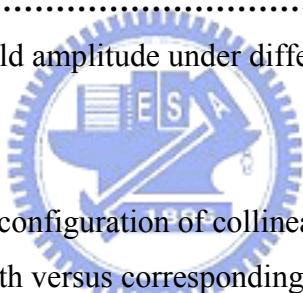
### Chapter 3

|                 |   |    |
|-----------------|---|----|
| <b>Fig. 3-1</b> | A general sketch of the home-made terahertz time-domain spectroscopy (THz-TDS) system. Laser source : Ti: sapphire femtosecond laser with wavelength~800nm; Repetition rate~82MHz; Pulse duration~50fs; THz emitter and detector : LT- GaAs photoconductive antenna with Si lens .... | 32 |
|-----------------|---|----|

|                  |   |           |
|------------------|---|-----------|
| <b>Fig. 3-2</b>  | A general sketch of the (a) reference-purged N <sub>2</sub> and (b) sample-GaSe crystal for the optical constants measurement in the terahertz time-domain spectroscopy (THz-TDS) experiment .....  | <b>33</b> |
| <b>Fig. 3-3</b>  | Raman spectra of GaSe crystal. Several Raman active phonon modes could be identified in this measurement .....  | <b>35</b> |
| <b>Fig. 3-4</b>  | (a) Time profiles of terahertz pulse transmitted through GaSe crystals of various thicknesses. (d=287, 1110, 2021 μm) (b) Real part of complex refractive index n of GaSe crystal. (c) Imaginary part of complex refractive index k of GaSe crystal .....           | <b>37</b> |
| <b>Fig. 3-5</b>  | Absorption spectrum of pure GaSe crystal from 3 μm to 700 μm .....  | <b>39</b> |
| <b>Fig. 3-6</b>  | Power reflectance measurement over wide range of terahertz frequencies. A strong infrared absorption peak in the range 6–8 THz, called the reststrahlen band, is observed .....   | <b>40</b> |
| <b>Fig. 3-7</b>  | (a) Comparisons of refractive indices n herein and published values. Revised dielectric function-fitted curve is included. (b) Comparison of absorption coefficient α herein with published values. Revised dielectric function-fitted curve is also included ..... | <b>42</b> |
| <b>Fig. 3-8</b>  | Fitting of the infrared generation phase matching curve [18] to obtain the extraordinary refractive indices n <sub>e</sub> . Inset: fitting the THz generation phase matching curve plotted in other works [21, 23, 32] .....                                       | <b>43</b> |
| <b>Fig. 3-9</b>  | Comparisons of extraordinary refractive indices n <sub>e</sub> herein and published values. Inset: the extraordinary refractive indices n <sub>e</sub> in the wide frequency range 0.2–100THz .....   | <b>45</b> |
| <b>Fig. 3-10</b> | Comparison of figures of merit (FOM) of GaSe and LiNbO <sub>3</sub> crystals in terahertz range. Inset: birefringence of GaSe crystal at terahertz frequencies .....  | <b>47</b> |
| <b>Chapter 4</b> |   |           |
| <b>Fig. 4-1</b>  | (a) X-ray rocking curve of pure GaSe (b) X-ray rocking curve of 0.2% Er:GaSe .....  | <b>53</b> |
| <b>Fig. 4-2</b>  | (a) Photography of the GaSe-based ps-DFG system. (b) Schematic of the GaSe-based ps-DFG system .....  | <b>55</b> |
| <b>Fig. 4-3</b>  | Wide tuning range of idler output from 355nm pumped OPA .....   | <b>56</b> |

|                      |  |           |
|----------------------|--|-----------|
| <b>Fig. 4-4</b>      | Absorption coefficients of GaSe are plotted as a function of wavelength in the mid-IR. The solid and dashed curves show our experimental results measured by FTIR and for pure and Er <sup>3+</sup> :GaSe, respectively .....  | <b>57</b> |
| <b>Fig. 4-5</b>      | Measured SHG efficiency of a 3.3 mm long pure GaSe crystal as a function of the internal pulse energy. Inset: Comparison of deff between pure and 0.5% Er:GaSe .....   | <b>59</b> |
| <b>Fig. 4-6</b>      | Type-I DFG output wavelength vs. external PM angle. The filled triangles show the experimental data and solid curve is the fitting curve using the modified Sellmeier equation. Dashed curve: calculated phase matching curve using dispersion of GaSe from Ref. [21]. Dotted curve: calculated phase matching curve using dispersion of GaSe from Ref. [22] .....   | <b>61</b> |
| <b>Fig. 4-7</b>      | Vibrational displacements of atoms in a primitive unit cell for E'-symmetry in the hexagonal GaSe. The arrows indicate only directions of atomic displacements [26] .....  | <b>64</b> |
| <b>Fig. 4-8</b>      | Vibrational displacements of atoms in a primitive unit cell for A <sub>2</sub> '-symmetry in the hexagonal GaSe. The arrows indicate only directions of atomic displacements [26] .....  | <b>65</b> |
| <b>Fig. 4-9</b>      | (a) Calculated parametric gain (dash curve), calculated infrared absorption (dot curve) and measured infrared absorption (solid curve) as a function of wavelength. (b) Measured and calculated pulse energies of the DFG generator versus wavelength. Solid squares show the measured infrared pulse energies for pure GaSe, open triangles show the measured infrared pulse energies for Er <sup>3+</sup> :GaSe, solid curve and dashed curve indicate the calculated pulse energies with and without considering the crystal linear absorption coefficient, respectively. The open circles shown in the THz region are taken from Ref. [8] for comparison ..... | <b>66</b> |
| <br><b>Chapter 5</b> |  |           |
| <b>Fig. 5-1</b>      | Schematic of coherent generation of terahertz radiation by multi-stage optical rectification in GaSe crystals. BS: Beam splitter; ND-Filter: Neutral Density filter; ITO: indium-tin-oxide glass plate; λ/4: quarter wave plate .....  | <b>74</b> |
| <b>Fig. 5-2</b>      | THz time domain waveforms at different GaSe azimuthal φ angle .....  | <b>75</b> |
| <b>Fig. 5-3</b>      | THz wave peak amplitude versus azimuthal φ angle for GaSe emitter .....  | <b>76</b> |



|  |   |            |
|--|---|------------|
| <b>Fig. 5-4</b>  | Time delay dependence of terahertz field amplitude after the second stage. Square-symbols present the terahertz time-domain waveform from the first stage, which are magnified for the easy comparison .....  | <b>77</b>  |
| <b>Fig. 5-5</b>  | Terahertz time-domain waveforms from the first and second stage, and two stages. (a) (d) Terahertz pulse from the second stage leads that from the first stage; (b) (e) best overlapped between the terahertz pulses from two stages; (c) (f) terahertz pulse from the second stage lags behind that from the first stage. Inset: corresponding spectra of the terahertz radiation. Experimental measurement: (a) (b) (c); Theoretical simulation: (d) (e) (f) .. | <b>78</b>  |
| <b>Fig. 5-6</b>  | Terahertz radiation attenuation by the GaSe crystal under high intensity pump laser pulses. Inset (a): fitting of the experimental data for linear and nonlinear absorption coefficient of GaSe crystal pumped by 800 nm optical pulses. Inset (b): fitting of the experimental data for the absorption coefficient $\alpha_{\text{THz,fc}}$ at terahertz frequency in GaSe crystal due to free carriers .....  | <b>83</b>  |
| <b>Fig. 5-7</b>  | Output terahertz field amplitude under different pump intensity .....   | <b>84</b>  |
|  |   |            |
| <b>Chapter 6</b>   |   |            |
| <b>Fig. 6-1</b>  | The experimental configuration of collinear type of OPA .....   | <b>92</b>  |
| <b>Fig. 6-2</b>  | Seeding wavelength versus corresponding external phase matching angle   | <b>94</b>  |
| <b>Fig. 6-3</b>  | The experimental setup of THz-OPA .....   | <b>95</b>  |
| <b>Fig. 6-4</b>  | THz generation by use of the four wave mixing in the plasma (a) THz time domain waveform (b) THz spectrum .....   | <b>96</b>  |
| <b>Fig. 6-5</b>  | The autocorrelation trace of optical pump pulses after stretching by prism pairs .....  | <b>97</b>  |
| <b>Fig. 6-6</b>  | Terahertz signal from the focus (plasma) as a function of BBO crystal rotation angle .....  | <b>98</b>  |
| <b>Fig. 6-7</b>  | Terahertz amplitude versus BBO-to-focus distance .....  | <b>99</b>  |
| <b>Fig. 6-8</b>  | Terahertz amplitude versus laser pulse energy .....   | <b>100</b> |
| <b>Fig. 6-9</b>  | Theoretical gain prediction in this THz-OPA system .....  | <b>102</b> |
| <b>Fig. 6-10</b>   | THz amplification by OPA process (a) THz time domain waveform (b) THz spectrum .....  | <b>103</b> |

## List of Tables Page

### Chapter 1

|                   |  |          |
|-------------------|--|----------|
| <b>Table. 1-1</b> | Nonlinear optical crystals for mid-infrared applications ..... | <b>2</b> |
|-------------------|--|----------|

### Chapter 2

|                   |  |           |
|-------------------|--|-----------|
| <b>Table. 2-1</b> | List of THz emitters and detectors and their advantage ..... | <b>13</b> |
|-------------------|--|-----------|

|                   |  |           |
|-------------------|--|-----------|
| <b>Table. 2-2</b> | Properties of various nonlinear crystals ..... | <b>14</b> |
|-------------------|--|-----------|

### Chapter 3

|                   |   |           |
|-------------------|---|-----------|
| <b>Table. 3-1</b> | Parameters used in the calculation of the optical constants for $\epsilon$ -GaSe from Eq. [6] and Eq. [7] ..... | <b>44</b> |
|-------------------|---|-----------|

|                   |   |           |
|-------------------|---|-----------|
| <b>Table. 3-2</b> | Parameters used in the calculation of the optical constants for $\epsilon$ -GaSe from Eq. [8] and Eq. [9] ..... | <b>46</b> |
|-------------------|---|-----------|

### Chapter 4

|                   |  |           |
|-------------------|--|-----------|
| <b>Table. 4-1</b> | Properties of the long-wavelength lattice vibrations of $\epsilon$ -GaSe ..... | <b>63</b> |
|-------------------|--|-----------|

### Chapter 6

|                   |  |           |
|-------------------|--|-----------|
| <b>Table. 6-1</b> | List of the numerous methods for high power THz generation ..... | <b>90</b> |
|-------------------|--|-----------|



# Chapter 1

## Introduction

### 1.1 Background

Gallium selenide (GaSe) is a native *p*-type semiconductor that belongs to the III-VI layered semiconductor family [1-3]. In the stacking direction (along the crystallographic *z*-axis which is in the direction of the optical *c*-axis), the layers can be arranged in different ways, which leads to the existence of different poly-types. Four modifications ( $\beta$ ,  $\gamma$ ,  $\delta$  and  $\varepsilon$ ) have been reported in the literature [2]. A great deal of studies have made by several research groups to understand the poly-types in these compounds. The formation of a particular poly-type or a mixture of several poly-types depends substantially on the growth method of single crystals. For instance, the *Czochralski* and *Bridgman-Stockbarger* methods yield mainly the  $\varepsilon$  poly-type. Figure 1-1 presents the structure of GaSe, and atomic configuration of GaSe layers. The  $\varepsilon$ -type structure has a  $D_{3h}^1$  space group symmetry with two layers, which is including four molecules (eight atoms) per unit cell. The atoms are located in the planes normal to the *c*-axis in the sequence Se-Ga-Ga-Se. Each GaSe layer thereby consists of two planes of Ga atoms, which are surrounded on two sides by the unit planes of the Se atoms. The strong bonding between two sheets of the same layer is covalent with some ionic contribution. But the bonds between the complete four-fold layer is essentially of the *van der Waals*-type. Due to the characteristics of layer, GaSe exhibits a strongly pronounced structural anisotropy. Consequently, the  $\varepsilon$ -type GaSe is a promising candidate material for nonlinear optical conversion devices in the near- to far-infrared wavelength (1-18  $\mu\text{m}$ ).

GaSe possesses a number of exciting properties, which are listed in Table 1-1, for nonlinear optical application. Among these nonlinear optical crystals, GaSe has a transparency range extending from a wavelength of 0.62  $\mu\text{m}$  to 20  $\mu\text{m}$  where the optical absorption coefficient does not exceed 1  $\text{cm}^{-1}$  throughout the range [1, 3]. The  $\varepsilon$ -type GaSe is a negative uniaxial crystal ( $n_o > n_e$ , where  $n_o$  and  $n_e$  denote the refractive indices in the ordinary and extraordinary direction). Its nonlinear optical coefficients are among the top five for birefringent crystals. Due to its large birefringence, it can satisfy phase matching (PM) conditions for optical configurations under the wide frequency range.

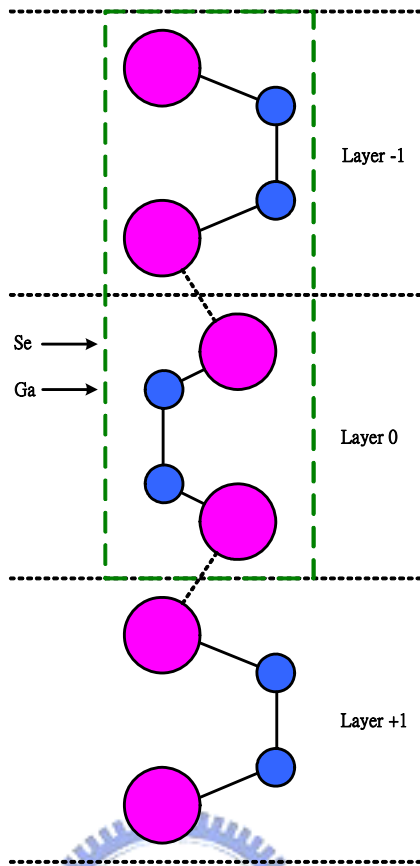


*Fig. 1-1 Layer structure of  $\epsilon$ -GaSe crystal.*

*Table 1-1 Nonlinear optical crystals for mid-infrared applications*

| Crystal                          | Nonlinear Coefficient (pm/V) @ 10.6 $\mu\text{m}$ | Merit Factor ( $\text{d}^2/\text{n}^3$ ) | Transparency Range ( $\mu\text{m}$ ) | Absorption Coefficient ( $\text{cm}^{-1}$ ) @ 10.6 $\mu\text{m}$ | Damage Threshold ( $\text{MW}/\text{cm}^2$ ) @ ~10ns, 1.064 $\mu\text{m}$ |
|----------------------------------|---|--|--------------------------------------|--|---|
| ZnGeP <sub>2</sub>               | 68.9  | 162                                      | 0.74–12                              | 0.83   | 3   |
| AgGaSe <sub>2</sub>              | 32.6  | 63.3                                     | 0.71–19                              | 0.089  | 25  |
| AgGaS <sub>2</sub>               | 12.5  | 12.8                                     | 0.47–13                              | 0.04   | 35  |
| GaSe                             | 54  | 217                                      | 0.62–20                              | 0.081  | 30  |
| Tl <sub>3</sub> AsS <sub>3</sub> | 36.5  | 42.4                                     | 1.28–17                              | 0.082  | 16  |
| CdGeAs <sub>2</sub>              | 217   | 1090                                     | 2.4–18                               | 0.5  | 40  |

For purposes of serving as a nonlinear optical (NLO) material in the mid-infrared and far-infrared (THz), GaSe possesses excellent values for all these properties, as has been extensively studied in the literatures [4-22]. To achieve birefringent phase matching, it is generally necessary to be able to cut and polish the faces of a NLO crystal at an angle arbitrary to the optical axis (for GaSe, this is the *c*-axis, along the [001] direction). However, GaSe has a layered structure, with weak *van der Waals*-like bonds between the layers, making it extremely difficult to cut and polish, except for crystal faces in the plane of cleavage (perpendicular to the optic axis). This feature reduces the usefulness of GaSe as a NLO crystal for practical use, and also complicates access to measurement of its basic properties [4-11].

Nonlinear optical frequency mixing is a well known technique since the discovery of capability of the laser for generation of tunable coherent light using a single crystal. Recently, incoherent parametric super-radiant generation tunable in the range of 3.5–18  $\mu\text{m}$  in GaSe (type-I PM) was obtained by using 110 ps pulses from the actively mode-locked Er:YAG laser as a pump source [12]. Subsequently, picosecond pulses of a mode-locked Er:Cr:YSGG laser were used to pump a traveling-wave OPG; type-I and type-II OPG provided continuous tunability in the range of 3.5–14 and 3.9–10  $\mu\text{m}$ , respectively [13]. On the other hand, there have been a number of reports on difference frequency generation (DFG) to achieve tunable and coherent mid-infrared for GaSe by using variety of laser sources [14, 15]. Additionally, few papers reported on the generation of far-infrared (THz wave) from GaSe crystal [16-18]. Figure 1-2 shows that GaSe has the lowest absorption coefficients in the THz wavelength region [19]. Consequently, GaSe has the largest figure of merit for the THz generation, which is several orders of magnitude large than that for bulk LiNbO<sub>3</sub> at 300  $\mu\text{m}$ . According to *Shi's* results, an efficient and coherent THz wave tunable in the two extremely wide ranges of 2.7–38.4 and 58.2–3540  $\mu\text{m}$ , with typical line-widths of 6000 MHz, had been achieved for the first time [17].

The nonlinear optical crystal is the heart of the nonlinear optical processes. There has been a lot of improvement in growth technology of nonlinear materials, particularly in the infrared region, and a number of nonlinear materials have been developed for laser device application. To perform efficiently, the material should possess a unique combination of optical, thermal and mechanical properties. Recently, the doping of the GaSe crystals was investigated to improve its optical and mechanical properties [20-22]. Recently, the electrical and optical characteristics of erbium doped GaSe (Er:GaSe) crystals had reported [23, 24]. The two acceptor levels were found to originate either from the substitution of one

$\text{Er}^{3+}$  for one pair of  $\text{Ga}^{2+}$  or insertion of one  $\text{Er}^{3+}$  interstitial ions at interlayer sites in the unit cell. The structure of GaSe can also be slightly altered by the erbium doping. Recently, the optical properties of Er:GaSe crystals and its potential in the generation of mid-infrared radiation had been further explored [25].

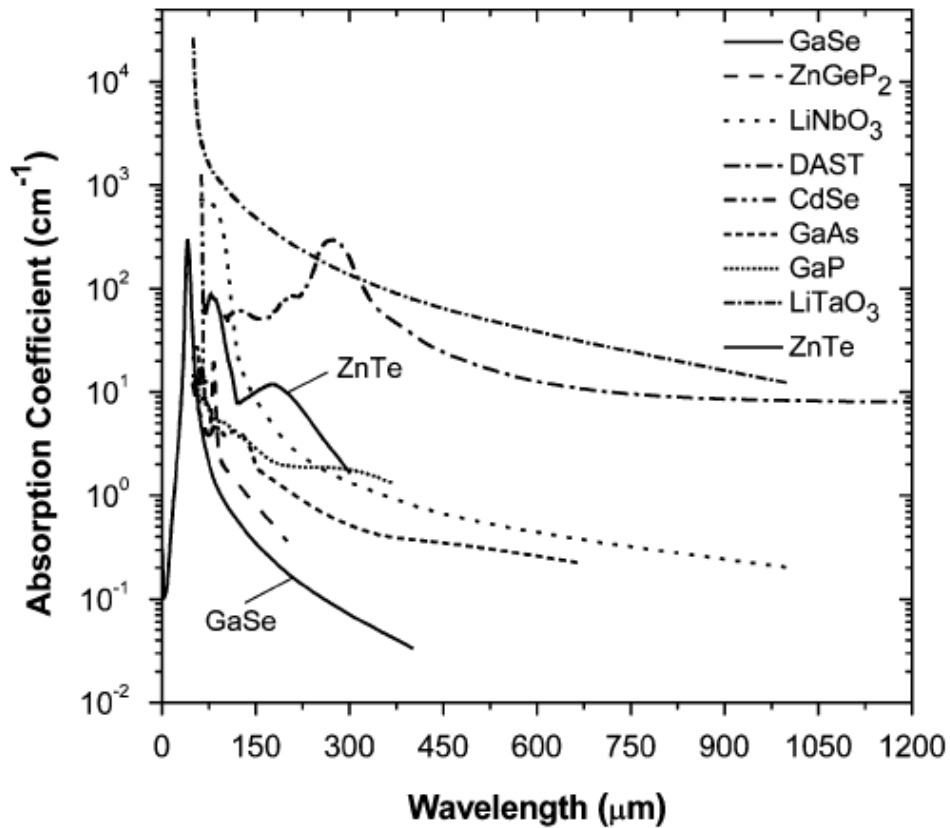


**Fig. 1-2** Absorption coefficients versus wavelength for several nonlinear crystals, some of which were frequently used for terahertz generation. The absorption spectrum for CdSe available covers a narrow wavelength range of 63–71  $\mu\text{m}$  [19].

In this work, the GaSe crystals were grown by a vertical *Bridgman* furnace. All the GaSe crystals used herein are home-made and provided by Prof. *Chen-Shiung Chang*'s group from National Chiao Tung University (NCTU). The photograph of the as-grown GaSe crystal is shown in Fig. 1-3. The optical *c*-axis is perpendicular to the good optical cleaved surface, as shown in Fig. 1-3. Tuning the external angles is necessary for perform the



phase-matching conditions (the angle between the optical axis and beam propagation direction) in the nonlinear optical experiments.



*Fig. 1-3 A cleaved surface of the as-grown  $\epsilon$ -GaSe crystal.*

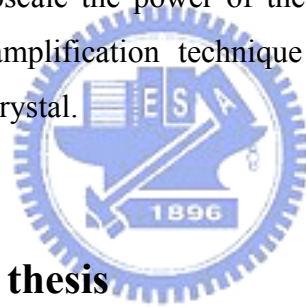


## 1.2 Motivation

GaSe crystal has been widely utilized to the generation and application of infrared and THz frequency regime. For accessing to the practical application of optoelectronics device, the realization of the basic optical properties of this crystal is very important and indispensable. Fortunately, the published literatures mentioned about the optical constants of GaSe crystal are inconsistent. The knowledge of the Reststrahlen band and vibration modes in this crystal is still limited. Therefore, we motivated to explore the optical properties of GaSe crystal by means of the optical measurements, including Raman scattering, Fourier Transform Infrared Spectroscopy (FTIR) and terahertz time domain spectroscopy (THz-TDS) in this study. After understanding fundamental optical properties, such as ordinary and extraordinary dielectric functions, Sellmeier equations and vibration frequencies, the extensive applications of GaSe crystal to perform the light source generation and nonlinear optical frequency conversion processes could be expected. Then it is proved that GaSe crystals have the promising properties such as high nonlinear coefficient and low absorption coefficient that benefits the high conversion efficiency in such frequency conversion processes.

There have been numerous works described that GaSe crystal can generate light source with wide frequency range from mid-infrared to THz by use of the frequency conversion technique such as difference frequency mixing process. However, few papers concern the optical behaviors in the strong absorption region and the role of the absorption effect in the DFG process. In this work, we further explore the origin and effect of the infrared absorption edges based upon the understanding of the proposed Sellmeier equations. Moreover, we investigate the effect of infrared absorption on the generation properties of coherent infrared radiation from mid-infrared to THz region in the GaSe crystal.

The conversion efficiency for generating the THz radiation is usually quite low among the several promising techniques. In order to yields the intense single cycle and high amplitude THz wave, we propose some methods to increase the output power of THz radiation. First, we propose the multiple stages of optical rectification technique which is useful for generating high amplitude single-cycle terahertz pulses, not limited by the pulse walk-off effect from group velocity mismatch in the nonlinear optical crystal used. On the other hand, we attempt to upscale the power of the weak THz radiation by utilizing the phase-matching parametric amplification technique associated with the high nonlinear coefficient property of GaSe crystal.



### 1.3 Organization of thesis

This section is to outline the scope of a PhD research program by the author of this thesis, and describe the structure of the thesis which contains most of the achievements of this study. This thesis consists of seven chapters including this introduction, background information and motivation (Chapter 1), and the overview of the radiation light sources of mid-infrared to far-infrared (terahertz) (Chapter 2), and optical properties and potential applications of  $\epsilon$ -GaSe crystal in terahertz frequencies (Chapter 3), and the generation properties of coherent infrared radiation in the optical absorption region through difference frequency mixing (DFM) (Chapter 4), and coherent generation and spectral synthesis of terahertz radiation with multiple stages of optical rectification (Chapter 5), and the study of THz optical parametric amplification in  $\epsilon$ -GaSe crystal (Chapter 6), as well as conclusion and future work (Chapter 7).

Chapter 2 presents an overview of the radiation light sources of mid-infrared to far-infrared (terahertz). Several promising generation techniques, including optical parametric generation (OPG), different frequency generation (DFG), four-wave mixing

(FWM), photoconductive switch and optical rectification (OR) will be introduced in this chapter. In addition, few detection methods for THz waves are also included.

Chapter 3 introduces that optical constants for a single crystal  $\epsilon$ -GaSe are investigated by use of the terahertz time-domain spectroscopy (THz-TDS) and Fourier Transform Infrared Spectroscopy (FTIR) over the frequency range from 0.2 to 3 THz. Based upon the experimental data, the modified ordinary and extraordinary complex dielectric functions of  $\epsilon$ -GaSe is proposed.

Chapter 4 describes the application of  $\epsilon$ -GaSe crystal in coherent generation of the picosecond wide tuning range infrared radiation. The generation properties in the absorption region are discussed herein. The origin and effect of the infrared absorption edges are also examined in this chapter. The output power variation as a function of the wavelength can be explained by the spectral profile of the parametric gain and absorption coefficient.

Chapter 5 demonstrates that multiple stages optical rectification will be useful for generation of high-field, single-cycle terahertz pulse not limited by the availability of thick GaSe crystals of good optical quality or the walk-off effect due to group velocity mismatch.

Chapter 6 demonstrates the application of  $\epsilon$ -GaSe crystal in scaling up the pulse energy of the broad band THz radiation by using the parametric amplification technique. The theoretical prediction and practical performance and the table-top system are also reported.

Consequently, the conclusion to this work is given in Chapter 7. Recommendations of further work are also given in this chapter.

## References

- [1] V. G. Dmitriev, G. G. Gurzadyan, and D. N. Nikogosyan, *Handbook of Nonlinear Optical Crystals* (Springer, Berlin, 1997), pp. 166-169.
- [2] T. J. Wieting and M. Schluter (Eds.), *Electrons and Phonons in Layered Crystal Structures* (D. Reidel Publishing Company, Holland, 1979).
- [3] E. D. Palik, *Handbook of Optical Constants of Solids* (Academic, New York, 1998), Vol. III.
- [4] J. D. Wasscher and J. Dieleman, "Anisotropy of the optical constants of GaSe near the band edge," *Phys. Lett.* **39A**, 279-280 (1972).
- [5] N. Piccioli, R. L. Toullec, M. Mejatty, and M. Balkanski, "Refractive index of GaSe between 0.45  $\mu\text{m}$  and 330  $\mu\text{m}$ ," *Appl. Opt.* **16**, 1236-1238 (1977).
- [6] V. M. Burlakov, E. A. Vinogradov, G. N. Zhizhin, N. N. Mel'nik, D. A. Rzaev, and V. A. Yakovlev, "Optical properties of GaSe films at lattice vibration frequencies," *Sov. Phys. Solid State* **21**, 1477-1480 (1979).
- [7] S. Adachi and Y. Shindo, "Optical constants of  $\epsilon$ -GaSe," *J. Appl. Phys.* **71**, 428-431 (1992).
- [8] K. Allakhverdiev, N. Fernelius, F. Gashimzade, J. Goldstein, E. Salaev, and Z. Salaeva, "Anisotropy of optical absorption in GaSe studied by midinfrared spectroscopy," *J. Appl. Phys.* **93**, 3336-3339 (2003).
- [9] K. R. Allakhverdiev, T. Baykara, A. K. Gulubayov, A. A. Kaya, J. Goldstein, N. Fernelius, S. Hanna, and Z. Salaeva, "Corrected infrared Sellmeier coefficients for gallium selenide," *J. Appl. Phys.* **98**, 093515-1-6 (2005).
- [10] K. Allakhverdiev, T. Baykara, S. Ellialtioglu, F. Hashimzade, D. Huseinova, K. Kawamura, A. A. Kaya, A. M. Kulibekov (Gulubayov), and S. Onari, "Lattice vibrations of pure and doped GaSe," *Mater Res. Bull.* **41**, 751-763 (2006).
- [11] C. -W. Chen, Y. -K. Hsu, J. Y. Huang, C. -S. Chang, J. Y. Zhang, and C. -L. Pan, "Generation properties of coherent infrared radiation in the optical absorption region of GaSe crystal," *Opt. Express* **14**, 10636-10644 (2006).
- [12] K. L. Vodopyanov and V. G. Voevodin, "2.8  $\mu\text{m}$  laser pumped type I and type II traveling-wave optical parametric generator in GaSe," *Opt. Commun.* **114**, 333-335 (1995).
- [13] K. L. Vodopyanov and V. Chazapis, "Extra-wide tuning range optical parametric generator," *Opt. Commun.* **135**, 98-102 (1997).

- [14] R. A. Kaindl, M. Wurm, K. Reimann, P. Hamm, A. M. Weiner, and M. Woerner, "Generation, shaping, and characterization of intense femtosecond pulses tunable from 3 to 20  $\mu\text{m}$ ," *J. Opt. Soc. Am. B* **17**, 2086-2094 (2000).
- [15] R. S. Putnam and D. G. Lancaste, "Continuous-wave laser spectrometer automatically aligned and continuously tuned from 11.8 to 16.1  $\mu\text{m}$  by use of diode-laser-pumped difference-frequency generation in GaSe," *Appl. Opt.* **38**, 1513-1522 (1999).
- [16] W. Shi, Y. J. Ding, N. Fernelius, and K. Vodopyanov, "Efficient, tunable, and coherent 0.18–5.27 THz source based on GaSe crystal," *Opt. Lett.* **27**, 1454-1456 (2002).
- [17] W. Shi and Y. J. Ding, "A monochromatic and high-power terahertz source tunable in the ranges of 2.7-38.4 and 58.2-3540  $\mu\text{m}$  for variety of potential applications," *Appl. Phys. Lett.* **84**, 1635-1637 (2004).
- [18] T. Tanabe, K. Suto, J. -i. Nishizawa, and T. Sasaki, "Characteristics of terahertz-wave generation from GaSe crystals," *J. Phys. D: Appl. Phys.* **37**, 155-158 (2004).
- [19] Y. J. Ding, "High-power tunable terahertz sources based on parametric processes and applications," *IEEE J. Sel. Topics Quantum Electron.* **13**, 705-720 (2007).
- [20] D. R. Suhre, N. B. Singh, V. Balakrishna, N. C. Fernelius, and F. K. Hopkins, "Improved crystal quality and harmonic generation in GaSe doped with indium," *Opt. Lett.* **22**, 775-777 (1997).
- [21] N. B. Singh, D. R. Suhre, W. Rosch, R. Meyer, M. Marable, N. C. Fernelius, F. K. Hopkins, D. E. Zelmon, and R. Narayanan, "Modified GaSe crystals for mid-IR applications," *J. Cryst. Growth* **198**, 588-592 (1999).
- [22] S. Das, C. Ghosh, O. G. Voevodina, Yu. M. Andreev, and S. Yu. Sarkisov, "Modified GaSe crystal as a parametric frequency converter," *Appl. Phys. B* **82**, 43-46 (2006).
- [23] Y. K. Hsu, C. S. Chang, and W. F. Hsieh, "Photoluminescence study of GaSe doped with Er," *Jpn. J. Appl. Phys.* **42**, 4222-4225 (2003).
- [24] Y. K. Hsu, W. C. Huang, and C. S. Chang, "Electrical properties of GaSe doped with Er," *J. Appl. Phys.* **96**, 1563-1567 (2004).
- [25] Y. -K. Hsu, C. -W. Chen, J. Y. Huang, C. -L. Pan, J. -Y. Zhang, and C. -S. Chang, "Erbium doped GaSe crystal for mid-IR applications," *Opt. Express* **14**, 5484-5491 (2006).

## Chapter 2

# Overview of the radiation light sources of mid-infrared to far-infrared (terahertz)

### 2.1 Introduction

Sources of tunable high-quality, ultrashort laser pulses in the near- and mid-infrared spectral region are an important tool in various fields of optical spectroscopy. As far as comparatively compact sources are concerned, the infrared radiation can be covered best by means of nonlinear frequency conversion. Extensive experimental studies have been carried out in this field of research in both the nanosecond and picosecond / femtosecond regime. Coherent sources in the mid-infrared to far-infrared are of prime importance for molecular spectroscopy, eye-safe medical instrumentations, radar and remote sensing of atmospheric constituents, and for numerous military applications such as target tracking, obstacle avoidance, and infrared countermeasures.

As virtually all fundamental vibrational modes of molecules and molecular ions lie in the 2-20  $\mu\text{m}$  wavelength region, infrared spectroscopy provides a convenient and real-time method of detection for most gases. Spectroscopic techniques have been successfully applied to monitor air pollution and to identify and quantify the presence of specific gaseous constituents in the atmosphere. In the mid-infrared spectral region the fundamental vibrational–rotational absorption spectra of molecular pollutants are very rich in absorption lines and the absorption frequencies are generally located so that strong lines of a number of most pollutant gases can be well distinguished from those of the others. Absorption spectra can thus be utilized for the detection and identification of polluting molecular species in this so-called fingerprint region.

After the rapid progress in ultrashort lasers and the successes in semiconductor technology and nonlinear optics, it has led the birth of a new area of applied physics known as optoelectronics or photonics in 1970s. One of the most promising photonic spectroscopic applications is the terahertz time-domain spectroscopy (THz-TDS). Terahertz region lies between microwave and infrared regions is relatively narrow, it is still important in condensed matter physics. There are many interesting phenomena falling right to this region, especially the soft lattice vibrations in dielectrics.



THz pulses generated by sub-picosecond laser pulses based on photoconduction and optical rectification with a broad bandwidth have found many applications, such as THz imaging, THz spectroscopy for studies of carrier dynamics and intermolecular dynamics in liquids, and dielectric responses of molecules, polymers, and semiconductors. A tunable and coherent THz source is one of the key elements for applications such as chemical identification, biomedical diagnostics, and THz spectroscopy. For instance, THz-probing technology exhibits a unique potential for label-free detection of a DNA binding state. Furthermore, it was recently demonstrated that cw THz waves can be used to detect cancer. To achieve these important applications and therefore to create a new era for THz science and technology, a compact, efficient, and coherent THz source is essential. Although in the past short THz pulses were generated by means of optical rectification, by photoconduction, and by *Cerenkov* radiation, it was difficult to measure low conversion efficiencies directly. Quite low conversion efficiency of  $\sim 10^{-10}$  was achieved based on optical rectification.

Terahertz radiation is in the frequency range from about 0.1 to 10 THz, which corresponds to wave-numbers between 3 and  $300\text{ cm}^{-1}$ , photon energies between 0.4 and 40 meV, temperatures between 5 and 500K and wavelengths between 3 mm and  $30\text{ }\mu\text{m}$ . This frequency range, shown in the Fig. 2-1, has several names: far infrared, sub-millimeter wave and terahertz range. Until some years ago, this frequency range was known as the ‘THz gap’. The lack of efficient sources and of sensitive detectors made measurements very difficult. Accordingly, the THz range remained to a large extent unexplored.

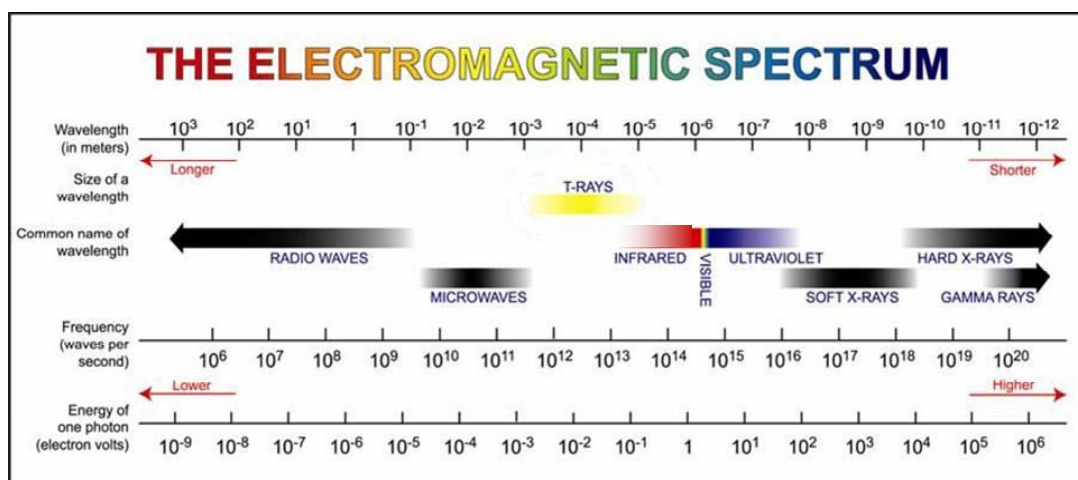


**Fig. 2-1 Overview of frequency regions.**

The appearance of ultrashort pulsed laser of  $\sim 100$  ps pulse duration made it possible to generate THz waves covering the whole THz spectral range. In 1981, *Mourou* and *Auston* first demonstrated generation and detection of pulsed THz radiation by a photoconductive switch with advantages of time resolution of picosecond and high sensitivity enhanced by phase-lock technique [1, 2]. In 1988, *Grischkowsky* used the photoconductor dipole antenna as the THz sensor, pushing the spectrum into the order of terahertz frequency [3]. Numerous investigations on THz wave showed a modest increase, whereas after 1995 the field has experienced an impressive growth. Probably the most important single development responsible for this growth is the invention of the mode-locked Ti: sapphire laser, which has greatly facilitated the use of ultrashort pulses in all sorts of experiments, among them the generation and measurement of THz pulses. Afterward a variety of antennas was appeared, like typical dipole antenna, large aperture photoconductor dipole antenna [4] and also another method using semiconductor surface electric field [5] to generate THz pulses by the ultrashort pulsed laser. In 1996, *Wu et al.* developed free-space electro-optic sampling (FS-EOS) technique to enhance signal to noise ratio (S/N ratio) up to 105 and to achieve much large dynamic range [6].

Since THz spectroscopy is a time-domain method, the pump-probe experiments can be easily performed. The sample can be excited by the optical pump beam, which is split from the femtosecond laser beam the pump beam is perfectly synchronized with the THz probe pulse and gating pulse. During last few years, the femtosecond optical amplifiers and parametric generators became commercially available. The regenerative amplified laser enabled us to generate a very intense excitation pulse and the latter to tune the excitation wavelength. This makes the THz time domain spectroscopy very suitable for investigations of ultrafast dynamics on the sub-picosecond time scale for the fundamental physics. The THz wave has an infinite potential in application of science. In the bioscience, the photon energy of THz is much smaller than the traditional X-ray and the pathological changes will not be induced by THz wave in human body. Since different tissues of body have different sensitivity for THz waves, more detailed information can be obtained through the THz tomography imaging. Photon energy of THz wave is about 4 meV for 1 THz, which approximately equals to the binding energy of the excitons in many semiconductors. Most of all, recently developed THz waves possess ultrashort duration with broad bandwidth and provide both high sensitivity and time-resolved phase information. These advantages can be used in several applications, such as the study of carrier dynamics of condensed matters with high temporal and spectral resolutions. Recently, the spectroscopic technique using

pulsed THz wave, called terahertz time-domain spectroscopy (THz-TDS), has been developed, by taking advantage of short pulses of broadband THz radiation. THz-TDS has the time resolution of sub-picosecond level and the spectral resolution of 50 GHz. The ability of THz-TDS to measure both real and imaginary parts of the dielectric function in real time has made it a promising method to investigate the materials at THz frequencies.

The development and spread of THz sources and receiver advance the THz time-domain spectroscopy. Table 2-1 shows a list of common use of THz emitters and detectors. Furthermore, we will only consider table-top sources herein, i.e. sources one can have in one's own lab. Such sources are nearly always based on femtosecond lasers in the visible or near-infrared.

*Table 2-1 List of THz emitters and detectors and their advantage*

| <b>Emitter</b>                  | <b>Type</b> | <b>Advantage</b>                       |
|---------------------------------|-------------|--|
| Free electron laser             |             | highest THz power                      |
| Gunn oscillator                 |             | generate sub THz                       |
| Quantum cascade laser           |             | cw, single mode                        |
| Difference frequency generation |             | narrow line-width cw possible          |
| Photoconductive antenna         |             | high SNR                               |
| Semiconductor surfaces          |             | higher THz power                       |
| Optical rectification           |             | broadband THz spectrum                 |
| <b>Detector</b>                 | <b>Type</b> | <b>Advantage</b>                       |
| Bolometer                       |             | incoherent radiation, more sensitivity |
| Pyroelectric detector           |             | incoherent radiation                   |
| Photoconductive dipole antenna  |             | higher SNR                             |
| Electro-optic crystal           |             | broadband THz spectrum                 |

## 2.2 Overview of coherent mid-infrared generation

Ultrashort pulses in the mid-infrared (MIR) spectral range ( $\lambda = 3\text{--}20 \mu\text{m}$ ) provide powerful tools to investigate the ultrafast dynamics of non-equilibrium excitations in condensed matter [7]. Recently, structural changes in molecules or molecular complexes

were monitored directly in the time domain by means of the transient absorption of prominent molecular vibrations [8]. Vibrational dynamics and correlations in liquid water or in proteins have been successfully studied with femtosecond pulses in the MIR [9-12]. Femtosecond infrared spectroscopy has also been increasingly applied to problems in solid-state physics [13]. For instance, time-resolved investigations of the coherent [14] or incoherent [15] dynamics of intersubband excitations in semiconductor nanostructures have provided new insights that cannot be obtained by experiments based on interband transitions. Recently, the ultrafast dynamics of the electronic system in a high transition-temperature superconductor was investigated near the conductivity gap with femtosecond MIR pulses as a probe [16]. Such experiments increasingly call for sources that provide intense pulses on the micro-joule level with pulse durations of the order of 100 fs or less. In this temporal range tabletop laser systems based on parametric devices are superior to free-electron lasers, which typically provide much longer pulses and for which the realization of synchronized pulses at two different wavelengths is a difficult problem that involves additional high-power laser systems.

**Table 2-2 Properties of various nonlinear crystals**

| Crystal             | Point Group | Transmission Range ( $\mu\text{m}$ ) | Nonlinear coefficient (pm/V) | Effective Nonlinearity $d_{eff}$                        | $n_o$<br>$n_e$ |
|---------------------|-------------|--------------------------------------|------------------------------|---|----------------|
| KDP                 | $\bar{4}2m$ | 0.17 – 1.5                           | 0.39 ( $d_{36}$ )            | $d_{ooe}=d_{36}\sin\theta\sin2\varphi$                  | 1.50           |
|                     |             |                                      |                              | $d_{eoe}=d_{36}\sin2\theta\cos2\varphi$                 | 1.46           |
| BBO                 | 3m          | 0.19 – 3                             | 2.3 ( $d_{22}$ )             | $d_{ooe}=d_{31}\sin\theta-d_{22}\cos\theta\sin3\varphi$ | 1.66           |
|                     |             |                                      | 0.16 ( $d_{31}$ )            | $d_{eoe}=d_{22}\cos^2\theta\cos3\varphi$                | 1.54           |
| LiIO <sub>3</sub>   | 6           | 0.28 – 6                             | 4.4 ( $d_{31}$ )             | $d_{ooe}=d_{31}\sin\theta$                              | 1.86           |
|                     |             |                                      |                              |   | 1.72           |
| AgGaS <sub>2</sub>  | $\bar{4}2m$ | 0.47 – 13                            | 12 ( $d_{36}$ )              | $d_{ooe}=d_{36}\sin\theta\sin2\varphi$                  | 2.35           |
|                     |             |                                      |                              | $d_{eoe}=d_{36}\sin2\theta\cos2\varphi$                 | 2.30           |
| AgGaSe <sub>2</sub> | $\bar{4}2m$ | 0.71 – 19                            | 33 ( $d_{36}$ )              | $d_{ooe}=d_{36}\sin\theta\sin2\varphi$                  | 2.59           |
|                     |             |                                      |                              | $d_{eoe}=d_{36}\sin2\theta\cos2\varphi$                 | 2.56           |
| CdSe                | 6mm         | 0.75 – 25                            | 18 ( $d_{31}$ )              | $d_{oeo}=d_{31}\sin\theta$                              | 2.43           |
|                     |             |                                      |                              |   | 2.45           |
| GaSe                | $\bar{6}2m$ | 0.62 – 20                            | 54 ( $d_{22}$ )              | $d_{ooe}=d_{22}\cos\theta\sin3\varphi$                  | 2.70           |
|                     |             |                                      |                              | $d_{eoe}=d_{22}\cos^2\theta\cos3\varphi$                | 2.38           |
| Te                  | 32          | 3.5 – 36                             | 670 ( $d_{11}$ )             | $d_{eeo}=d_{11}\cos^2\theta\sin3\varphi$                | 4.79           |
|                     |             |                                      |                              | $d_{oeo}=d_{11}\cos\theta\cos3\varphi$                  | 6.25           |

✧ Nonlinear coefficients and refractive indices are listed for  $\lambda=1 \mu\text{m}$  for KDP · BBO and LiIO<sub>3</sub>; and  $\lambda=10 \mu\text{m}$  for AgGaS<sub>2</sub> · AgGaSe<sub>2</sub> · CdSe · GaSe and Te. The indices of effective nonlinearity  $d_{abc}$  denote the polarizations (o, ordinary; e, extraordinary) of phase-matched process  $a + b \rightarrow c$ .

$\lambda = 2\text{--}5 \mu\text{m}$  : Sources for this limited range are comparatively abundant. Such setups permit, for example, the generation of as much as 100 mW of 60–150 fs pulses from high repetition rate (80 MHz) parametric oscillators based on KNbO<sub>3</sub> or KTiOAsO<sub>4</sub> (KTA) crystals [17, 18]. At kilohertz repetition rates, parametric amplification in KTP provides equally short pulses down to ~70 fs duration with 200 nJ pulse energy in the 3–4  $\mu\text{m}$  range [19]. Difference frequency mixing of signal and idler pulses in thin KTP or LiIO<sub>3</sub> crystals generates 200 fs pulses tunable from 2.5 to 5  $\mu\text{m}$  [20–23].

$\lambda = 3\text{--}10 \mu\text{m}$  : This broader range necessitates use of nonlinear crystals with sufficient transparency. The limited number of possible materials includes AgGaS<sub>2</sub> (see the Table 2-2) or ZnGeP<sub>2</sub>. Difference mixing of the output of an 82 MHz, two-color Ti: sapphire laser in AgGaS<sub>2</sub> permitted the generation of 500 fs pulses tunable from 7.5 to 12.5  $\mu\text{m}$  [24]. At low repetition rates, a ZnGeP<sub>2</sub>-based parametric amplifier produces 200 fs pulses ( $\lambda = 6 \mu\text{m}$ ) tunable from 2.5 to 10  $\mu\text{m}$  [25]. From amplified Ti: sapphire laser systems that deliver intense pulses at a 1 kHz repetition rate, 130 fs pulses tunable from 3 to 10  $\mu\text{m}$  were generated by difference frequency mixing (DFM) pulses from an optical parametric amplifier (OPA) in AgGaS<sub>2</sub> [26, 27].

$\lambda = 10\text{--}20 \mu\text{m}$  : Generation of femtosecond pulses at wavelengths beyond 10  $\mu\text{m}$  has barely been studied. Complex setups constructed from 80 MHz parametric oscillators and subsequent DFM in AgGaSe<sub>2</sub> or GaSe deliver output powers of  $\leq 2 \text{ mW}$  in the 5–18  $\mu\text{m}$  range [28, 29]. However, from such schemes that combine several nonlinear frequency-conversion stages and require high-power Ti: sapphire lasers (1–2 W) and synchronously pumped, stabilized external cavities, only pulse durations above 300 fs were demonstrated. Recently, some of the present authors and others demonstrated a compact scheme for the generation of pulses of typically ~150 fs duration in the spectral range from 7 to 20  $\mu\text{m}$  at high repetition rates by parametric mixing within the broad spectra of 13 fs pulses from a 2 MHz cavity-dumped Ti: sapphire oscillator in GaSe [30]. Setups based on amplified systems allow for much higher pulse energies but typically produce even longer pulses. *Bayanov et al.* use the second harmonic of a 4 Hz, 7 mJ picosecond Nd: glass

amplifier to pump a three-path OPA [31]. By subsequent DFM in GaSe, pulses tunable from 4 to 20  $\mu\text{m}$  and with energies of as much as 11  $\mu\text{J}$  with pulse duration 700 fs are generated. Other setups generate pulses of 1 ps [32] or 10 ps [33] duration. Recently, it was shown that non-phase-matched optical rectification of very short,  $\sim 10$  fs Ti: sapphire pulses or optically switched high field transport in semiconductors can also provide higher-frequency components up to the MIR ( $\lambda > 8 \mu\text{m}$ ) range [34-37]. However, applications to nonlinear (e.g., pump-probe) spectroscopy with such an ultrabroadband (0–30 THz) source are rare because of the large spectral spread of group delay and diffractive properties and the very low (nanowatt) average powers.

Nonlinear materials like AgGaSe<sub>2</sub>, GaSe and CdSe have been proven to be well suited in the considered wavelength range. Starting with intense but fixed-frequency radiation at 1  $\mu\text{m}$  different conversion schemes depending on the pump system have been investigated. As GaSe allows for pumping at 1  $\mu\text{m}$  efficient generation of MIR radiation is possible by parametric amplification of tunable near-IR (NIR) radiation delivered by dye lasers or parametric sources with tuning ranges up to 20  $\mu\text{m}$  [31, 32, 38]. *Kaindl et al.* performed an intense mid-infrared light source that provides femtosecond pulses on a micro-joule energy level, broadly tunable in the 3–20  $\mu\text{m}$  wavelength range [39]. The pulses are generated by phase-matched difference-frequency mixing in GaSe of near-infrared signal and idler pulses of a parametric device based on a 1 kHz Ti: sapphire amplifier system. Recently, *Shi et al.* demonstrated the phase-matched MIR generation in GaSe up to 28.7  $\mu\text{m}$  by difference frequency mixing of a Nd:YAG laser (1.064  $\mu\text{m}$ ) and a tunable near NIR parametric source with nanosecond pulse duration [40]. A drawback of such a conversion scheme is the two-photon absorption (TPA) in GaSe still observable for high intensity radiation around 1  $\mu\text{m}$ . Accordingly, pumping at longer wavelengths seems to be a reasonable choice.

Therefore, several nonlinear optical crystals could be applied to generate the mid-infrared radiation through the difference frequency mixing technique. Figure 2-2 represents the yielded frequency ranges for several common used NLO crystals in the experiments for mid-infrared generation. It is obviously shown that GaSe crystal possesses the promising property which can cover widest generated mid-infrared frequency range compared with other crystals.



| Crystal                   | 1 | 5 | 10 | 15 | 20 | 38 ( $\mu\text{m}$ ) |
|---------------------------|---|---|----|----|----|----------------------|
| <b>KNbO<sub>3</sub></b>   |   |   |    |    |    |                      |
| <b>KTA</b>                |   |   |    |    |    |                      |
| <b>KTP</b>                |   |   |    |    |    |                      |
| <b>LiIO<sub>3</sub></b>   |   |   |    |    |    |                      |
| <b>AgGaS<sub>2</sub></b>  |   |   |    |    |    |                      |
| <b>ZnGaP<sub>2</sub></b>  |   |   |    |    |    |                      |
| <b>AgGaSe<sub>2</sub></b> |   |   |    |    |    |                      |
| <b>CdSe</b>               |   |   |    |    |    |                      |
| <b>GaSe</b>               |   |   |    |    |    |                      |

*Fig. 2-2 Generated frequency ranges for several NLO crystals in mid-infrared generation.*

## 2.3 Overview of coherent terahertz generation and detection

### 2.3.1 Generation by photoconductive antenna

Femtosecond laser excites a biased semiconductor with photon energies greater than its band-gap, will produce electrons and holes at the illumination point in the conduction and valence bands. Figure 2-3 presents the schematic of PC antenna. Owing to fast changing of the density of the carriers and accelerated by the applied dc bias, electromagnetic field radiates into free-space. The production of currents with a full-width half-maximum (FWHM) less than 1 ps depends on the carrier lifetime in the semiconductor [41].

The carrier density behavior in time is given by

$$dn/dt = -n/\tau_t + G(t) \quad (1)$$

where  $n$  is the carrier density and  $G(t) = n_0 \exp(t/\Delta t)^2$  is the generation rate of carriers due to laser pulse excitation, with  $\Delta t$  the laser pulse width and  $n_0$  is the generated carrier density at  $t = 0$ . The generated carriers are accelerated by the bias field with a velocity rate given by

$$dv_{e,h}/dt = -v_{e,h}/\tau_{rel} + (q_{e,h}E)/m_{eff,e,h} \quad (2)$$

where  $v_{e,h}$  is the mean velocity of the carrier,  $q_{e,h}$  are the charge of the electron and hole,  $\tau_{rel}$  is the momentum relaxation time, and  $E$  is the local electric field, which is less than the applied bias  $E_b$  because of the screen effect of space charges. The relation is as follows:



$$E = E_b - P/3\epsilon_r \quad (3)$$

where  $\epsilon_r$  is the dielectric constant and  $P$  is the polarization induced by the separation of electrons and holes. The polarization depends on time according to the expression

$$dP/dt = -P/\tau_{rec} + J \quad (4)$$

where  $\tau_{rec}$  is the recombination time between electrons and holes ( $\tau_{rec} = 10$  ps for LT-GaAs) and  $J = env_h + (-e)nv_e$  is the current density.

The far-field radiation can be expressed as follows:

$$E_{THz} \propto \partial J / \partial t \propto ev\partial n / \partial t + en\partial v / \partial t \quad (5)$$

where  $v$  equals to  $v_e - v_h$ . The transient electromagnetic field  $E_{THz}$  consists of two terms: the first term describes the carrier density change effect while the second term describes the effect of charge acceleration due to the electric field bias.

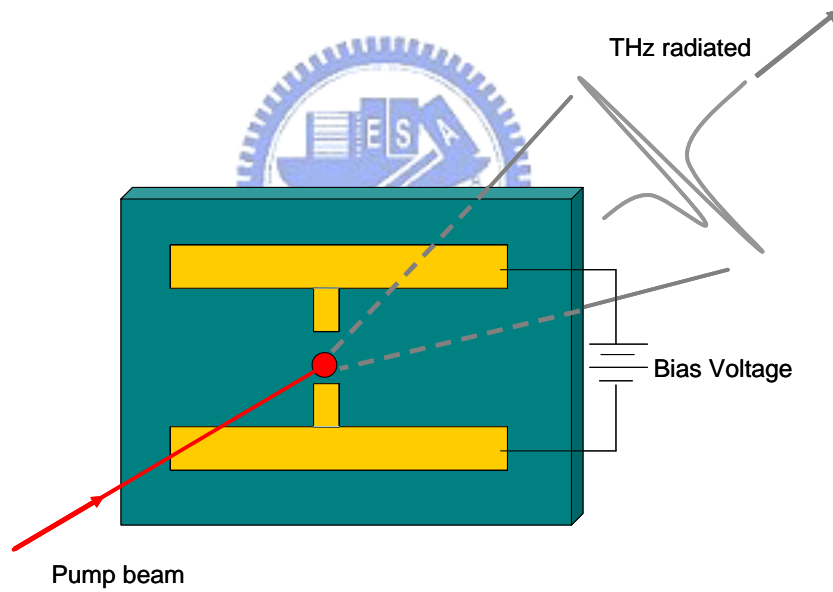


**Fig. 2-3 Schematic of PC antenna.**

### 2.3.2 Generation by optical rectification

The generation of terahertz by optical rectification is only possible by pulsed laser. Optical rectification is the generation of DC polarization by the application of optical waves in a non-centrosymmetric medium with large second-order susceptibility  $\chi^{(2)}$ . Assume a femtosecond pumping pulse propagates in z-direction, with the pulse duration  $\tau_G$  in Gaussian profile:

$$I(\omega) = I_0(\omega) \exp(-\tau_G \omega^2 / 2) \quad (6)$$

When this pulse propagates through the nonlinear optical crystal, there will be induced polarization in the crystal:

$$P^{(2)}(z, \omega) = \chi^{(2)}(\omega) I(\omega) \exp(-\omega z / v_g) \quad (7)$$

where  $v_g$  is the group velocity of pump pulse. By solving nonlinear Maxwell's equations:

$$-\nabla^2 E + \frac{1}{c^2} \frac{\partial^2 D^{(1)}}{\partial t^2} = -\frac{4\pi}{c^2} \frac{\partial^2 P^{(2)}}{\partial t^2} \quad (8)$$

The locally generated terahertz electric field can be expressed as:

$$E_{THz}(z, \omega) = \omega^2 \chi^{(2)}(\omega) z \text{sinc}(\Delta k_{THz} z / 2) \quad (9)$$

Then the generated terahertz is the integral of local generation.

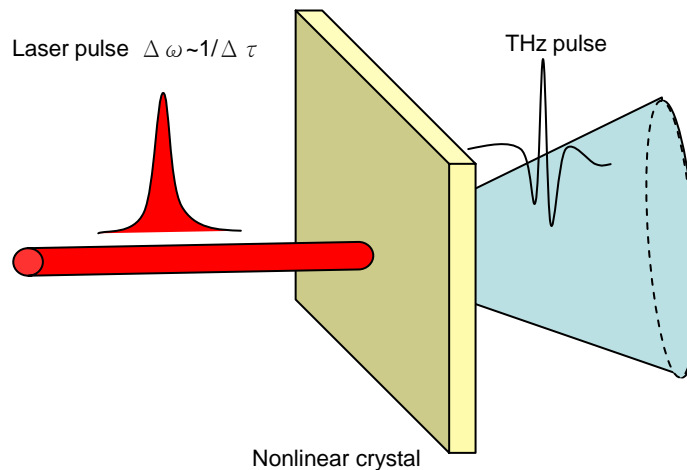


**Fig. 2-4 Illustration of terahertz radiation by optical rectification.**

If there are no momentum mismatch, the output signal follows the intensity envelope of the pump laser pulse. For instance, laser pulses with duration of 100 fs are used as the pump source, the spectrum of generated pulses center approximately at a few terahertz. Because the ultrashort pulses have large bandwidth, the frequency components are differentiated with each other and the produced signal have frequency component from 0 to the bandwidth of the pump  $\Delta\omega \sim 1/\tau_p \sim 10 \text{ THz}$ . Broadband THz wave detected up to 70THz was reported [42]. Figure 2-4 illustrates the schematics of the terahertz wave generation by means of optical rectification.

### 2.3.3 Generation by laser induced plasma

In 1993, *Hamster et al.* first observed terahertz emission from laser-induced plasmas [43]. This is a novel method of generating terahertz which is emitting from laser induced plasma based on amplified laser systems. The basic concept of these emitters is to focus an ultrashort high energy laser pulse in a gaseous medium such as ambient air. Reaching optical field strengths as high as  $5 \times 10^{14} \text{ W/cm}^2$  which is enough to ionize the air and form a plasma in the focal region. Up to now, there are three different approaches to generate THz wave from plasma as our knowledge:

1. Emission based on ponderomotive force

The mechanism is that the polarization produced by the free electrons that are accelerated by the ponderomotive forces associated with the propagating laser pulse, i.e. due to a spatial-temporal optical intensity gradient within the plasma. In this method, a rotationally symmetric polarization is created around the beam propagation axis, this leads to an emission of terahertz wave in a diverging cone around the optical propagation axis. Due to symmetry reasons no net terahertz field radiates along the optical propagation axis [43]. Compared to another two methods employing laser-induced plasma, the pulse energy of the generated terahertz wave using this approach is relatively low.

2. Emission based on external bias fields

This approach is applying an external bias field to the plasma region. It can increase the terahertz wave strength and to direct it into the forward direction of the optical propagation axis. The electric field amplitude of the terahertz pulse scales up linearly with the external bias field. The maximum achievable terahertz pulse energy for a given laser pulse energy is limited by the maximum external bias field [44].

3. Emission based on optical second harmonic bias

Another nonlinear optical method for THz generation was found by *Cook et al.* with later developments by other groups [45-47]. This approach is more efficient than that mentioned above. It uses the nonlinear interaction of the fundamental and the second harmonic in a plasma generated by the same laser pulses. Figure 2-5 displays the schematic of the THz generation via four-wave mixing in a plasma.

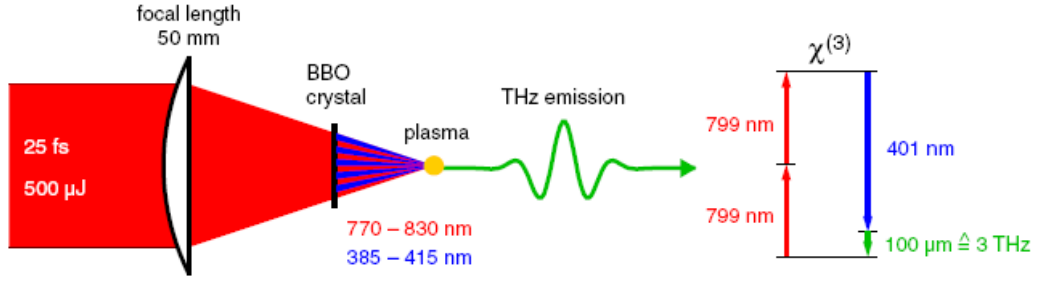


**Fig. 2-5** *Schematic of the THz generation via four-wave mixing in a plasma. The pulse at the fundamental contains wavelengths between 770 and 830 nm, the second harmonic between 385 and 415 nm.*

Thus, a complete description of this process requires the simultaneous treatment of plasma formation, of plasma dynamics, of the generation of the THz radiation and of the propagation of the THz radiation through the plasma. In the following we only consider the THz generation, i.e. we consider the plasma as a medium with optical nonlinearities. The nonlinear polarization in the focal region and the generated terahertz field amplitude are given by:

$$E_{THz}(t) \propto P_{plasma} \propto \chi^{(3)} E_{2\omega} E_{\omega}^*(t) E_{\omega}^*(t) \cos(\varphi) \quad (10)$$

where  $\chi^{(3)}(\Omega: 2\omega + \Omega, -\omega, -\omega)$  is the third order susceptibility,  $E_{\omega}$  and  $E_{2\omega}$  is the electric field of fundamental wave and the second harmonic wave, respectively.  $\varphi$ , which equals to  $k_{2\omega}\Delta l$ , is the phase difference between the fundamental and second harmonic beams,  $k_{2\omega}$  is the wave vector of the second harmonic beam and  $\Delta l$  is the path difference between the fundamental wave and the second harmonic wave along the beam propagation direction.

### 2.3.4 Detection by photoconductive antenna

In 1984, *Auston et al.* first generated and detected the THz pulses by photoconductive antennas [48]. In photoconductive antennas detection scheme, the antenna is optical gated with a femtosecond laser pulse. The gating pulse creates carriers and the terahertz pulse provides the bias field to yield a detectable current in the detection antenna. The output polarity is sensitive to the direction of the field. For several years, it was considered that the length of the optical gating pulse and the decay rate of the semiconductor were crucial to the detector responsivity and time resolution. Hence, it was assumed that no advantage could be gained from using shorter gating pulses, as the carrier lifetime of the carriers would always determine the response time of the detector. This in turn would therefore limit the detection capability of a typical GaAs photoconductive antenna to low frequencies.

### 2.3.5 Detection by electro-optical sampling

In 1995, the free space electric optical sampling (FEOS) detection scheme was first investigated by *Zhang's* group [49]. This method has widely used and allowed for coherent detection of the temporal evolution of the electric field in the ultrashort transients. Figure 2-6 displays the schematic of FEOS setup, which consists of EO crystal, quarter wave plate (or compensator), wallaston prism and balanced detector.

First, when no terahertz field experiences, the optical probe beam will not be affected by the EO crystal, then by rotating the angle of quarter wave plate, to make the polarization become circularly. This circularly polarized beam will be split into two orthogonal polarization components (*s*- and *p*-polarization) with equal intensity. The balanced detector measures the intensity difference between these two components, the value is zero. When terahertz meets the EO crystal, the electric field of the terahertz pulse will induce a small birefringence in the EO crystal through *Pockel's* effect. Passing through such crystal, the initially linearly polarized optical probe beam will change into elliptical polarization. This ellipticity is proportional to the THz electric field which applied to the crystal. Then the elliptical polarization probe beam will be split into two orthogonal polarization parts by wallaston prism. The intensity difference can be detected by balanced detector, then the THz amplitude is proportional to this signal. In general, the duration of terahertz pulse is several picosecond (or sub-picosecond) much longer than the laser pulse (femtosecond order), hence the terahertz field can be approximately treated as a dc bias field. Accordingly, the

whole terahertz time domain profile can be mapped out by scanning the delay between terahertz and probe beam.

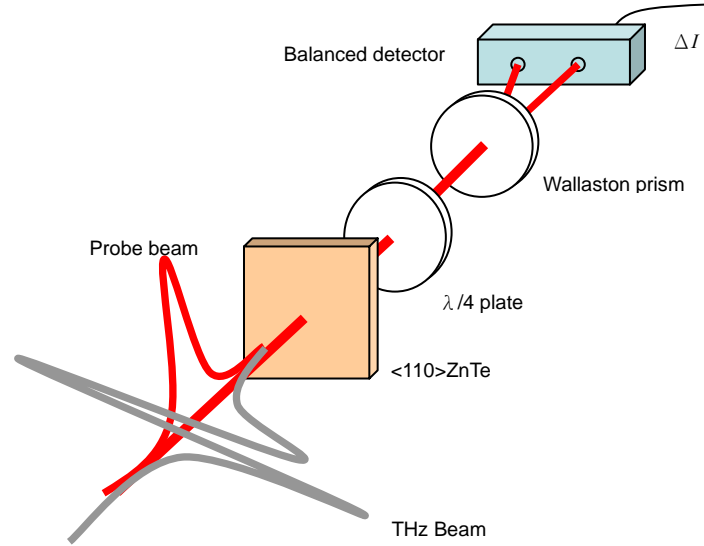


**Fig. 2-6** The scheme of EO sampling setup.

The balanced detection signal for an EO crystal such as <110> ZnTe can be calculated [50]. The ZnTe crystal is a very common EO crystal used in terahertz EO sampling. It belongs to zinc-blende structure with  $\bar{4}3m$  point group symmetry, the only non-zero coefficient of the electro tensor is  $\gamma_{41}$ .

$$\gamma_{ij} = \begin{bmatrix} 0 & 0 & 0 \\ 0 & 0 & 0 \\ 0 & 0 & 0 \\ \gamma_{41} & 0 & 0 \\ 0 & \gamma_{41} & 0 \\ 0 & 0 & \gamma_{41} \end{bmatrix} \quad (11)$$

where  $\gamma_{41} = 3.9 \text{ pm/V}$ .

Herein the angle dependence of the signal in EO sampling with (110) ZnTe is described and discussed. When an arbitrary electric field  $\vec{E} = (E_x, E_y, E_z)$  propagate along the (110)

axis is applied to the EO crystal, in the crystal axes coordinate system  $(x, y, z)$ , the refractive index ellipsoid can be written as:

$$\frac{x^2 + y^2 + z^2}{n_o^2} + 2\gamma_{41}E_x yz + 2\gamma_{41}E_y zx + 2\gamma_{41}E_z xy = 1 \quad (12)$$

After rotating the  $(x, y, z)$  coordinate system around the  $z$  axis by  $45^\circ$ , the equation (12) becomes:

$$\begin{aligned} & \frac{1}{n_o^2} \left( \frac{1}{2} \sqrt{2}x' - \frac{1}{2} \sqrt{2}y' \right)^2 + \frac{1}{n_o^2} \left( \frac{1}{2} \sqrt{2}x' + \frac{1}{2} \sqrt{2}y' \right)^2 + \frac{z'^2}{n_o^2} + 2E_x r_{41} \left( \frac{1}{2} \sqrt{2}x' + \frac{1}{2} \sqrt{2}y' \right) z' \\ & + 2E_y r_{41} \left( \frac{1}{2} \sqrt{2}x' - \frac{1}{2} \sqrt{2}y' \right) z' + 2E_z r_{41} \left( \frac{1}{2} x'^2 - \frac{1}{2} y'^2 \right) = 1 \end{aligned} \quad (13)$$

And  $E_y = -E_x$

$$x'^2 \left( \frac{1}{n_o^2} + E_z r_{41} \right) + y'^2 \left( \frac{1}{n_o^2} - E_z r_{41} \right) + \frac{z'^2}{n_o^2} + 2\sqrt{2}E_x r_{41} y' z' = 1 \quad (14)$$

Then the  $(x', y', z')$  coordinate system is rotated around the  $x'$  axis by  $\theta$ :

$$\begin{aligned} x' &= x'' \\ y' &= y'' \cos \theta - z'' \sin \theta \\ z' &= y'' \sin \theta + z'' \cos \theta \end{aligned} \quad (15)$$

The components of the electric field are expressed in terms of the angle  $\alpha$  (the angle of the THz beam polarization with respect to the  $(001)$  axis), which is shown in Fig. 2-7.

$$\begin{aligned} E_z &= E_{THz} \cos \alpha \\ E_x &= E_{THz} \frac{\sqrt{2}}{2} \sin \alpha \end{aligned} \quad (16)$$

With these definitions and some calculations, the index ellipsoid of Eq. (14) becomes:

$$\begin{aligned} & x''^2 \left( \frac{1}{n_o^2} + E_{THz} r_{41} \cos \alpha \right) + y''^2 \left\{ \frac{1}{n_o^2} - E_{THz} r_{41} [\cos \alpha \sin^2 \theta + \cos(\alpha + 2\theta)] \right\} \\ & + z''^2 \left\{ \frac{1}{n_o^2} - E_{THz} r_{41} [\cos \alpha \cos^2 \theta - \cos(\alpha + 2\theta)] \right\} = 1 \end{aligned} \quad (17)$$

And

$$\begin{aligned} 2\theta &= -\tan^{-1}(2 \tan \alpha) - n\pi \\ \left( n - \frac{1}{2} \right) \pi &\leq \alpha < \left( n + \frac{1}{2} \right) \pi, n = 0, 1, \dots \end{aligned} \quad (18)$$

By setting  $x'' = 0$  ( $y''z''$  plane), then solve the equation, we can get two eigenvalues.

$$\lambda_{1,2} = \frac{1}{n_o^2} - \gamma_{41} E_{THz} [\cos \alpha \sin^2 \theta \pm \cos(\alpha + 2\theta)] \quad (19)$$



The refractive indices for visible-near IR light propagating along the  $x''$  direction are:

$$\begin{aligned} n_{y''}(\alpha) &\approx n_0 + \frac{n_0^3}{2} E_{THz} r_{41} [\cos \alpha \sin^2 \theta + \cos(\alpha + 2\theta)] \\ n_{z''}(\alpha) &\approx n + \frac{n_0^3}{2} E_{THz} r_{41} [\cos \alpha \cos^2 \theta - \cos(\alpha + 2\theta)] \end{aligned} \quad (20)$$

The intensity detected by balance detector can be expressed as:

$$\begin{aligned} \Delta I(\alpha, \varphi) &= I_p \sin[2(\varphi - \theta)] \sin \left\{ \frac{\omega}{c} [n_{y''}(\alpha) - n_{z''}(\alpha)] L \right\} \\ &= I_p \frac{\omega n_0^3 E_{THz} r_{41} L}{2c} (\cos \alpha \sin 2\varphi + 2 \sin \alpha \cos 2\varphi) \end{aligned} \quad (21)$$

where  $L$  is crystal length,  $\varphi$  is the angle of the probe beam polarization with respect to the (001) axis, which is shown in Fig. 2-7.

The optimum signal can be realized at the largest phase retardation if  $\alpha + 2\theta = n\pi, n = 0, \pm 1, \pm 2 \dots$  which means terahertz beam should be parallel or perpendicular to probe beam to get maximum detected signal.

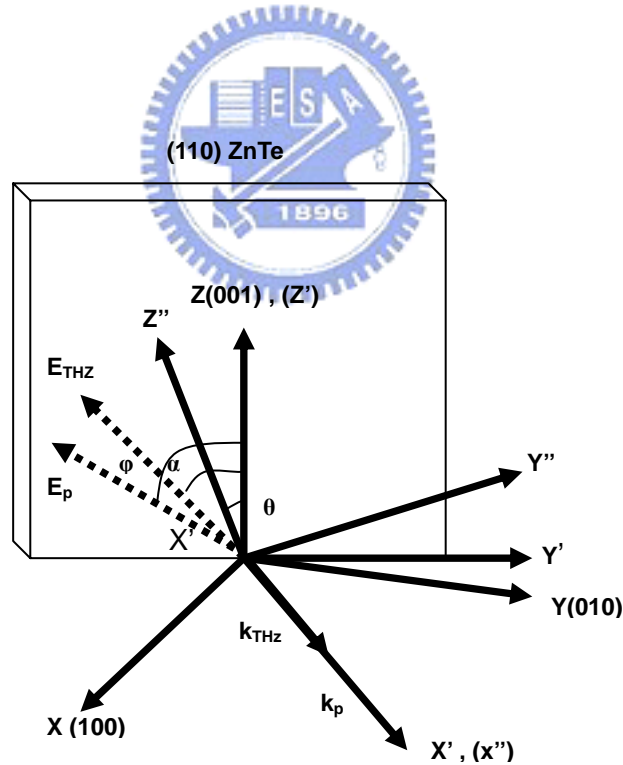


**Fig. 2-7** Angles of the THz wave and probe beam polarization directions.

## References

- [1] G. Mourou, C. V. Stancampiano, and D. Blumenthal, "Picosecond microwave pulse generation," *Appl. Phys. Lett.* **38**, 470-472 (1981).
- [2] D. H. Auston, K. P. Cheung, P. R. Smith, "Picosecond photoconducting Hertzian dipoles," *Appl. Phys. Lett.* **45**, 284-286 (1984).
- [3] C. Fattinger, and D. Grischkowsky, "Point source terahertz optics," *Appl. Phys. Lett.* **53**, 1480-1482 (1988).
- [4] N. Sarukura, H. Ohtake, S. Izumida, and Z. Liu, "High average-power THz radiation from femtosecond laser-irradiated InAs in a magnetic field and its elliptical polarization characteristics," *J. Appl. Phys.* **84**, 654-656 (1998).
- [5] X. -C. Zhang, *Perspectives in Optoelectronics*, ed. by Sudhanshu S. Jha, World Scientific, chapter 3 (1995).
- [6] Q. Wu and X. -C. Zhang, "Ultrafast electro-optic field sensors," *Appl. Phys. Lett.* **68**, 1604-1606 (1996).
- [7] T. Elsaesser, J. G. Fujimoto, D. A. Wiersma, and W. Zinth, eds., *Ultrafast Phenomena XI* (Springer-Verlag, Berlin, 1998).
- [8] C. Chudoba, E. T. J. Nibbering, and T. Elsaesser, "Site-specific excited-state solute-solvent interactions probed by femtosecond vibrational spectroscopy," *Phys. Rev. Lett.* **81**, 3010-3013 (1998).
- [9] E. J. Heilweil, "Ultrafast glimpses at water and ice," *Science* **283**, 1467-1468 (1999).
- [10] S. Woutersen, U. Emmerichs, and H. J. Bakker, "Femtosecond mid-IR pump-probe spectroscopy of liquid water: evidence for a two-component structure," *Science* **278**, 658-660 (1997).
- [11] P. Hamm, M. Lim, and R. M. Hochstrasser, "Non-Markovian dynamics of the vibrations of ions in water from femtosecond infrared three-pulse photon echoes," *Phys. Rev. Lett.* **81**, 5326-5329 (1998).
- [12] R. M. Hochstrasser, P. Hamm, and M. Lim, "Femtosecond Dynamics, two-dimensional infrared spectroscopy and echoes of protein vibrations," in *Ultrafast Phenomena XI*, T. Elsaesser, J. G. Fujimoto, D. A. Wiersma, and W. Zinth, eds. (Springer-Verlag, Berlin, 1998), pp. 653-657.
- [13] T. Elsaesser and M. Woerner, "Femtosecond infrared spectroscopy of semiconductors and semiconductor nanostructures," *Phys. Rep.* **321**, 253-305 (1999).

- [14] R. A. Kaindl, S. Lutgen, M. Woerner, T. Elsaesser, B. Nottelmann, V. M. Axt, T. Kuhn, A. Hase, and H. Kunzel, "Ultrafast dephasing of coherent intersubband polarizations in a quasi-two-dimensional electron plasma," *Phys. Rev. Lett.* **80**, 3575-3578 (1998).
- [15] S. Lutgen, R. A. Kaindl, M. Woerner, T. Elsaesser, A. Hase, H. Kunzel, M. Gulia, D. Meglio, and P. Lugli, "Nonequilibrium dynamics in a quasi-two-dimensional electron plasma after ultrafast intersubband excitation," *Phys. Rev. Lett.* **77**, 3657-660 (1996).
- [16] R. A. Kaindl, M. Woerner, T. Elsaesser, D. C. Smith, J. F. Ryan, G. A. Farnan, M. P. McCurry, and D. G. Walmsley, "Ultrafast mid-infrared response of  $\text{YBa}_2\text{Cu}_3\text{O}_{7-\delta}$ ," *Science* **287**, 470-473 (2000).
- [17] D. E. Spence, S. Wielandy, C. L. Tang, C. Bosshard, and P. Gunter, "High-average power, high-repetition rate femtosecond pulse generation in the 1–5  $\mu\text{m}$  region using an optical parametric oscillator," *Appl. Phys. Lett.* **68**, 452-454 (1996).
- [18] C. McGowan, D. T. Reid, M. Ebrahimzadeh, and W. Sibbett, "Femtosecond pulses tunable beyond 4  $\mu\text{m}$  from a KTA-based optical parametric oscillator," *Opt. Commun.* **134**, 186-190 (1997).
- [19] V. Petrov and F. Noack, "Tunable femtosecond optical parametric amplifier in the mid-infrared with narrow-band seeding," *J. Opt. Soc. Am. B* **12**, 2214-2221 (1995).
- [20] G. M. Gale, G. Gallot, F. Hache, and R. Sander, "Generation of intense highly coherent femtosecond pulses in the mid infrared," *Opt. Lett.* **22**, 1253-1255 (1997).
- [21] A. Lohner, P. Kruck, and W. W. Ruhle, "Generation of 200 femtosecond pulses tunable between 2.5 and 5.5  $\mu\text{m}$ ," *Appl. Phys.* **59**, 211-213 (1994).
- [22] T. Elsaesser and M. C. Nuss, "Femtosecond pulses in the mid-infrared generated by downconversion of a traveling-wave dye laser," *Opt. Lett.* **16**, 411-413 (1991).
- [23] C. Ludwig, W. Frey, M. Woerner, and T. Elsaesser, "Generation of synchronized femtosecond pulses independently tunable in the mid-infrared," *Opt. Commun.* **102**, 447-451 (1993).
- [24] M. R. X. de Barros, R. S. Miranda, T. M. Jedju, and P. C. Becker, "High-repetition rate femtosecond mid-infrared pulse generation," *Opt. Lett.* **20**, 480-482 (1995).
- [25] V. Petrov, F. Rotermund, and F. Noack, and P. Schunemann, "Femtosecond parametric generation in  $\text{ZnGeP}_2$ ," *Opt. Lett.* **24**, 414-416 (1999).
- [26] F. Seifert, V. Petrov, and M. Woerner, "Solid-state laser system for the generation of mid infrared femtosecond pulses tunable from 3.3 to 10  $\mu\text{m}$ ," *Opt. Lett.* **19**, 2009-2011 (1994).

- [27] P. Hamm, M. Lim, and R. M. Hochstrasser, "Vibrational energy relaxation of the cyanide ion in water," *J. Chem. Phys.* **107**, 10523-10531 (1997).
- [28] J. M. Fraser, D. Wang, A. Hache, G. R. Allan, and H. M. van Driel, "Generation of high-repetition rate femtosecond pulses from 8 to 18  $\mu\text{m}$ ," *Appl. Opt.* **36**, 5044-5047 (1997).
- [29] S. Ehret and H. Schneider, "Generation of subpicosecond infrared pulses tunable between 5.2 and 18  $\mu\text{m}$  at a repetition rate of 76 MHz," *Appl. Phys.* **66**, 27-30 (1998).
- [30] R. A. Kaindl, F. Eickemeyer, M. Woerner, and T. Elsaesser, "Broadband phasematched difference frequency mixing of femtosecond pulses in GaSe: experiment and theory," *Appl. Phys. Lett.* **75**, 1060-1062 (1999).
- [31] I. M. Bayanov, R. Danielus, P. Heinz, and A. Seilmeier, "Intense subpicosecond pulses tunable between 4  $\mu\text{m}$  and 20  $\mu\text{m}$ ," *Opt. Commun.* **113**, 99-104 (1994).
- [32] T. Dahinten, U. Plodereder, A. Seilmeier, K. L. Vodopyanov, K. R. Allakhverdiev, and Z. A. Ibragimov, "Infrared pulses of 1 picosecond duration tunable between 4  $\mu\text{m}$  and 18  $\mu\text{m}$ ," *IEEE J. Quantum Electron.* **29**, 2245-2250 (1993).
- [33] A. Dhirani and P. Guyot-Sionnest, "Efficient generation of infrared picosecond pulses from 10 to 20  $\mu\text{m}$ ," *Opt. Lett.* **20**, 1104-1106 (1995).
- [34] P. Y. Han and X. -C. Zhang, "Coherent broadband midinfrared terahertz beam sensors," *Appl. Phys. Lett.* **73**, 3049-3051 (1998).
- [35] A. Bonvalet, M. Joffre, J. L. Martin, and A. Migus, "Generation of ultrabroadband femtosecond pulses in the midinfrared by optical rectification of 15 fs light pulses at 100 MHz repetition rate," *Appl. Phys. Lett.* **67**, 2907-2909 (1995).
- [36] M. Joffre, A. Bonvalet, A. Migus, and J. -L. Martin, "Femtosecond diffracting Fourier-transform infrared interferometer," *Opt. Lett.* **21**, 964-966 (1996).
- [37] A. Leitenstorfer, S. Hunsche, J. Shah, M. C. Nuss, and W. H. Knox, "Detectors and sources for ultrabroadband electrooptic sampling: experiment and theory," *Appl. Phys. Lett.* **74**, 1516-1518 (1999).
- [38] J. L. Oudar, Ph. J. Kupecek, and D. S. Chemla, "Medium infrared tunable down conversion of a YAG-pumped infrared dye laser in gallium selenide," *Opt. Commun.* **29**, 119-122 (1979).
- [39] R. A. Kaindl, M. Wurm, K. Reimann, P. Hamm, A. M. Weiner, and M. Woerner, "Generation, shaping, and characterization of intense femtosecond pulses tunable from 3 to 20  $\mu\text{m}$ ," *J. Opt. Soc. Am. B* **17**, 2086-2094 (2000).

- [40] W. Shi, Y. J. Ding, X. Mu, and N. Fernelius, "Tunable and coherent nanosecond radiation in the range of 2.7–28.7 mm based on difference-frequency generation in gallium selenide," *Appl. Phys. Lett.* **80**, 3889-3891 (2002).
- [41] M. Tani, M. Herrmann, and K. Sakai, "Generation and detection of terahertz pulsed radiation with photoconductive antennas and its application to imaging, *Meas. Sci. Technol.* **13**, 1739-1745 (2002).
- [42] A. Leitenstorfer, S. Hunsche, J. Shah, M. C. Nuss, and W. H. Knox, "Detectors and sources for ultrabroadband electro-optic sampling: Experiment and theory," *Appl. Phys. Lett.* **74**, 1516-1518 (1999).
- [43] H. Hamster, A. Sullivan, S. Gordon, W. White, and R. W. Falcone, "Subpicosecond, electromagnetic pulses from intense laser-plasma interaction," *Phys. Rev. Lett.* **71** 2725-2728 (1993).
- [44] T. Löffler, F. Jacob, and H. G. Roskos, "Generation of terahertz pulses by photoionization of electrically biased air," *Appl. Phys. Lett.* **77**, 453-455 (2000).
- [45] D. J. Cook, and R. M. Hochstrasser, "Intense terahertz pulses by four-wave rectification in air," *Opt. Lett.* **25** 1210-1212 (2000).
- [46] T. Bartel, P. Gaal, K. Reimann, M. Woerner, and T. Elsaesser, "Generation of single-cycle THz transients with high electric-field amplitudes," *Opt. Lett.* **30**, 2805-2807 (2005).
- [47] X. Xie, J. Dai, and X. -C. Zhang, "Coherent control of THz wave generation in ambient air," *Phys. Rev. Lett.* **96** 075005-1-4 (2006).
- [48] D. H. Auston, K. P. Cheung, and P. R. Smith, "Picosecond photoconducting Hertzian dipole," *Appl. Phys. Lett.* **45**, 284-286 (1984).
- [49] Q. Wu, and X. -C. Zhang, "Free-space electro-optic sampling of terahertz beams," *Appl. Phys. Lett.* **67**, 3523-3525 (1995).
- [50] P. C. M. Planken, H. K. Nienhuys, H. J. Bakker, and T. Wenckebach, "Measurement and calculation of the orientation dependence of terahertz pulse detection in ZnTe," *J. Opt. Soc. Am. B* **18**, 313-317 (2001).

## Chapter 3

# Optical properties and potential applications of $\epsilon$ -GaSe crystal in terahertz frequencies

### 3.1 Introduction

The terahertz (THz) spectrum ( $\sim 0.1$ – $10$  THz) has recently attracted considerable interest because of its potential in both fundamental physics and an increasing range of applications. For instance, various molecules have distinctive dispersive and absorptive properties at terahertz spectral frequencies. In particular, recent progress in both time-domain and time-resolved THz spectroscopy has advanced understanding of the nature of molecular vibrations, protein kinetics, carrier dynamics in semiconductors and other phenomena [1-3]. In the past, ultrafast laser pulses have been required to generate broadband terahertz pulses based on optical rectifications and photoconductions. Coherent broad-bandwidth THz pulses generated by optical rectifications [4] are highly useful for time-resolved spectroscopic applications. To probe the nonlinear response of material in the far-infrared region, high-energy THz pulse generation by optical rectification in a large-aperture ZnTe single crystal has been recently reported [5]. In addition to optical rectifications, other parametric processes in nonlinear crystals can efficiently convert optical pulses to terahertz waves. For example, the terahertz parametric oscillation in a LiNbO<sub>3</sub> crystal has been used to generate a pulse energy of  $\sim 10$  pJ [6]. Recently, two coherent infrared laser beams were mixed in nonlinear optical crystals such as GaSe [7], ZnGeP<sub>2</sub> [8] and GaP [9], to generate efficiently terahertz waves with extremely wide tuning ranges and high peak powers. Accordingly, a figure of merit,  $d_{eff}^2/n^3\alpha^2$ , which can conveniently represents the efficiency of generation of terahertz output, is proposed, where  $d_{eff}$  is the effective nonlinear coefficient;  $n$  is the index of refraction, and  $\alpha$  is the absorption coefficient at the terahertz frequencies.

Gallium selenide (GaSe) has been recently identified as a promising semiconductor crystal for nonlinear optics and terahertz photonics applications because of its high nonlinearity [10, 11]. It has been successfully employed to generate coherent radiation in the mid-infrared and even down to the terahertz frequency range using difference-frequency generation (DFG) or phase-matched optical rectification [7, 12]. The widest tuning range

covers wavelengths from 58.2  $\mu\text{m}$  to 3.54 mm and is associated with o-ee phase-matched difference frequency generation (DFG). On the high-frequency side of the reststrahlen band, tuning in the range 2.7–38.4  $\mu\text{m}$  was performed using an e-oo phase-matching configuration. The output peak powers were measured to be 389 W and 4.7 W at wavelengths of 203  $\mu\text{m}$  and 1 mm, respectively. GaSe is also becoming the material of choice for broadband terahertz detectors [13]. Given the above findings, the optical properties of GaSe crystal are practically important to several terahertz devices. Optical constants near the absorption edge and over a wide spectral range from near-infrared to far-infrared continue to be studied actively [14-19]. The dielectric response, optical constants and nonlinear optical properties of the GaSe crystals in the terahertz range were recently investigated by terahertz time-domain spectroscopy (THz-TDS) and other parametric processes [20-23]. Numerous optical measurements and phonon modes of the *p*-GaSe crystal have also been reported [24]. Unfortunately, the available data on optical properties, including refractive index and absorption coefficient, of GaSe crystal in the terahertz region are inconsistent.

This work experimentally elucidates the optical constants, including the real and imaginary parts of the ordinary dielectric function, over a wide range of terahertz frequencies. Fitting to experimental results yields a revised complex ordinary and extraordinary dielectric function for GaSe crystal. The phonon vibrational modes and overtones on the wide terahertz frequencies are well-examined. The high magnitude of the figure of merit and the large birefringence of a GaSe crystal are also identified. Based on the superior optical properties of GaSe crystal at terahertz frequencies, a THz phase modulator design is presented for potential applications.

### **3.2 Sample preparation and experimental method**

The GaSe crystals adopted in this work were grown using the Bridgman method. Raw materials were placed in a well-cleaned quartz tube, sealed and then pumped down to below  $10^{-6}$  Torr. Crystals were grown at a thermal gradient of 30  $^{\circ}\text{C}/\text{cm}$  with a growth rate of 2 cm/day. The resulting pure GaSe crystal exhibited the characteristic appearance of a (001) hexagonal layered structure. The optical transmission of a thin GaSe crystal of thickness  $\sim 170$   $\mu\text{m}$  was determined using a Bruker IFS66v/S spectrometer (Fourier transform infrared spectrometer - FTIR) over a wide range of frequencies ( $60\text{--}4000$   $\text{cm}^{-1}$ ). The power reflectivity from the thick GaSe crystal (thickness  $\sim 3$  mm) surface was also measured by the specular reflection method with an oblique angle of incidence ( $\theta\sim 11^{\circ}$ ) using the FTIR.



Three GaSe crystals with different thicknesses 287  $\mu\text{m}$ , 1110  $\mu\text{m}$  and 2021  $\mu\text{m}$  were prepared for the THz-TDS measurement. A home-made antenna-based THz-TDS system with a collimated beam at the sample position was used [25], as shown in Fig. 3-1. Briefly, terahertz pulses generated from femtosecond laser-excited dipole-type antenna fabricated on low-temperature-grown GaAs were collimated by an off-axis paraboloidal mirror and propagated through the GaSe sample at normal incidence. The transmitted terahertz pulses were focused on another dipole-type antenna that was gated by time-delayed probe pulses and oriented to detect terahertz waves that were polarized parallel to the incident terahertz wave polarization. The diameter of the beam of the terahertz wave through the GaSe sample was approximately 0.6 cm. The terahertz spectrometer was purged with nitrogen and maintained at a relative humidity of  $3.0\pm 0.5\%$ .

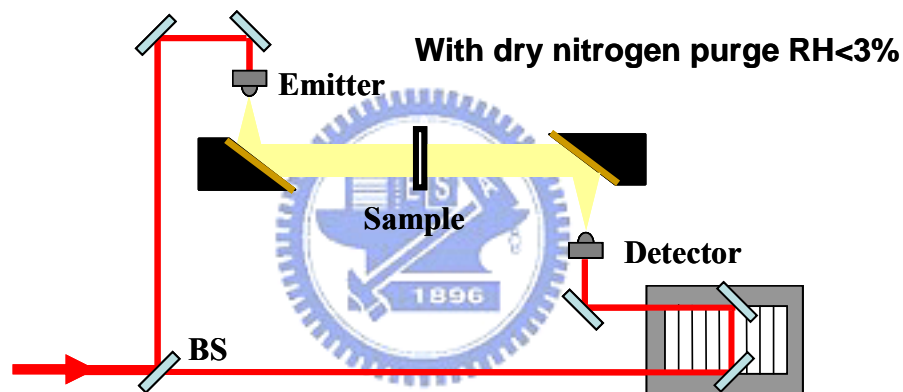


*Fig. 3-1 A general sketch of the home-made terahertz time-domain spectroscopy (THz-TDS) system. Laser source : Ti: sapphire femtosecond laser with wavelength~800nm; Repetition rate~82MHz; Pulse duration~50fs; THz emitter and detector : LT- GaAs photoconductive antenna with Si lens.*

### 3.3 Analysis model of optical constant from THz-TDS

We assume that the terahertz signal is a plane wave passing through the crystal at normal incidence. In order to compare the recorded signal transmitting through GaSe crystal, we treat the signal passing through the purged nitrogen  $\text{N}_2$  as a reference. In Fig. 3-2, the terahertz signal,  $E_0(f)$ , is passing through the crystal (thickness:  $d_s$ ) at normal incidence. The electric field of the terahertz wave transmitted through the  $\text{N}_2$  area and GaSe crystal at a frequency,  $f$ , can be expressed as  $E_{ref}(t)$  and  $E_S(t)$ , respectively.

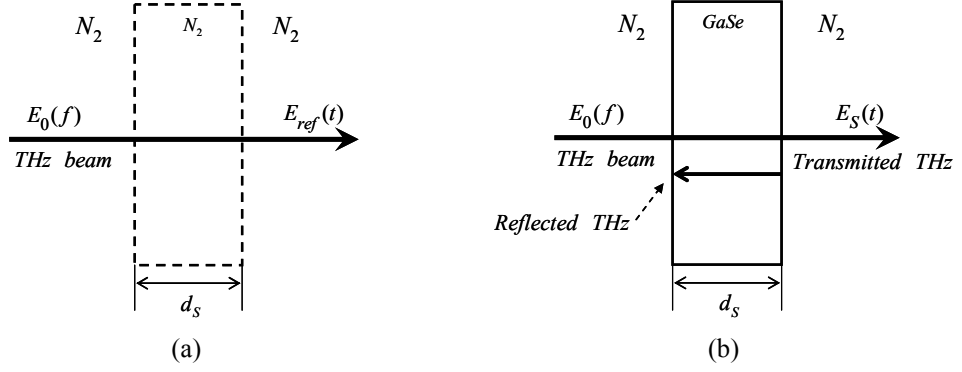


**Fig. 3-2** A general sketch of the (a) reference-purged  $N_2$  and (b) sample-GaSe crystal for the optical constants measurement in the terahertz time-domain spectroscopy (THz-TDS) experiment.

The electric field of the terahertz wave transmitted through the  $N_2$  area at the frequencies  $f$ , can then be written as:

$$E_{ref}(t) = \int_{-\infty}^{\infty} E_0(f) \times e^{i2\pi f \left(\frac{\tilde{n}_A d_s}{c}\right)} \times e^{-i2\pi ft} df \quad (1)$$

where  $E_0(f)$  is the electric field of the incident terahertz wave,  $\tilde{n}_A$  is the complex refractive index of  $N_2$  ( $\tilde{n}_A = 1$ ), and  $d_s$  is the thickness of GaSe crystal. Similarly, the electric field of the terahertz wave transmitted through the GaSe crystal can be expressed as:

$$E_S(t) = \int_{-\infty}^{\infty} E_0(f) \times \tilde{t}_{AS} \times FP_{GaSe}(f, d_s) \times \tilde{t}_{SA} \times e^{-i2\pi ft} df \quad (2)$$

where  $\tilde{t}_{AS} = 2 \times \tilde{n}_A / (\tilde{n}_A + \tilde{n}_S)$  and  $\tilde{t}_{SA} = 2 \times \tilde{n}_S / (\tilde{n}_S + \tilde{n}_A)$  are the complex transmission coefficients at the  $N_2$ -GaSe and GaSe- $N_2$  interfaces, respectively.  $\tilde{n}_S$ , which is the complex refractive index of GaSe crystal, is either the ordinary index ( $\tilde{n}_o = n_o + i\kappa_o$ ) or extraordinary index ( $\tilde{n}_e = n_e + i\kappa_e$ ) of the GaSe crystal. In this work, the terahertz wave is normal incident, and the complex refractive index is defined as  $\tilde{n}_o$ . The Fabry-Perot coefficient in the GaSe crystal with a thickness of  $d_s$  is  $FP_{GaSe}(f, d_s)$

$$FP_{GaSe}(f, d_s) = \sum_{m=0}^N \left[ \tilde{r}_{SA}^{2m} e^{i2\pi f \left(\frac{\tilde{n}_S d_s}{c} (2m+1)\right)} \right] \quad (3)$$

where  $\tilde{r}_{SA}$  is the complex reflective coefficient at the GaSe-N<sub>2</sub> interface. The number of times for multiple internal reflections is considered from m=0 to N. (N is a variable in this calculation).

Complex transmittance of the sample is represented in terms of Eq. (1) and (2) as:

$$\begin{aligned} & \sqrt{\frac{T_S}{T_{ref}}} e^{i(\phi_S - \phi_{ref})} \\ &= \frac{E_S(t)}{E_{ref}(t)} \\ &= \left[ \tilde{t}_{AS} \tilde{t}_{SA} \sum_{m=0}^N \left[ \tilde{r}_{SA} e^{i2\pi f \left( \frac{\tilde{n}_S d_S}{c} \right)} \right]^{2m} e^{\frac{-2\pi f}{c} [(\kappa_S - \kappa_A) d_S]} \right] \times e^{\frac{i2\pi f}{c} [(n_S - n_A) d_S]} \end{aligned} \quad (4)$$

where  $\sqrt{T_S/T_{ref}}$  and  $\phi_S - \phi_{ref}$  indicate the power transmittance and the phase shift, respectively. From Eq. (4), the complex refractive index  $\tilde{n}_S = n_S + i\kappa_S$  is derived as follows:

$$\begin{aligned} n_S &= \frac{1}{2\pi f \frac{d_S}{c}} \left[ (\phi_S - \phi_{ref}) - \arg \left( \tilde{t}_{AS} \tilde{t}_{SA} \sum_{m=0}^N \left[ \tilde{r}_{SA} e^{i2\pi f \left( \frac{\tilde{n}_S d_S}{c} \right)} \right]^{2m} \right) \right] + n_A \\ \kappa_S &= \frac{1}{-2\pi f \frac{d_S}{c}} \ln \left[ \frac{\sqrt{\frac{T_S}{T_{ref}}}}{\left[ \tilde{t}_{AS} \tilde{t}_{SA} \sum_{m=0}^N \left[ \tilde{r}_{SA} e^{i2\pi f \left( \frac{\tilde{n}_S d_S}{c} \right)} \right]^{2m} \right]} \right] + \kappa_A \end{aligned} \quad (5)$$

## 3.4 Results and Discussions

### 3.4.1 Raman spectroscopy

The Raman scattering measurements were performed by a Jobin-Yvon U1000 Raman system. The Raman spectra were excited by means of the 514.5 nm line from an Argon-ion laser with a filter to filter out the Rayleigh scattering of the laser. Raman signals were collected by the double-grating spectrometer and detected by a LN<sub>2</sub> cooled charge coupled device (CCD). The measured Raman spectra data are presented in Fig. 3-3. There are several Raman active phonon frequencies at 78 cm<sup>-1</sup>, 115.3 cm<sup>-1</sup>, 133.0 cm<sup>-1</sup>, 211.5 cm<sup>-1</sup>, 250 cm<sup>-1</sup> and 306.6 cm<sup>-1</sup> for GaSe crystal. These phonon modes could be provided the correct assignments according to some published literature [24, 27]. Some low frequency

bands, such as  $19\text{ cm}^{-1}$  and  $60\text{ cm}^{-1}$ , were not observed because of the noise background from the laser system.

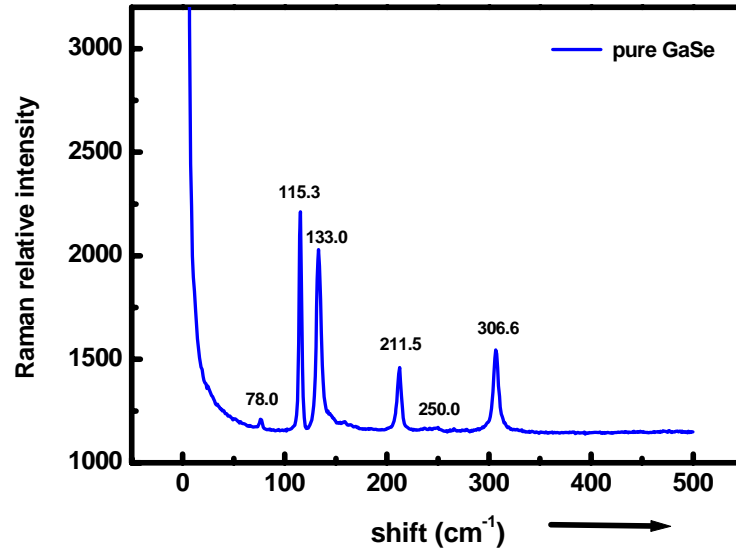


*Fig. 3-3 Raman spectra of GaSe crystal. Several Raman active phonon modes could be identified in this measurement.*

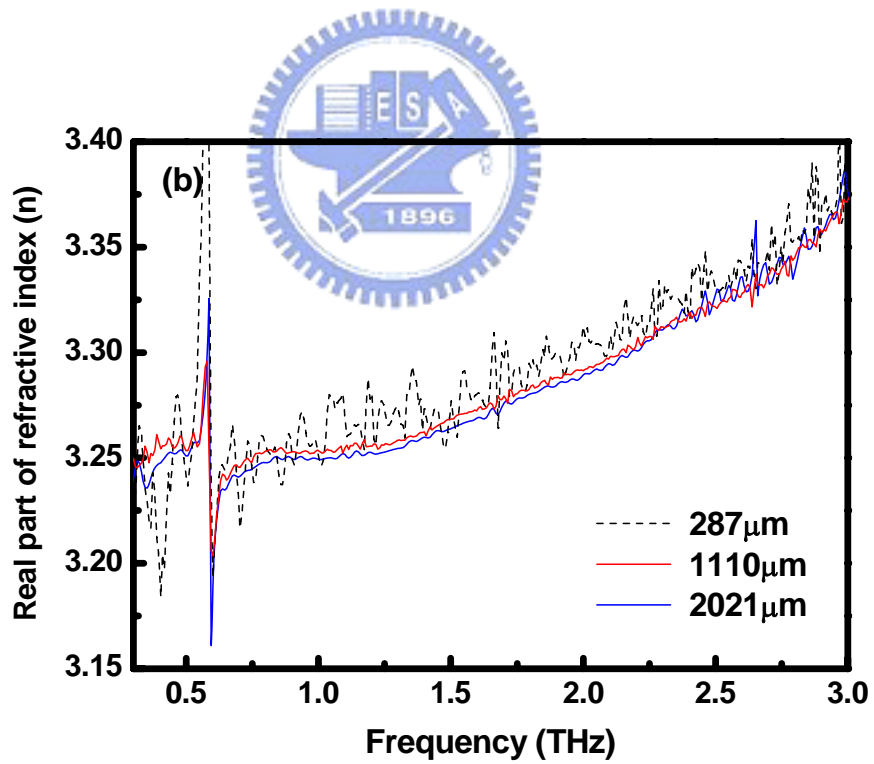
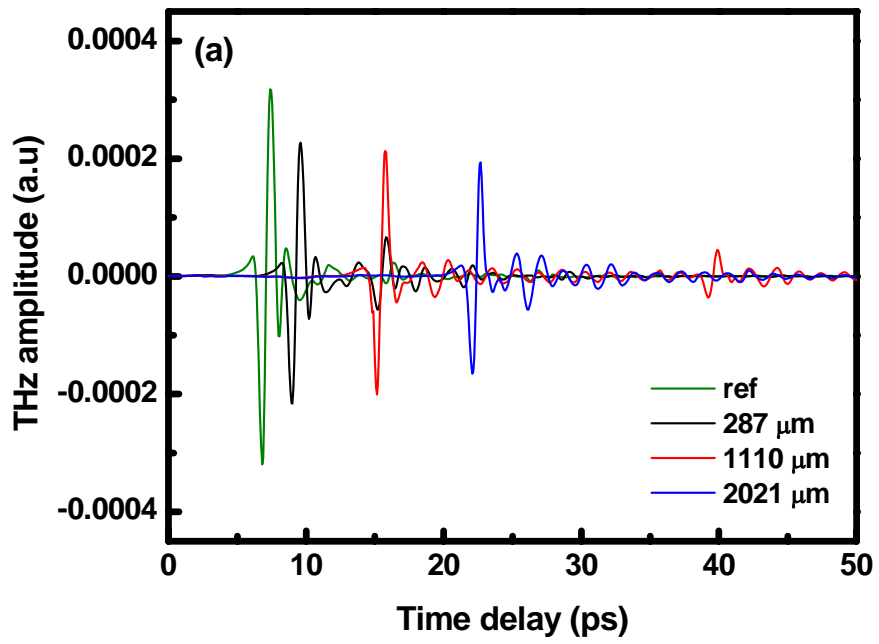


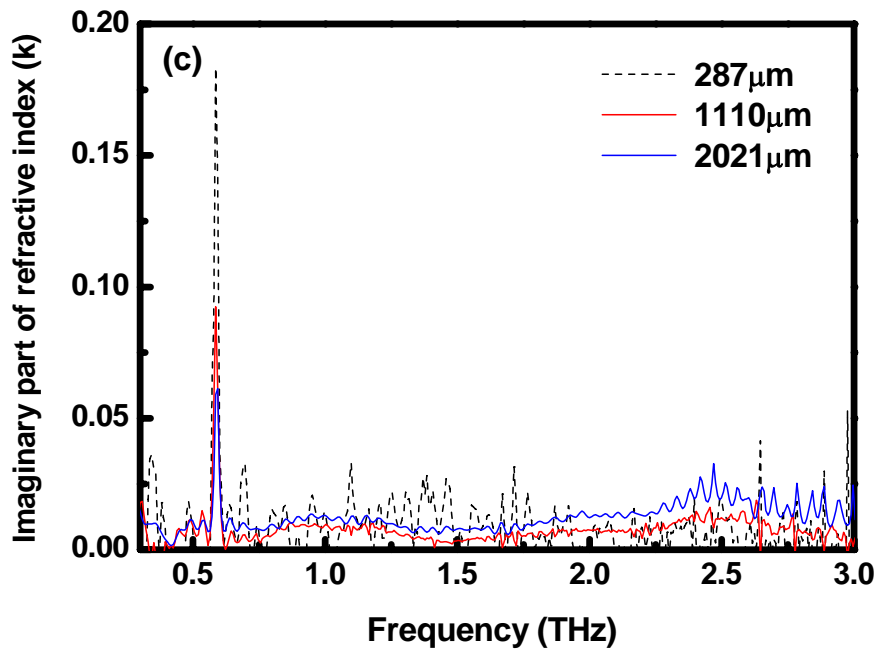
### 3.4.2 Optical constant measurement by THz-TDS

Figure 3-4(a) presents the temporal waveforms in THz-TDS without and with the GaSe sample for different sample thicknesses ( $d=287, 1110, 2021\ \mu\text{m}$ ). The measurement of the time delay  $\Delta t$  yields the group index of refraction  $n=1+c\Delta t/d$ , where  $d$  is the thickness of the sample, and  $c$  is the speed of light in a vacuum. For instance, the delay due to the sample index and thickness is experimentally determined to be  $\Delta t=15.21\pm 0.03\text{ ps}$  for  $d=2021\ \mu\text{m}$ . The calculated group index of refraction  $n$  is 3.26. Based on iterative calculation procedures, the real part of the complex ordinary refractive index, presented in Fig. 3-4(b), is about 3.23–3.37 ( $\pm 0.005$ ) in the range from 0.2 THz to 3 THz. The result for  $n_o$  in 0.2–3 THz at room temperature is consistent with the resulting delay-time in the aforementioned terahertz temporal profiles. The extracted values of the real part of the complex ordinary refractive index from three crystals of different thicknesses are mutually consistent. The relatively clear separation in the time domain of the main transmitted pulse and the first internal reflection facilitated the data analysis for the main pulse in the thick samples ( $d=1110\ \mu\text{m}$ ,

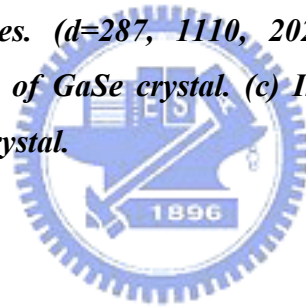
2021  $\mu\text{m}$ ). Furthermore, the calculated real part of the complex ordinary refractive index from the thin sample ( $d=287 \mu\text{m}$ ) has a poorer signal and noise ratio than that from thick sample, probably because the thinner sample has a shorter interaction length with the terahertz wave, such that the relevant extracted data are less correct. However, measurements of the thin sample include a severe Fabry-Perot effect: the main peak and the multiple reflection peaks will mix together such that the extracted data are associated with a worse S/N ratio. Nevertheless, the mean value of the real part of the complex ordinary refractive index measured from the thin sample is very close to that measured from the thick samples. A significant phonon resonance feature is determined as in the thick samples.

The refractive index  $n$  of a dispersive medium depends on frequency. In regions of the spectrum where the material does not absorb, the real part of the complex refractive index ( $n$ ) tends to increase with frequency. Near anomalous dispersion and resonant absorption, the curve of the refractive index declines with frequency [26]. The GaSe crystal is a dielectric medium, with the expected dispersive behavior in the terahertz frequencies, according to our measurements. The absorption spectrum, which is shown in Fig. 3-4(c), clearly includes an absorption peak at around 0.586 THz ( $19.5 \text{ cm}^{-1}$ ), corresponding to the ringing in the time-domain waveform in Fig. 3-4(a). The presence of the low-frequency sharp peak of the “rigid layer mode” at 0.586 THz indicates that the pure GaSe crystal is in the  $\epsilon$ -phase. This result is confirmed by the extracted index of refraction  $n_o$ , presented in Fig. 3-4(b). As expected, the line-shape of the real part exhibits dispersive behavior close to the absorption peak. Away from resonance, the real part remains smooth. Figure 3-4(c) shows the extinction coefficient  $k$  to be about  $0.0015-(0.020\pm 0.012)$  outside the absorption peak. This value corresponds to an absorption coefficient of under  $20 \text{ cm}^{-1}$  in the 0.2–3 THz frequency range.





*Fig. 3-4 (a) Time profiles of terahertz pulse transmitted through GaSe crystals of various thicknesses. ( $d=287, 1110, 2021 \mu\text{m}$ ) (b) Real part of complex refractive index  $n$  of GaSe crystal. (c) Imaginary part of complex refractive index  $k$  of GaSe crystal.*



### 3.4.3 Optical properties measurement by transmitted FTIR

Fourier-Transform Infrared transmission spectra are useful for characterizing phonon vibration frequencies. Our earlier works have identified some overtones and multi-phonon process modes [18, 19]. Figure 3-5 depicts the experimental absorption spectrum of the pure GaSe crystal in the wide wavelength range (3–700  $\mu\text{m}$ ). The measurements reveal no absorption modes in the transparency window ( $<18 \mu\text{m}$ ). Some other IR-active modes at 19.6  $\mu\text{m}$  ( $510 \text{ cm}^{-1}$ ), 22.4  $\mu\text{m}$  ( $446 \text{ cm}^{-1}$ ), 24.4  $\mu\text{m}$  ( $410 \text{ cm}^{-1}$ ) and 27.6  $\mu\text{m}$  ( $362 \text{ cm}^{-1}$ ) are identified. These modes are assigned to the difference frequency combinations of acoustic and optical phonons or the impurity-induced localized modes. For instance, the band at 24.4  $\mu\text{m}$  is the overtone of the IR active mode at 46.8  $\mu\text{m}$ . The band at 27.6  $\mu\text{m}$  originates in the multi-phonon processes, while the two bands at 19.6  $\mu\text{m}$  and 22.4  $\mu\text{m}$  follow mainly from the impurity-induced localized modes [20, 24, 27, 28].



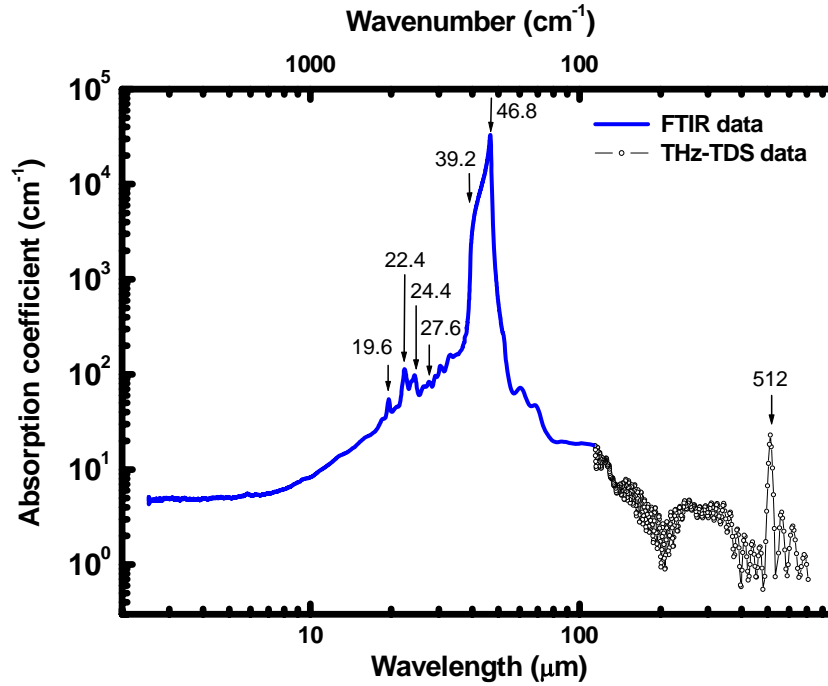


**Fig. 3-5** Absorption spectrum of pure GaSe crystal from 3  $\mu\text{m}$  to 700  $\mu\text{m}$ .

In principle, the optical medium indeed absorbs very strongly whenever the photon is close to resonance with the TO phonon. The fundamental optical properties of a dielectric, including the absorption, refraction and reflectivity, are all related to each other, because they are all determined by the complex dielectric function. At frequencies in the reststrahlen band between transverse (TO) and longitudinal (LO) optical phonons, no mode can propagate and so all of the incident photons are reflected. The *Kramers-Kronig* analysis of a reflection spectrum from a single interface was used to determine the complex refractive index in elsewhere [29]. Figure 3-5 displays the strong infrared absorption peak in the reststrahlen band. The phonon modes and absorption coefficient are determined by measuring the crystal surface reflectivity, as follows.

### 3.4.4 Optical properties measurement by reflected FTIR

Figure 3-6 shows power reflectance, which yields information about optical phonons in the reststrahlen band. After the experimental data are fitted, the transverse and longitudinal optical phonons ( $\omega_{TO}$  and  $\omega_{LO}$ ) are identified at 46.8  $\mu\text{m}$  (6.39 THz; 213.5  $\text{cm}^{-1}$ ) ( $E'(TO)$ )

and  $39.2 \mu\text{m}$  ( $7.62 \text{ THz}$ ;  $255 \text{ cm}^{-1}$ ) ( $E'(LO)$ ), respectively, for an ordinary refractive index. Both assigned phonon modes in the reststrahlen band in our studies are consistent with those reported elsewhere [10, 18]. The infrared active phonons identified by the specular reflection measurements verify that the GaSe crystal is in the  $\varepsilon$ -phase.

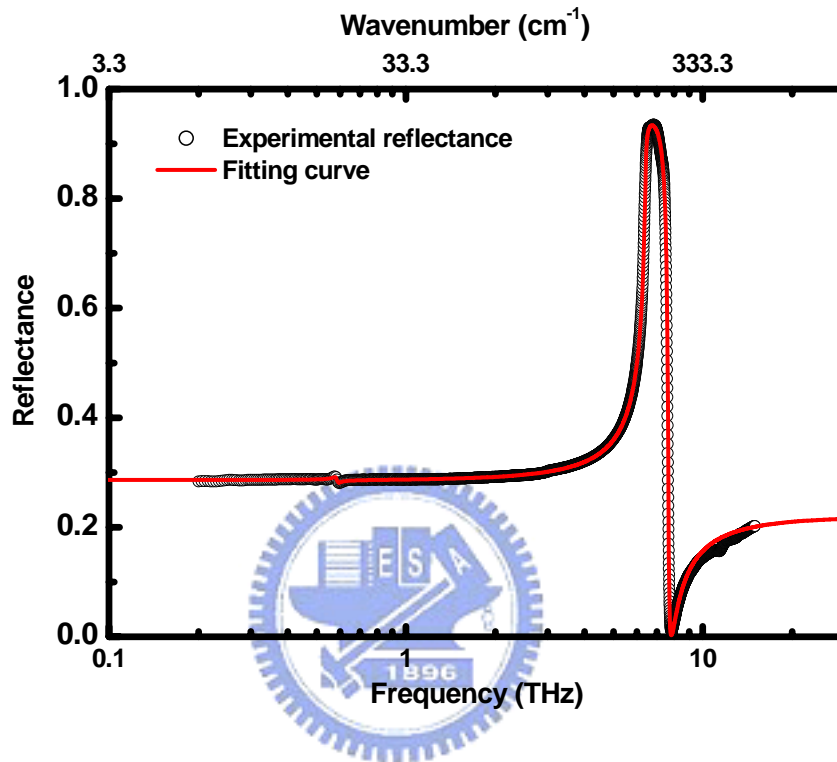


*Fig. 3-6 Power reflectance measurement over wide range of terahertz frequencies. A strong infrared absorption peak in the range 6–8 THz, called the reststrahlen band, is observed.*

### 3.4.5 Ordinary and extraordinary dielectric function determination

The calculated power reflectance in the range 0.2 to 3 THz is obtained using the parameters that govern the optical constants derived from the THz-TDS. Combining the experimental measurements from THz-TDS and FTIR yields the power reflectance over a wide frequency range. Moreover, based on the parameters given elsewhere [10], a complex ordinary dielectric function is developed theoretically to fit our data, as presented as the red solid-line in Fig. 3-6. The complex ordinary dielectric function  $\varepsilon_o(\omega)$  is modified slightly, by

introducing a corrected damped harmonic oscillator term. The expression as a function of wave-number,  $\omega$ , is

$$\varepsilon_o(\omega) = A\omega^6 + B\omega^4 + C\omega^2 + S_1 + \frac{(\omega_L^2 - \omega_T^2)S_1}{\omega_T^2 - \omega^2 - i\Gamma_1\omega} + \frac{\omega_i^2 S_2}{\omega_i^2 - \omega^2 - i\Gamma_2\omega} \quad (6)$$

where  $A=6.105 \times 10^{-27} \text{ cm}^6$ ,  $B=1.8564 \times 10^{-18} \text{ cm}^4$ ,  $C=4.0499 \times 10^{-9} \text{ cm}^2$ ,  $S_1=7.37$ ,  $S_2=0.017$ ,  $\Gamma_1=2.8 \text{ cm}^{-1}$ ,  $\Gamma_2=0.5667 \text{ cm}^{-1}$ ,  $\omega_L=255 \text{ cm}^{-1}$ ,  $\omega_T=213.5 \text{ cm}^{-1}$  and  $\omega_i=19.53 \text{ cm}^{-1}$ . Although the parameters of  $A$ ,  $B$  and  $C$  are insignificant for the fitted result, we still include these for the formula more completely in order to deduce the following Sellmeier equations. The *Kramers-Kronig* analysis of the power reflectance data yields values for the transverse and longitudinal optical phonon modes of  $\omega_T=213.5 \text{ cm}^{-1}$  and  $\omega_L=255 \text{ cm}^{-1}$ , respectively, in the reststrahlen band.

Figures 3-7(a) and (b) display the experimentally measured optical constants ( $n$ : refractive index;  $\alpha$ : absorption coefficient), which are compared with previously published data. The figure includes the real and imaginary parts of the proposed fitted dielectric function, the ordinary index of refraction and the absorption coefficient. In Fig. 3-7(a), the revised real part of the ordinary dielectric function fits well with the experimental data in the terahertz range. Additionally, the deviation between the imaginary part of the ordinary dielectric function fitted curve and the experimental data in Fig. 3-7(b) is caused mainly by the scattering absorption loss because of the imperfect crystallinity of the crystal.

The Sellmeier equation is an empirical formula that effectively describes dispersion. The modified Sellmeier equation coefficients for the pure GaSe crystal suitable over various frequency ranges were experimentally proposed [18, 30, 31]. In particular, *Shi et al.* utilized the dispersion relation of *Vodopyanov* to confirm the phase matching condition for terahertz generation by applying difference-frequency mixing [32]. Furthermore, in our previous investigations [18], the revised Sellmeier equations were expected to be accurate over the spectral range of 2.4–35  $\mu\text{m}$  and were experimentally verified from 2.4 to 28  $\mu\text{m}$ . *Piccioli et al.* theoretically fitted their data to propose the complex dielectric function [10, 15]. In Figs. 3-7(a) and (b), the solid-lines represent the calculated dielectric functions reported in the literature [10, 18 and 30], which are separated to yield the ordinary  $n_o$  and  $\alpha_o$ . The optical constants measured herein agree closely the data published elsewhere [22]. The measured sharp phonon resonance mode at 0.586 THz is verified in that work [22]. Other studies have also obtained optical constants using THz-TDS in the terahertz range [20, 21]. To simplify the figures in this paper, no data is included for comparison. However, some data concerning optical constants in these studies deviate somewhat from those measured in this

investigation. In particular, no second-order phonon vibration mode is observed, unlike that in the literature [20].

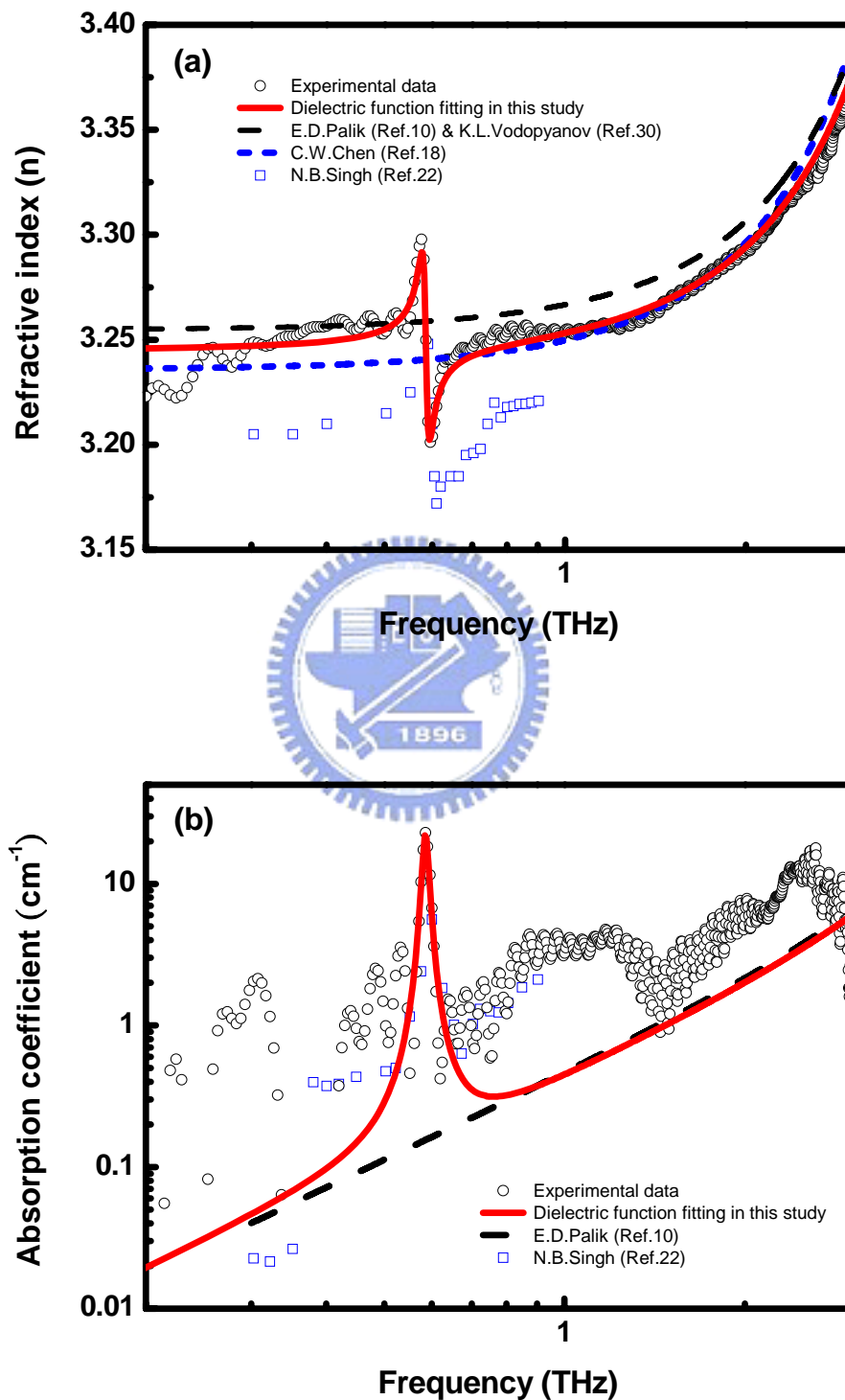


**Fig. 3-7** (a) Comparisons of refractive indices  $n$  herein and published values. Revised dielectric function-fitted curve is included. (b) Comparison of absorption

*coefficient  $\alpha$  herein with published values. Revised dielectric function-fitted curve is also included.*

The ordinary dielectric function over the terahertz range is modified herein. Furthermore, we fit our previous work [18] in Fig. 3-8 to retrieve the extraordinary dielectric function. The complex extraordinary dielectric function  $\varepsilon_e(\omega)$  is expressed as

$$\varepsilon_e(\omega) = A'\omega^6 + B'\omega^4 + C'\omega^2 + S_3 + \frac{(\omega_L^2 - \omega_T^2)S_3}{\omega_T^2 - \omega^2 - i\Gamma_3\omega} \quad (7)$$

where  $A'=122.3 \times 10^{-27} \text{ cm}^6$ ,  $B'=-22.88 \times 10^{-18} \text{ cm}^4$ ,  $C'=3.879 \times 10^{-9} \text{ cm}^2$ ,  $S_3=5.76$ ,  $\Gamma_3=2.8 \text{ cm}^{-1}$ ,  $\omega_L=245.5 \text{ cm}^{-1}$ ,  $\omega_T=237 \text{ cm}^{-1}$ . The extraordinary dielectric function may be adaptable to the terahertz regime by fitting the phase matching curve plotted in other works, which is shown in the inset of Figs. 3-8(a) and (b) [21, 23, 32]. In the inset of Figs. 3-8(a) and (b), there are some deviations in the long wavelength ranges. It might be likely due to the bandwidth of the two interaction waves in the difference frequency mixing process. On the other hand, the little changes of the phase matching angles among these THz range lead to the non-distinguishable recording of the angles value. Consequently, Table 3-1 concludes the parameters used in the calculation of the optical constants for  $\varepsilon$ -GaSe from Eq. [6] and [7].

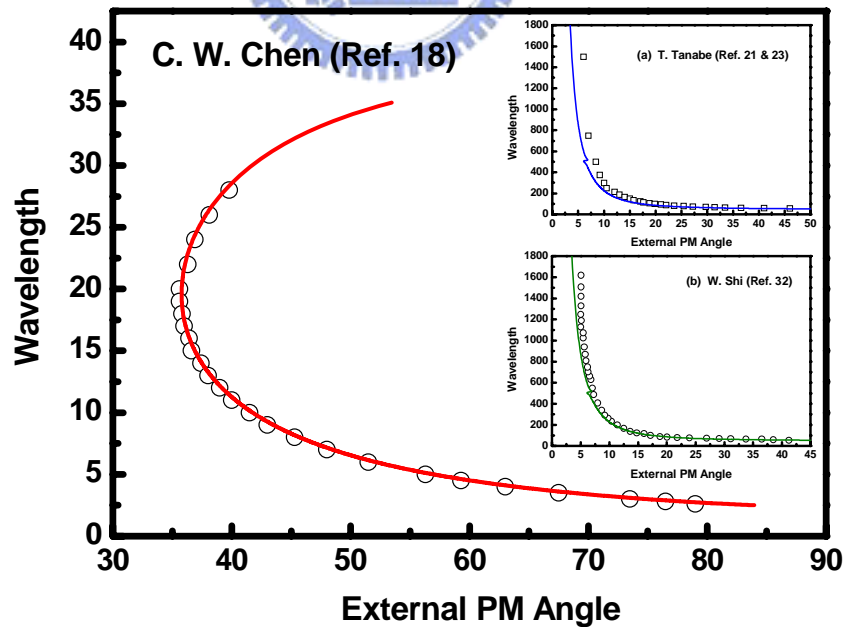


*Fig.3-8 Fitting of the infrared generation phase matching curve [18] to obtain the extraordinary refractive indices  $n_e$ . Inset: fitting the THz generation phase matching curve plotted in other works [21, 23, 32].*

**Table 3-1 Parameters used in the calculation of the dielectric functions for  $\epsilon$ -GaSe from Eq. [6] and Eq. [7]**

| <b>DIELECTRIC FUNCTION</b> | <b>PARAMETER</b>                       | <b>THIS WORK</b>               | <b>HANDBOOK REF.[10]</b>       |
|----------------------------|--|--------------------------------|--------------------------------|
| <b>Ordinary</b>            | <b>A (cm<sup>6</sup>)</b>              | <b>6.105×10<sup>-27</sup></b>  | <b>6.105×10<sup>-27</sup></b>  |
|                            | <b>B (cm<sup>4</sup>)</b>              | <b>1.8564×10<sup>-18</sup></b> | <b>1.8564×10<sup>-18</sup></b> |
|                            | <b>C (cm<sup>2</sup>)</b>              | <b>4.0499×10<sup>-9</sup></b>  | <b>4.0499×10<sup>-9</sup></b>  |
|                            | <b>S<sub>1</sub></b>                   | <b>7.37</b>                    | <b>7.443</b>                   |
|                            | <b>S<sub>2</sub></b>                   | <b>0.017</b>                   |                                |
|                            | <b>Γ<sub>1</sub> (cm<sup>-1</sup>)</b> | <b>2.8</b>                     | <b>3</b>                       |
|                            | <b>Γ<sub>2</sub> (cm<sup>-1</sup>)</b> | <b>0.5667</b>                  |                                |
|                            | <b>ω<sub>L</sub> (cm<sup>-1</sup>)</b> | <b>255</b>                     | <b>254.7</b>                   |
|                            | <b>ω<sub>T</sub> (cm<sup>-1</sup>)</b> | <b>213.5</b>                   | <b>213.5</b>                   |
|                            | <b>ω<sub>t</sub> (cm<sup>-1</sup>)</b> | <b>19.53</b>                   |                                |
| <b>Extraordinary</b>       | <b>A' (cm<sup>6</sup>)</b>             | <b>122.3×10<sup>-27</sup></b>  |                                |
|                            | <b>B' (cm<sup>4</sup>)</b>             | <b>-22.88×10<sup>-18</sup></b> |                                |
|                            | <b>C' (cm<sup>2</sup>)</b>             | <b>3.879×10<sup>-9</sup></b>   |                                |
|                            | <b>S<sub>3</sub></b>                   | <b>5.76</b>                    | <b>5.76</b>                    |
|                            | <b>Γ<sub>3</sub> (cm<sup>-1</sup>)</b> | <b>2.8</b>                     | <b>2.8</b>                     |
|                            | <b>ω<sub>L</sub> (cm<sup>-1</sup>)</b> | <b>245.5</b>                   | <b>245.5</b>                   |
|                            | <b>ω<sub>T</sub> (cm<sup>-1</sup>)</b> | <b>237</b>                     | <b>237</b>                     |

### 3.4.6 Sellmeier equations determination

According to the revised dielectric function proposed above, we report the following modified Sellmeier equations for GaSe suitable for wide frequency range. For o-ray,

$$n_o^2 = A + \frac{B}{\lambda^2} + \frac{C}{\lambda^4} + \frac{D}{\lambda^6} + \frac{E\lambda^2}{\lambda^2 - F} + \frac{G\lambda^2}{\lambda^2 - H} \quad (8)$$

where  $\lambda$  is the wavelength in micrometers, and  $A=7.37$ ,  $B=0.405$ ,  $C=0.0186$ ,  $D=0.0061$ ,  $E=3.1436$ ,  $F=2193.8$ ,  $G=0.017$ ,  $H=262177.5577$ . The last term is added into this equation in

order to interpret the phonon modes ( $\omega_i=19.53 \text{ cm}^{-1}$ ) observed in the THz range. Similarly, the modified Sellmeier equation for e-ray is also given by

$$n_e^2 = A' + \frac{B'}{\lambda^2} + \frac{C'}{\lambda^4} + \frac{D'}{\lambda^6} + \frac{E'\lambda^2}{\lambda^2 - F'} \quad (9)$$

with  $A' \approx 5.76$ ,  $B' \approx 0.3879$ ,  $C' \approx -0.2288$ ,  $D' \approx 0.1223$ ,  $E' \approx 0.4206$ , and  $F' \approx 1780.3$ . Figure 3-9 presents the extraordinary refractive indices in this work and comparison with that from other groups [10, 18, 30]. The inset of Fig. 3-9 shows the extraordinary refractive index  $n_e$  in wide THz range including the strong resonance region. Consequently, Table 3-2 lists the parameters used in the calculation of the optical constants for  $\epsilon$ -GaSe from Eq. [8] and [9].

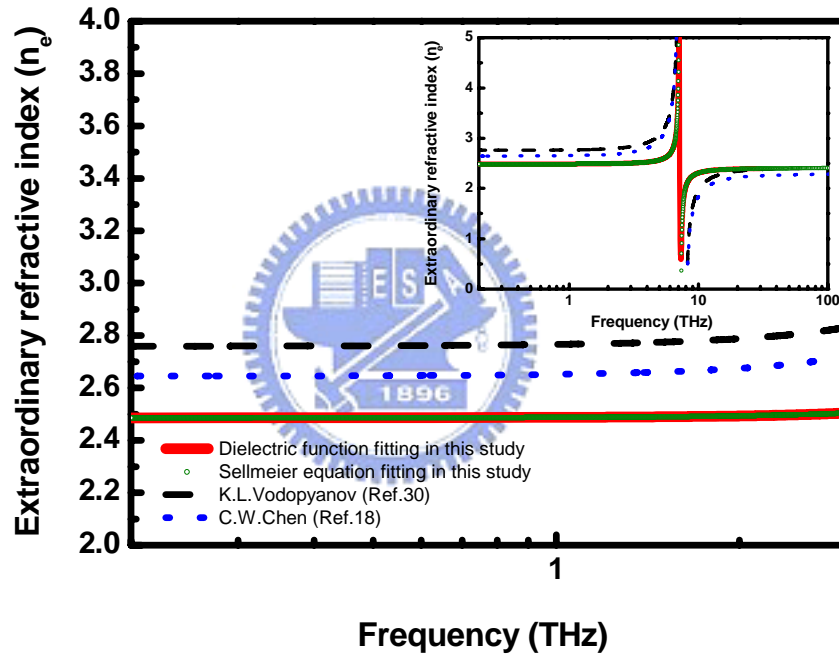


**Fig. 3-9** Comparisons of extraordinary refractive indices  $n_e$  herein and published values. Inset: the extraordinary refractive indices  $n_e$  in the wide frequency range 0.2–100THz.



**Table 3-2 Parameters used in the calculation of the Sellmeier equations for  $\epsilon$ -GaSe from Eq. [8] and Eq. [9]**

|                         | PARAMETER | THIS WORK   | VODOPYANOV<br>REF.[30] | ALLAKHVERDIEV<br>REF.[31] |
|-------------------------|-----------|-------------|------------------------|---------------------------|
| <b><math>n_o</math></b> | A         | 7.37        | 7.443                  | 7.38539                   |
|                         | B         | 0.405       | 0.405                  | 0.42611                   |
|                         | C         | 0.0186      | 0.0186                 | -0.00797                  |
|                         | D         | 0.0061      | 0.0061                 | 0.02291                   |
|                         | E         | 3.1436      | 3.1485                 | 0.88558                   |
|                         | F         | 2193.8      | 2194                   | 873.471                   |
|                         | G         | 0.017       |                        |                           |
|                         | H         | 262177.5577 |                        |                           |
| <b><math>n_e</math></b> | A'        | 5.76        | 5.76                   | 5.77169                   |
|                         | B'        | 0.3879      | 0.3879                 | 0.31285                   |
|                         | C'        | -0.2288     | -0.2288                | -0.03784                  |
|                         | D'        | 0.1223      | 0.1223                 | 0.0573                    |
|                         | E'        | 0.4206      | 1.855                  | 2216.135                  |
|                         | F'        | 1780.3      | 1780                   | 2049967                   |

### 3.4.7 Potential application of GaSe in terahertz frequencies

The GaSe crystal is a promising material for nonlinear optical and optoelectronic applications at terahertz frequencies. In Fig. 3-10, the figure of merit for GaSe is approximately five orders of magnitude larger than that for bulk LiNbO<sub>3</sub> at terahertz frequencies. Hence, GaSe crystal is a good candidate for generating terahertz waves. Not only does it have a low absorption coefficient at terahertz frequencies, but also it has a large birefringence, as shown in the inset of Fig. 3-10. The birefringence presented in this study is obtained from our revised ordinary and extraordinary dielectric function. The high birefringence and low absorption coefficient suffice for terahertz device applications. For example, the EO phase modulator can provide a phase shift  $\Phi=2\pi d\Delta n/\lambda$ , where  $d$  is the thickness of the EO crystal;  $\lambda$  is the operating wavelengths of the device;  $\Delta n$  equals the difference between  $n_e$  and  $n_o$  for the GaSe crystal ( $\Delta n= n_o-n_e$ ).

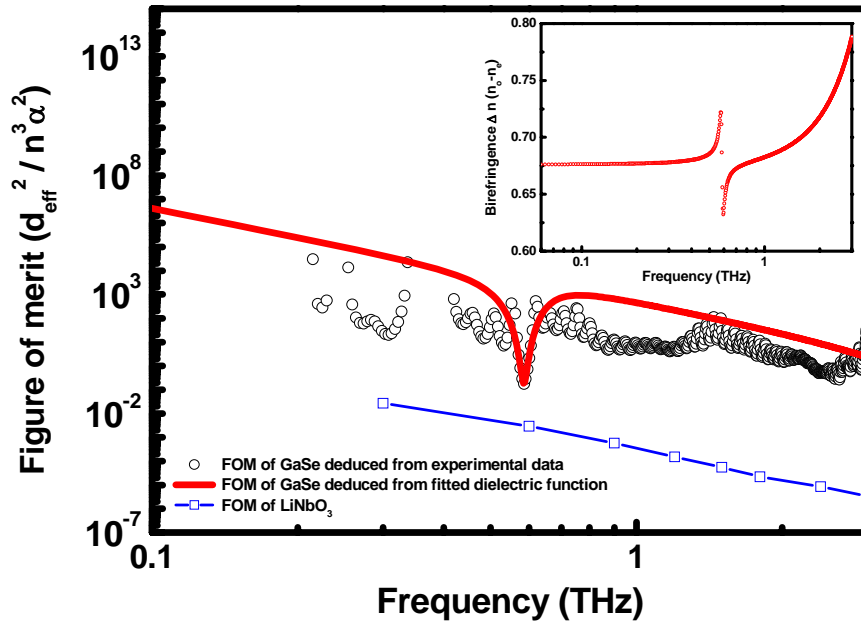


*Fig. 3-10 Comparison of figures of merit (FOM) of GaSe and LiNbO<sub>3</sub> crystals in terahertz range. Inset: birefringence of GaSe crystal at terahertz frequencies.*

A THz phase modulator design is considered. For a 1 THz frequency ( $\lambda=300 \mu\text{m}$ ), a crystal thickness  $d=400 \mu\text{m}$  is required for a  $2\pi$  phase shift. The estimated absorption coefficient  $\alpha$  is around  $2 \text{ cm}^{-1}$  at 1 THz. Disregards of the Fresnel reflection from the interfaces, the low intrinsic absorption loss in the GaSe crystal is such that the high transmittance could be as high as 92% for a crystal thickness of  $400 \mu\text{m}$ . Moreover, given a  $3\text{dB}$  loss at 1 THz, the GaSe crystal could be as thick as 3.4 mm if perfectly crystalline following high-quality crystal growth. Other practical applications of the design of photonic devices at terahertz frequencies are anticipated.

### 3.5 Summary

The optical constants of a single crystal  $\epsilon$ -GaSe are studied using the terahertz time-domain spectroscopy over the frequency range from 0.2 to 3 THz. Fitting the power reflectance over a wide terahertz range for ordinary refraction index yields the transverse and longitudinal optical phonons in the reststrahlen band of 6.39 and 7.62 THz, respectively.

Modified complex ordinary and extraordinary dielectric functions of GaSe are presented. Moreover, the revised Sellmeier equations are also reported herein. The accurate measurement of the optical properties of the  $\epsilon$ -GaSe crystal is useful for fundamental and practical applications, and the design of the photonic devices at terahertz frequencies. An estimated EO phase modulator design is developed to yield the promising characteristics of the GaSe crystal at terahertz frequencies.



## References

- [1] M. C. Nuss and J. Orenstein, "Terahertz Time-Domain Spectroscopy," in *Millimeter and Submillimeter Wave Spectroscopy of Solids*, G. Gruner, ed., (Springer, Berlin, 1998).
- [2] D. Mittleman, *Sensing with Terahertz Radiation* (Springer-Verlag, Berlin, 2003).
- [3] B. Ferguson and X. -C. Zhang, "Materials for terahertz science and technology," *Nat. Mater.* **1**, 26-33 (2002).
- [4] K. Reimann, R. P. Smith, A. M. Weiner, T. Elsaesser, and M. Woerner, "Direct field-resolved detection of terahertz transients with amplitudes of megavolts per centimeter," *Opt. Lett.* **28**, 471-473 (2003).
- [5] F. Blanchard, L. Razzari, H. -C. Bandulet, G. Sharma, R. Morandotti, J. -C. Kieffer, T. Ozaki, M. Reid, H. F. Tiedje, H. K. Haugen, and F. A. Hegmann, "Generation of 1.5  $\mu$ J single-cycle terahertz pulses by optical rectification from a large aperture ZnTe crystal," *Opt. Express* **15**, 13212-13220 (2007).
- [6] K. Kawase, M. Sato, T. Taniuchi, and H. Ito, "Coherent tunable terahertz wave generation from LiNbO<sub>3</sub> with monolithic grating coupler," *Appl. Phys. Lett.* **68**, 2483-2485 (1996).
- [7] W. Shi and Y. J. Ding, "A monochromatic and high-power terahertz source tunable in the ranges of 2.7-38.4 and 58.2-3540  $\mu$ m for variety of potential applications," *Appl. Phys. Lett.* **84**, 1635-1637 (2004).
- [8] W. Shi and Y. J. Ding, "Continuously-tunable and coherent terahertz radiation by means of phase-matched difference-frequency generation in zinc germanium phosphide," *Appl. Phys. Lett.* **83**, 848-850 (2003).
- [9] W. Shi and Y. J. Ding, "Tunable terahertz waves generated by mixing two copropagating infrared beams in GaP," *Opt. Lett.* **30**, 1030-1032 (2005).
- [10] E. D. Palik, *Handbook of Optical Constants of Solids* (Academic, New York, 1998), Vol. III.
- [11] V. G. Dmitriev, G. G. Gurzadyan, and D. N. Nikogosyan, *Handbook of Nonlinear Optical Crystals* (Springer, Berlin, 1997), pp. 166-169.
- [12] R. Huber, A. Brodschelm, F. Tauser, and A. Leitenstorfer, "Generation and field-resolved detection of femtosecond electromagnetic pulses tunable up to 41 THz," *Appl. Phys. Lett.* **76**, 3191-3193 (2000).
- [13] K. Liu, J. Xu, and X. C. Zhang, "GaSe crystals for broadband terahertz wave detection," *Appl. Phys. Lett.* **85**, 863-865 (2004).

- [14] S. Adachi and Y. Shindo, "Optical constants of  $\epsilon$ -GaSe," J. Appl. Phys. **71**, 428-431 (1992).
- [15] N. Piccioli, R. Le Toullec, M. Mejatty, and M. Balkanski, "Refractive index of GaSe between 0.45  $\mu\text{m}$  and 330  $\mu\text{m}$ ," Appl. Opt. **16**, 1236-1238 (1976).
- [16] V. M. Burlakov, E. A. Vinogradov, G. N. Zhizhin, N. N. Mel'nik, D. A. Rzaev, and V. A. Yakovlev, "Optical properties of GaSe films at lattice vibration frequencies," Sov. Phys. Solid State **21**, 1477-1480 (1979).
- [17] K. Allakhverdiev, N. Fernelius, F. Gashimzade, J. Goldstein, E. Salaev, and Z. Salaeva, "Anisotropy of optical absorption in GaSe studied by midinfrared spectroscopy," J. Appl. Phys. **93**, 3336-3339 (2003).
- [18] C. -W. Chen, Y. -K. Hsu, J. Y. Huang, C. -S. Chang, J. Y. Zhang, and C. -L. Pan, "Generation properties of coherent infrared radiation in the optical absorption region of GaSe crystal," Opt. Express **14**, 10636-10644 (2006).
- [19] Y. -K. Hsu, C. -W. Chen, J. Y. Huang, C. -L. Pan, J. -Y. Zhang, and C. -S. Chang, "Erbium doped GaSe crystal for mid-IR applications," Opt. Express **14**, 5484-5491 (2006).
- [20] B. L. Yu, F. Zeng, V. Kartazayev, R. R. Alfano, and K. C. Mandal, "Terahertz studies of the dielectric response and second-order phonons in a GaSe crystal," Appl. Phys. Lett. **87**, 182104-1-3 (2005).
- [21] T. Tanabe, K. Suto, J. -i. Nishizawa, and T. Sasaki, "Characteristics of terahertz-wave generation from GaSe crystals," J. Phys. D: Appl. Phys. **37**, 155-158 (2004).
- [22] N. B. Singh, T. B. Norris, T. Buma, R. N. Singh, M. Gottlieb, D. Suhre, and J. J. Hawkins, "Properties of nonlinear optical crystals in the terahertz wavelength region," Opt. Engineering **45**, 094002-1-7 (2006).
- [23] J. -i. Nishizawa, T. Sasaki, Y. Oyama, T. Tanabe, "Aspects of point defects in coherent terahertz-wave spectroscopy," Physica B **401-402**, 677-681 (2007).
- [24] K. Allakhverdiev, T. Baykara, S. Ellialtioglu, F. Hashimzade, D. Huseinova, K. Kawamura, A. A. Kaya, A. M. Kulibekov (Gulubayov), and S. Onari, "Lattice vibrations of pure and doped GaSe," Mater Res. Bull. **41**, 751-763 (2006).
- [25] C. L. Pan, C. F. Hsieh, R. P. Pan, M. Tanaka, F. Miyamaru, M. Tani, and M. Hangyo, "Control of enhanced THz transmission through metallic hole arrays using nematic liquid crystal," Opt. Express **13**, 3921-3930 (2005).
- [26] B. E. A. Saleh and M. C. Teich, *Fundamentals of Photonics* (Wiley, New York, 1991).

- [27] H. Yoshida, S. Nakashima, and A. Mitsuishi, "Phonon Raman Spectra of Layer Compound GaSe," *Phys. Status Solidi B* **59**, 655-666 (1973).
- [28] M. Hayek, O. Brafman, and R. M. A. Lieth, "Splitting and Coupling of Lattice Modes in the Layer Compounds GaSe, GaS, and  $\text{GaSe}_x\text{S}_{1-x}$ ," *Phys. Rev. B* **8**, 2772-2779 (1973).
- [29] K. Yamamoto, A. Masui, and H. Ishida, "Kramers-Kronig analysis of infrared reflection spectra with perpendicular polarization," *Appl. Opt.* **33**, 6285-6293 (1994).
- [30] K. L. Vodopyanov and L. A. Kulevskii, "New dispersion relationships for GaSe in the 0.65-18  $\mu\text{m}$  spectral region," *Opt. Commun.* **118**, 375-378 (1995).
- [31] K. R. Allakhverdiev, T. Baykara, A. K. Gulubayov, A. A. Kaya, J. Goldstein, N. Fernelius, S. Hanna, and Z. Salaeva, "Corrected infrared Sellmeier coefficients for gallium selenide," *J. Appl. Phys.* **98**, 093515-1-6 (2005).
- [32] W. Shi, Y. J. Ding, N. Fernelius, K. Vodopyanov, "Efficient, tunable, and coherent 0.18–5.27-THz source based on GaSe crystal," *Opt. Lett.* **27**, 1454-1456 (2002).



## Chapter 4

# Generation properties of coherent infrared radiation in the optical absorption region of GaSe crystal

### 4.1 Introduction

Generation of broadly tunable coherent mid-infrared (mid-IR) pulses is of considerable interests in many disciplines ranging from molecular spectroscopy, bio-medical diagnostics, to remote sensing of atmospheric trace constituents. The most important technique to generate tunable coherent radiation in the mid infrared (mid-IR) is based on the second-order nonlinear optical (NLO) processes in a non-centrosymmetric crystal. These NLO processes include difference-frequency mixing, optical parametric generation and amplification [1-9].

The crystals used for mid-IR generation by frequency down conversion are still scarce and only a few of them have become commercially available [1-3]. Among these, GaSe is particularly attractive as it exhibits a fairly high effective nonlinear coefficient,  $d_{eff}=54$  pm/V at  $10.6 \mu\text{m}$  and a wide transparency range from  $0.62 \mu\text{m}$  to  $20 \mu\text{m}$  [10]. It has been successfully employed for generation of coherent radiation in the mid-IR and even down to the THz frequency range by difference-frequency generation (DFG) or phase-matched optical rectification [5, 8]. Improvements in the optical nonlinearity of GaSe crystal with doping of silver or sulphur have been reported [11-13]. Recently, we also reported that the nonlinear coefficient ( $d_{eff}$ ) of a GaSe crystal doped with 0.5 atom % erbium is 24% higher than that of a pure GaSe crystal [14].

GaSe is a semiconductor with layered hexagonal structure belonging to the  $D_{3h}^1(P\bar{6}m2)$  space group. Beyond mid-IR, the infrared absorption edge of the NLO crystal places a practical limit on its frequency down conversion range. The infrared absorption edge of a crystal is usually attributed to infrared-active phonon modes or their combination modes. Unfortunately, there have been very limited studies concerning the effect of infrared absorption edge on the optical dispersion and frequency down conversion efficiency of NLO crystals, GaSe in particular.

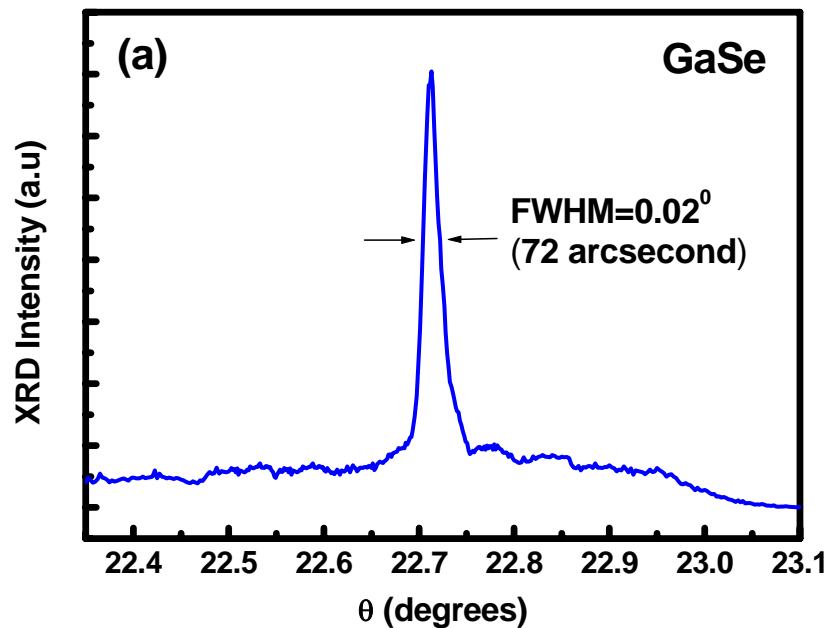
In this work, we investigate the effect of infrared absorption on the generation properties of coherent infrared radiation from mid-IR to THz region using the GaSe crystal.



Based upon the experimentally determined phase matching curves, modified Sellmeier equations of GaSe are proposed to more accurately describe the optical dispersion of this crystal in this spectral region. We identify the phonon modes that are responsible for the resulting infrared absorption edge. We also show that the absorption effect of these infrared active phonon modes can be reduced by doping GaSe crystal with erbium ions. The scheme increases the IR output and therefore extends the long wavelength tuning limit.

## 4.2 Experimental methods

The GaSe crystals used in this study were grown with the Bridgman method. For doped crystals or Er:GaSe, up to 0.2 atom % of erbium (99.95%) was introduced into the melt. Raw materials were placed in a well-cleaned quartz tube, sealed and then pumped down to below  $10^{-6}$  Torr. The crystal growth was carried out under a thermal gradient of 30 °C/cm with a growth rate of 2 cm/day. The resulting pure GaSe and Er:GaSe crystals exhibit the characteristic appearance of hexagonal layered structure of (001) plane. The crystal qualities were evaluated by measuring the X-ray rocking curve of the diffraction peak from the (008) plane. The optical transmission of the crystals were determined with a Fourier-transform infrared spectrometer (FTIR, Bruker IFS66v/S) in the mid-IR region and a home-made THz time-domain spectrometer (THz-TDS) [15] in the THz region, respectively.



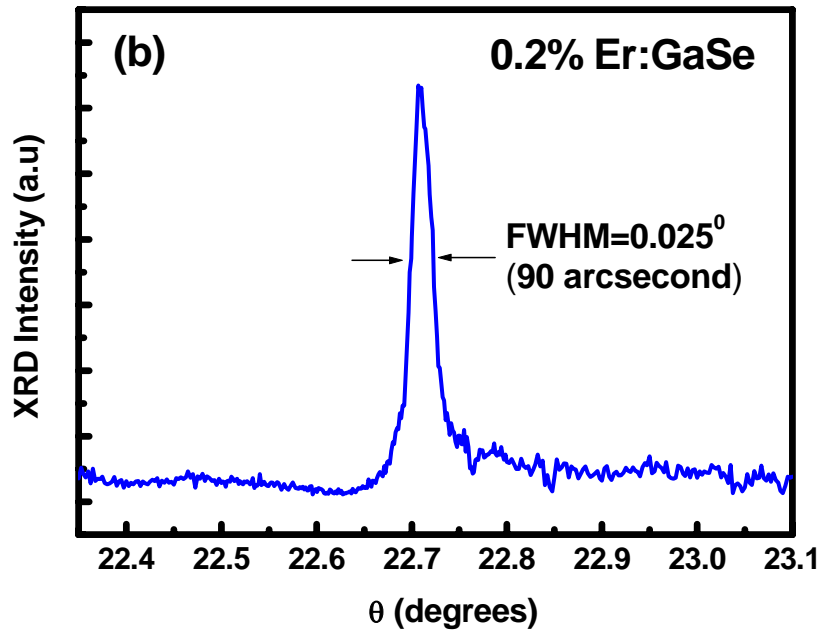
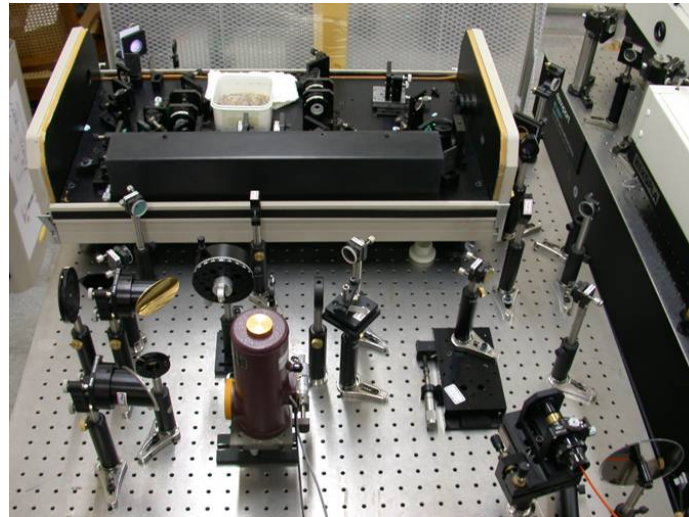


*Fig. 4-1 (a) X-ray rocking curve of pure GaSe (b) X-ray rocking curve of 0.2% Er:GaSe.*

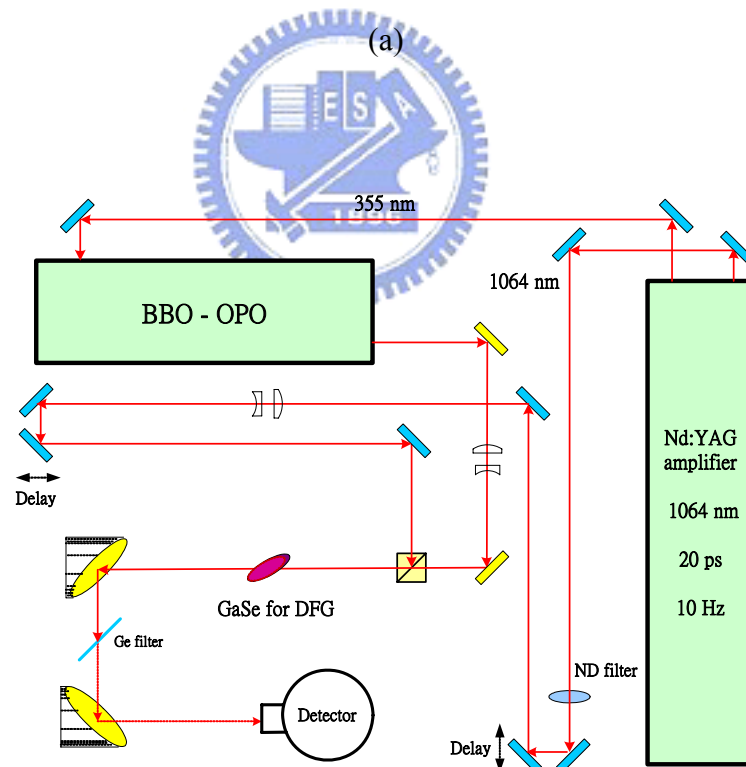
The crystal quality of the pure and the 0.2% Er:GaSe crystals are excellent. This is confirmed by measuring full-width-at-half-maximum (FWHM) widths of the (008) diffraction peaks, estimated to be about  $0.02^\circ$  and  $0.025^\circ$  for the pure and the 0.2% Er:GaSe crystals. Figures 4-1(a) and (b) present the X-ray rocking curves for both as-grown and doped GaSe crystals, respectively.

The GaSe difference-frequency generator (DFG) was implemented with a collinear type-I ( $o+o \rightarrow e$ ) phase-matching geometry. The photography and schematic of this DFG system are shown in Figs. 4-2 (a) and (b), respectively. The pump beam of the DFG was provided by the fundamental output of an Nd: YAG laser ( $\lambda=1.064 \mu\text{m}$ ) with pulse duration of 20 ps, at a repetition rate of 10 Hz. The signal beam, with a pulse duration of 5 ps and tunable in the range of 1.1-1.8  $\mu\text{m}$  was generated by the idler output of a  $\beta\text{-BaB}_2\text{O}_4$  (BBO)-based optical parametric amplifier (OPA) pumped by the 355 nm output of the Nd:YAG laser, which is shown in Fig. 4-3. The typical pulse energy of the 1.064  $\mu\text{m}$  beam employed for DFG was about 750  $\mu\text{J}$ , while that of the OPA was adjusted between 35 and 50  $\mu\text{J}$ . The spot size of the pump beam was measured to be about 1.7 mm, corresponding to a maximum peak intensity of 1.7  $\text{GW}/\text{cm}^2$  on the GaSe crystal. The spot size of the signal beam after focusing is about 2.5 mm. In order to prevent optically induced damage, the

samples are placed at the location of the focus of signal beam, which is before the focus of the pump beam. Both GaSe and the Er:GaSe crystals used in this study were not anti-reflection-coated and have a nominal thickness of 3.3 mm.



(a)



(b)

**Fig. 4-2** (a) *Photography of the GaSe-based ps-DFG system.* (b) *Schematic of the GaSe-based ps-DFG system.*

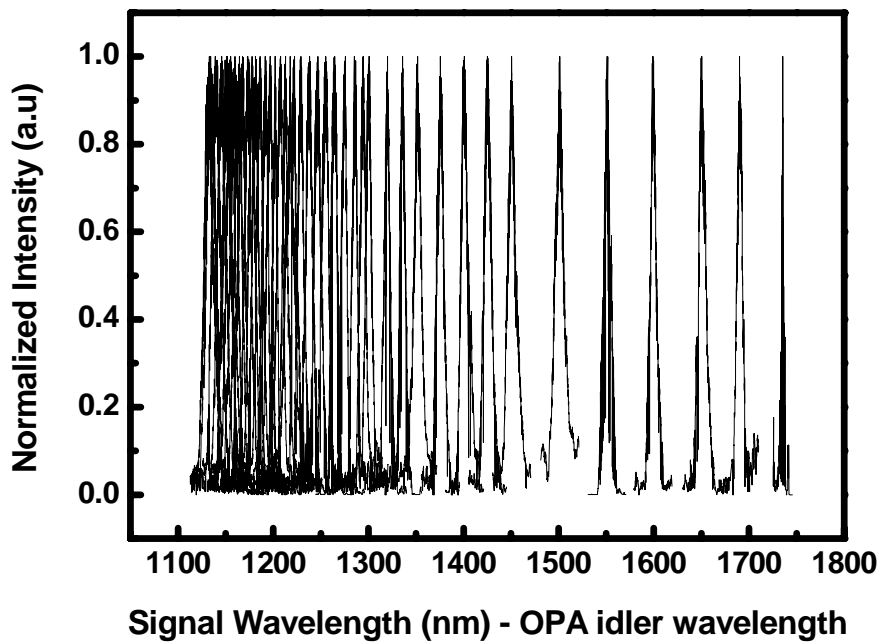


*Fig. 4-3 Wide tuning range of idler output from 355nm pumped OPA.*

The generated mid-IR radiation was detected either with a cryogenically cooled mercury cadmium telluride (MCT) detector or a silicon bolometer. The residual pump radiation was blocked with a germanium (Ge) filter. The absolute pulse energies of the generated mid-IR radiation were determined with a calibrated pyroelectric detector. The generated pulse energies are corrected for the losses from Fresnel reflection and transmittance of the Ge filter.

## **4.3 Results and Discussions**

### **4.3.1 Optical properties of pure and erbium doped GaSe crystals measured by transmitted type FTIR**

The absorption power spectrum of the pure GaSe crystal from 5 to 40  $\mu\text{m}$  is presented in Fig. 4-4. A strong infrared absorption peak near 40–50  $\mu\text{m}$  ( $200\text{--}250\text{ cm}^{-1}$ ) can be clearly observed. Summarizing the lattice vibrational analysis and the existing data for infrared active phonons of  $\epsilon\text{-GaSe}$  [16], several longitudinal and transverse optical phonons modes

were noticed to occur at  $214\text{ cm}^{-1}$  ( $E'(TO)$ ) and  $255\text{ cm}^{-1}$  ( $E'(LO)$ ). Before the absorption edge, some other IR-active modes at  $19.6\text{ }\mu\text{m}$  ( $510\text{ cm}^{-1}$ ),  $22.4\text{ }\mu\text{m}$  ( $446\text{ cm}^{-1}$ ),  $24.4\text{ }\mu\text{m}$  ( $410\text{ cm}^{-1}$ ),  $27.6\text{ }\mu\text{m}$  ( $362\text{ cm}^{-1}$ ),  $30.4\text{ }\mu\text{m}$  ( $329\text{ cm}^{-1}$ ), and  $33.1\text{ }\mu\text{m}$  ( $302\text{ cm}^{-1}$ ) can also be identified. These modes are assigned as the difference-frequency combinations of acoustic and optical phonons or the impurity-induced localized modes. For example, the band at  $24.4\text{ }\mu\text{m}$  is the overtone of the IR active mode at  $46.7\text{ }\mu\text{m}$ . The band at  $27.6\text{ }\mu\text{m}$  has its origin from the multi-phonon processes, while the two bands at  $19.6\text{ }\mu\text{m}$  and  $22.4\text{ }\mu\text{m}$  are mainly due to the impurity-induced localized modes [17-20].

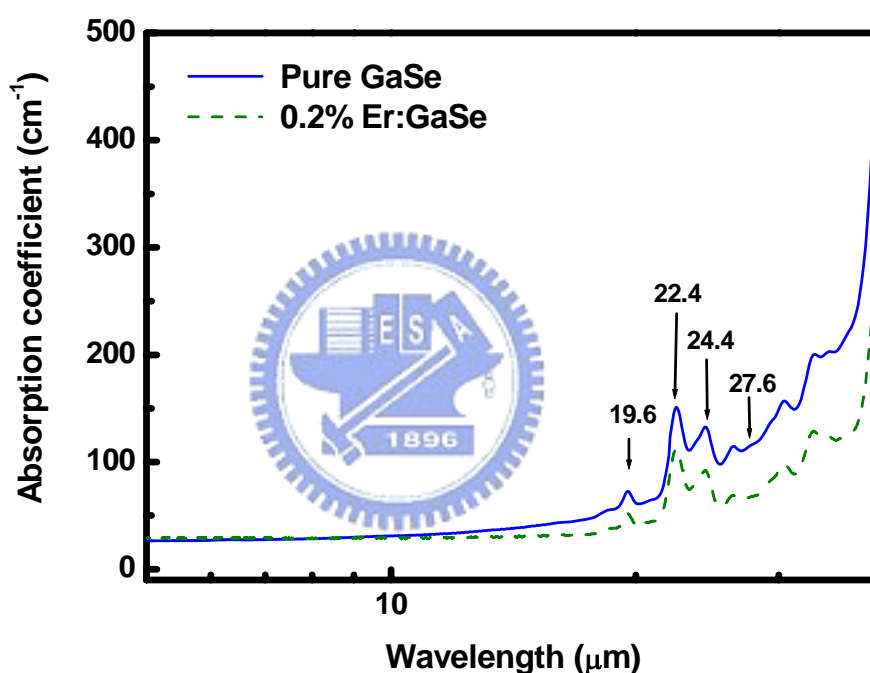


*Fig. 4-4 Absorption coefficients of GaSe are plotted as a function of wavelength in the mid-IR. The solid and dashed curves show our experimental results measured by FTIR and for pure and  $Er^{3+}$ :GaSe, respectively.*

From our measurement, the transmittance of the erbium doped GaSe crystal was compared highly with the one of pure crystal while the output wavelength was above  $15\text{ }\mu\text{m}$ . The infrared absorption of  $Er^{3+}$ :GaSe is lower than that of pure crystal because the linear chain structure of Se-Ga-Ga-Se-Se-Ga-Ga-Se [14] in pure GaSe crystal is disrupted by erbium dopants. As a result, the vibrations of induced vacancies or substitutional impurities

in GaSe crystal are shifted to lower frequencies. Consequently, the heights of overtone absorption peaks from the unperturbed part of GaSe lattice are reduced.

### 4.3.2 Effective nonlinear coefficient ( $d_{eff}$ ) determined by SHG

The most commonly used method to determine the effective nonlinear coefficient is second-harmonic generation (SHG), because SHG benefits from well-established focused beam theories for type-I and type-II interactions. Subsequently, we utilized the picosecond infrared light source generated from our DFG system as a pump beam to achieve the frequency doubling in the as-grown pure GaSe crystal. The DFG system herein, shown in Fig. 4-2(b), was tuned to the wavelength of 6  $\mu\text{m}$ . The output of the DFG system had a pulse width of 5 ps, and the pulse energy was available up to  $\sim 1$   $\mu\text{J}$ . We determined optimum condition by varying the orientation and position of the crystal until maximum SHG output was observed. The pulse energy in both the fundamental and the frequency-doubled beams were measured with MCT detector. A 1 mm thick glass plate was introduced to separate the two wavelengths, and the absorption of the plate was factored into the efficiency calculation.

Type-I phase matching was used with an ordinary wave input and obtained an extraordinary wave output. The external phase matching angle of  $30.2^\circ$  was adjusted by means of dispersion relation of GaSe. As a function of the input pulse energy, the measured efficiencies of pure GaSe crystal are presented in Fig. 4-5. The slope of the efficiency data was also used to determine the effective nonlinear optical coefficient ( $d_{eff}$ ) for this crystal. The extracted effective nonlinear coefficient  $K$ , using the focused Gaussian beam theory of *Boyd* and *Kleinman*, combined with both focusing and double refraction effects can be determined [21]. The theoretical second-harmonic power  $P_2$  is related to  $K$  the following equation by

$$P_2 = KP_1^2 L k_1 h(B, \xi) \quad (1)$$

where  $P_1$  is the fundamental input power;  $L$  is the interaction length;  $k_1 = 2\pi n / \lambda_0$ , with  $n$  being the index of refraction of the input beam; and  $h(B, \xi)$  is the *Boyd* and *Kleinman* efficiency factor. The double refraction parameter is  $B = (\rho / 2)(k_1 L)^{1/2}$ , where  $\rho$  is the walk-off angle of  $3.4^\circ$  was used, which is the predicted value when the Sellmeier equations are used at the predicted phase matching angle. The focusing parameter  $\xi = L / b$ , where  $b$  is the length for confocal configuration over which the beam diameter is less than  $2^{1/2} \omega_0$ . It is given by

$b = k_i \omega_0^2$ , and the efficiency scaling constant in *m.k.s.* units is

$$K = 8\pi d^2 / c \varepsilon_0 n^3 \lambda_0^2 \quad (2)$$

where  $\varepsilon_0$  is the permittivity of free space,  $c$  is the vacuum speed of light, and  $d$  is the effective nonlinear coefficient in meters per volt.

The measured nonlinear conversion efficiency is the total energy of second-harmonic signal compared with the fundamental pulse energy and is expressed as  $\eta = \int P_2 dt / \int P_1 dt$ , where the integrals are over the temporal duration of the pulse. One can relate this efficiency to the time-independent *Boyd* and *Kleinman* theory by measuring the fundamental pulse shape and integrating Eq. (1) over time. The result is

$$\eta = KLk_1 h(B, \xi) \int P_\lambda^2 dt / \int P_\lambda dt \quad (3)$$

So that by measuring the temporal pulse shape of the fundamental we can relate the experimental conversion efficiency to the theory. Using Eq. (1)-(3), along with the measured pulse shape, we calculated the  $d_{eff}$  by matching the theory to the data. We have determined the nonlinear coefficient  $d_{22}$  of the pure GaSe crystal to be 56 pm/V, which agrees well with a value of 54 pm/V reported in Ref. [10].

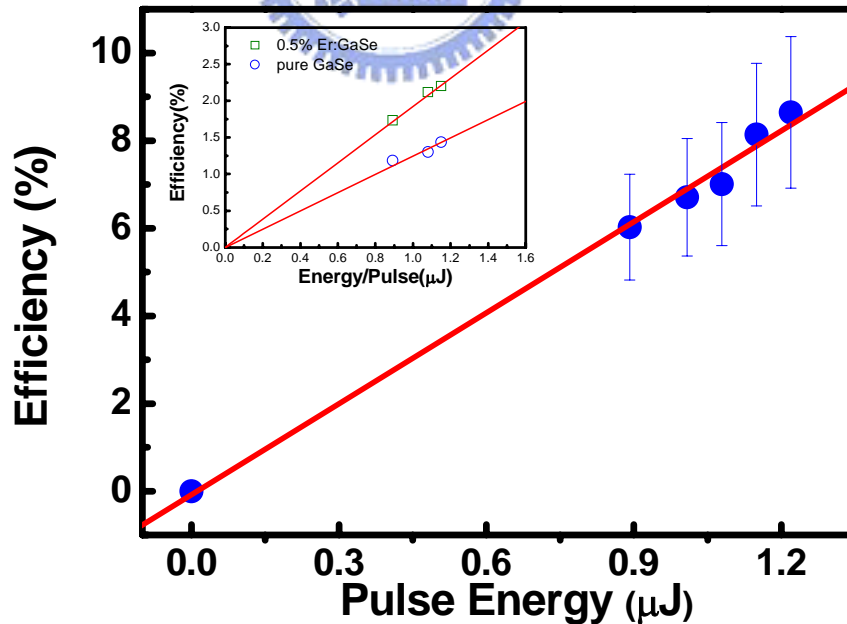


**Fig. 4-5** Measured SHG efficiency of a 3.3 mm long pure GaSe crystal as a function of the internal pulse energy. Inset: Comparison of  $d_{eff}$  between pure and 0.5% Er:GaSe.



In addition, the conversion efficiency for erbium doped GaSe crystal is also measured in this study. The effective nonlinear coefficient  $d_{eff}$  of the 0.5% Er:GaSe crystals were determined to be higher than that for pure one. The experimental measurement is shown in the inset of Fig. 4-5. The difference could be ascribed to either crystal quality [11] or doping-induced effect [12]. The structural analysis of our GaSe crystals shown in Fig. 4-1 suggests that these crystals have similar crystal quality. Therefore, the increased effective nonlinear coefficient of Er:GaSe must originate from the doping effect with erbium. A plausible interpretation could be that the substitution of one  $Er^{3+}$  ion for one pair of  $Ga^{2+}$  and insertion of one  $Er^{3+}$  interstitial ion at interlayer sites in the unit cell could result in a favorable local structural alteration with better optical nonlinearity. Note that an 20 % increase in optical nonlinearity by impurity substitution was also observed recently in  $YCa_4O(BO_3)_3$  crystal [22] doped with Yb at a fairly high doping level of 20%. The increase in optical nonlinearity was attributed to the more covalent nature of Yb, which causes large delocalization of the  $\pi$ -electrons in the BO conjugate ring. Based on these two experimental studies, doping indeed seems to be an effective way to improve the optical properties of nonlinear optical crystals. Effective nonlinear coefficient ( $d_{eff}$ ) of 0.5% erbium doped GaSe crystal was found to be increased by 24% from that of a pure GaSe crystal. It is noticed that the absorption coefficients of pure and erbium doped GaSe are comparable in the wavelength of 6  $\mu m$ , the result is shown in Fig. 4-4. The difference is within the 10% deviation, in which the value for erbium doped GaSe is slightly higher. Therefore, the absorption coefficient should not be likely the main origin which leads to the 24% difference of the  $d_{eff}$  for the doped and pure GaSe crystals.

### 4.3.3 Picosecond mid-infrared generation by difference frequency mixing

The tuning curve of a collinear type-I phase-matched GaSe DFG pumped at 1.064  $\mu m$  is presented in Fig. 4-6. The filled triangles in Fig. 4-6 are the experimental data. The broken lines in red and green are the calculated results by using the Sellmeier equations reported in Ref. [23] and Ref. [24], respectively. To characterize the phase matching (PM) curves, we prepare one sample for each type of GaSe crystals. We first carefully determine the crystal orientation with a zero external angle. The phase matching angles can be measured with an accuracy limited by the rotational stage used. The tuning curves are highly reproducible for different measurement runs with each data point having a

measurement accuracy of  $\pm 0.2^\circ$  in crystal orientation and 10 nm in wavelength. The difference between the phase matching tuning curves of the pure GaSe and the Er:GaSe (not shown here) can not be distinguished within the measurement accuracy. The Erbium doping appears to produce very small perturbation on the lattice of GaSe and therefore its role can not be revealed in the Sellmeier equations and PM curve.

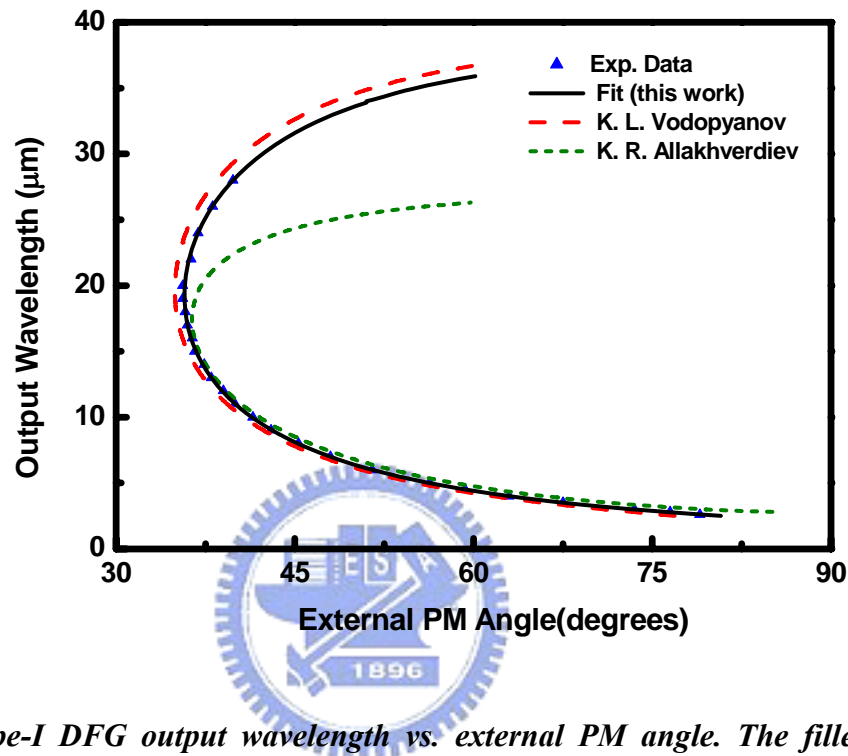


*Fig. 4-6 Type-I DFG output wavelength vs. external PM angle. The filled triangles show the experimental data and solid curve is the fitting curve using the modified Sellmeier equation. Dashed curve: calculated phase matching curve using dispersion of GaSe from Ref. [23]. Dotted curve: calculated phase matching curve using dispersion of GaSe from Ref. [24].*

#### 4.3.4 Sellmeier equations determination

The tuning curves shown in Fig. 4-6 indicate that by varying the external PM angle from  $34^\circ$  to  $80^\circ$ , the DFG output can be tuned from 2.4 to 28  $\mu\text{m}$ . For the output wavelengths longer than 20  $\mu\text{m}$ , however, the experimental PM angles show significant deviation from the two calculated phase matching curves. Compared to the curve with Sellmeier equations taken from Ref. [23], our measured data points deviate from the calculated curve by 2%–4% ( $0.7^\circ$ – $3.3^\circ$ ), which are larger than the error bar of our

experimental data. A uniform shift of the measured data along the x-axis, which results in a deviation of 0.6°–2.6°, can not yield a satisfactory fit to the PM curve from Ref. [23]. Furthermore the absolute crystal orientation with a zero external angle can be measured to rule out this possibility. Therefore, to fit the PM curve for DFG satisfactorily, we propose the following modified Sellmeier equations for GaSe.

For o-ray,

$$n_o^2 = A + \frac{B}{\lambda^2} + \frac{C}{\lambda^4} + \frac{D}{\lambda^6} + \frac{E\lambda^2}{\lambda^2 - F} \quad (4)$$

where  $\lambda$  is the wavelength in micrometers, and  $A=7.37$ ,  $B=0.405$ ,  $C=0.0186$ ,  $D=0.0061$ ,  $E=3.1436$ ,  $F=2193.8$ . Similarly, the modified Sellmeier equation for e-ray is also given by

$$n_e^2 = A' + \frac{B'}{\lambda^2} + \frac{C'}{\lambda^4} + \frac{D'}{\lambda^6} + \frac{E'\lambda^2}{\lambda^2 - F'} \quad (5)$$

with  $A' \simeq 5.76$ ,  $B' \simeq 0.3879$ ,  $C' \simeq -0.2288$ ,  $D' \simeq 0.1223$ ,  $E' \simeq 0.4206$ , and  $F' \simeq 1780.3$ . The modified Sellmeier equations are expected to be accurate in the spectral range of 2.4–35  $\mu\text{m}$  and had been experimentally verified from 2.4 to 28  $\mu\text{m}$ . It is noticed that the parameters published in Ref. [25] were our previous achievement. Those parameters were performed by genetic algorithm fitting which find the best solution in the global searching. After the following and completely work in this study, the parameters of the Sellmeier equations for GaSe crystal are modified again, which match appropriately for the physical meanings and crystal properties. These achievements have been mentioned and reported in chapter 3 in this thesis.

The phase matching curve based our modified Sellmeier equations is plotted in Fig. 4-6 as the solid curve. Excellent agreement with experimental data points is achieved. The error could be down to about  $2.4 \times 10^{-2}$ . The improvement of our fit with Eqs. (4) and (5) from that with Ref. [23] is statistically significant, implying that our modified Sellmeier equations can be used to yield useful information about the lattice vibrations responsible for the absorption edge. There have been very limited studies concerning the origin and effect of infrared absorption edge on the optical dispersion of a NLO crystal. The information reported is crucial in view that infrared absorption edge is an important parameter for the design of new infrared NLO crystals.

### 4.3.5 Relation between infrared absorption edge and optical dispersion

The space group for  $\epsilon$ -GaSe is  $D_{3h}^1(P\bar{6}m2)$ , and the primitive unit cell contains two layers or eight atoms. The symmetry of the pseudolattice is the same as that of the crystal, and the site group is  $C_{3v}(3m)$  for both Ga and Se. The decomposition into irreducible representation is

$$4A_2'' + 4A_1' + 4E' + 4E'' \quad (6)$$

The modes are characterized in Table 4-1. The Ga and Se atoms are in motion in all 24 normal modes. The  $E'$  modes are both infrared- and Raman-active, because of the lack of an inversion center in the  $\epsilon$  poly-type [26].

**Table 4-1 Properties of the long-wavelength lattice vibrations of  $\epsilon$ -GaSe**

| Irreducible representation | Number of acoustical modes | Number of optical modes | Activity       | Direction of vibration | Atoms involved | Transformation properties |
|----------------------------|----------------------------|-------------------------|----------------|------------------------|----------------|---------------------------|
| $A_2''$                    | 1                          | 3                       | Infrared       | <i>c</i> -axis         | Ga+Se          | <i>z</i>                  |
| $A_1'$                     |                            | 4                       | Raman          | <i>c</i> -axis         | Ga+Se          | $x^2+y^2, z^2$            |
| $E'$                       | 1                          | 3                       | Infrared+Raman | Basal plane            | Ga+Se          | $x, y; x^2-y^2, xy$       |
| $E''$                      |                            | 4                       | Raman          | Basal plane            | Ga+Se          | $yz, zx$                  |

The poles of the modified Sellmeier equations occur at 42.2  $\mu\text{m}$  for the e-ray and 46.8  $\mu\text{m}$  for the o-ray, respectively. The pole of the o-ray dispersion corresponds to an infrared active mode of  $E'$ -symmetry with vibration involving both Ga and Se atoms on the basal plane of GaSe crystal. The optical field of the o-ray propagating through the GaSe crystal thus experiences an index of refraction reflecting the intralayer covalent bonding structure of GaSe. The vibrational displacements of atoms in a primitive unit cell for  $E'$ -symmetry in the hexagonal GaSe are shown in Fig. 4-7. The pole of the e-ray dispersion corresponds to an infrared active mode of  $A_2''$ -symmetry with vibration involving both Ga and Se atoms along the optical axis (*c*-axis). The optical field of the e-ray then experiences an index of refraction, reflecting an optical dispersion from the interlayer vibration in the GaSe crystal [26]. The vibrational displacements of atoms in a primitive unit cell for  $A_2''$ -symmetry in the hexagonal GaSe are shown in Fig. 4-8.

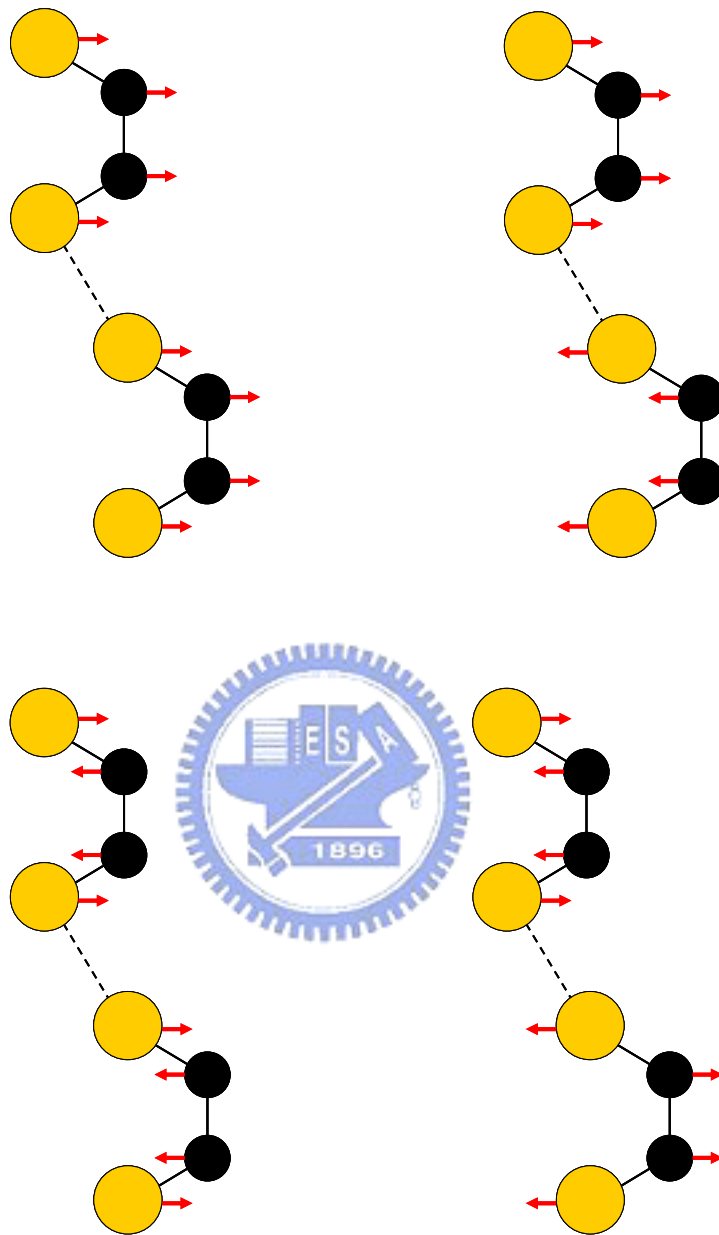


*Fig. 4-7 Vibrational displacements of atoms in a primitive unit cell for  $E'$ -symmetry in the hexagonal GaSe. The arrows indicate only directions of atomic displacements [26].*

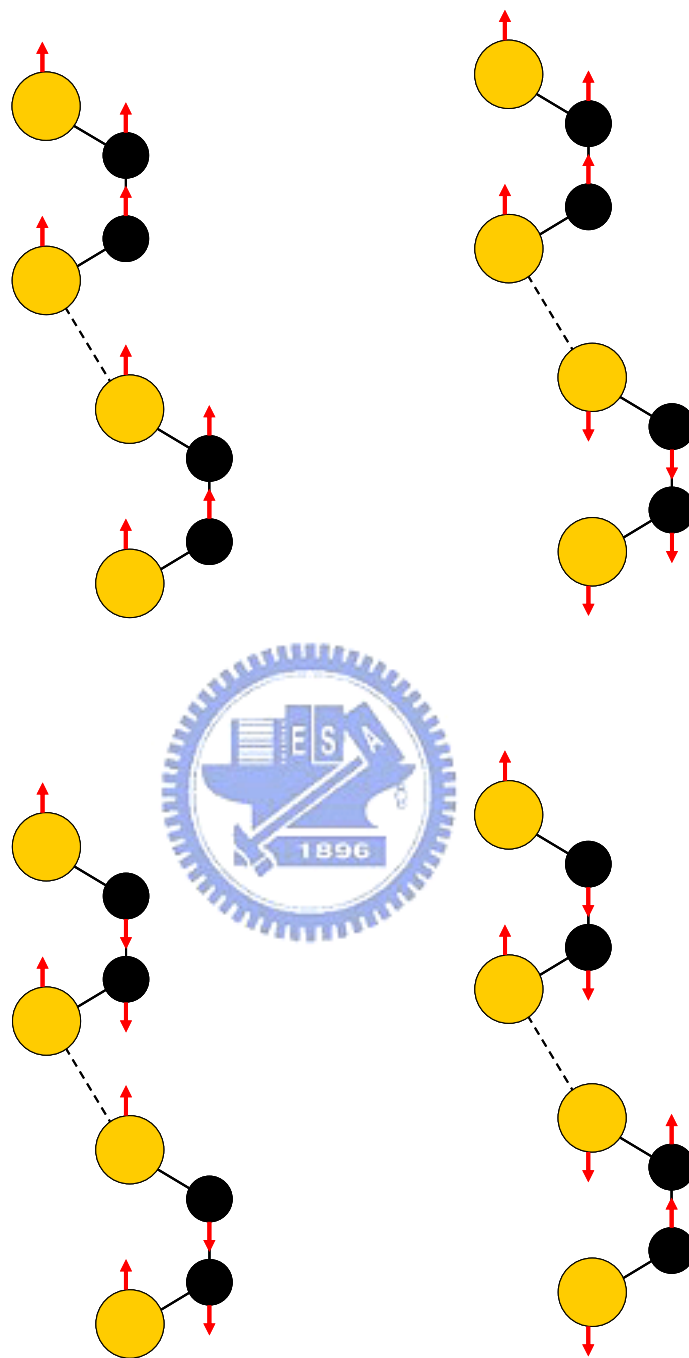


**Fig. 4-8** *Vibrational displacements of atoms in a primitive unit cell for  $A_2''$ -symmetry in the hexagonal GaSe. The arrows indicate only directions of atomic displacements [26].*

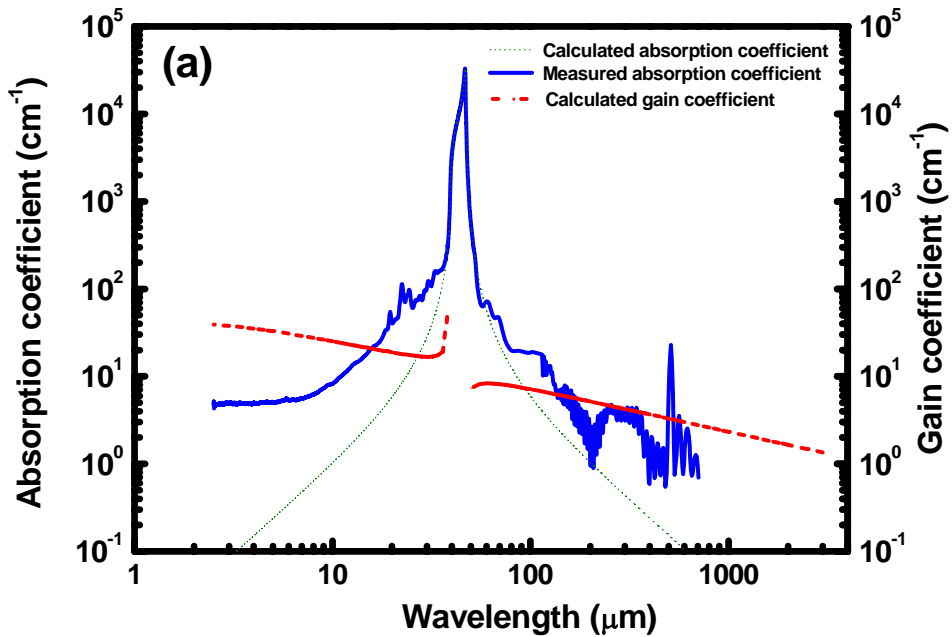
### 4.3.6 Parametric gain and output power calculation

The parametric gain can be written as [27]

$$\Gamma(\lambda) = \sqrt{\frac{8\pi^2 d_{eff}^2 I_p}{\varepsilon_0 c n_s n_i n_p \lambda_s \lambda_i}} \quad (7)$$

where  $I_p$  is the intensity of the pump beam;  $d_{eff}$  is the effective nonlinear coefficient;  $\varepsilon_0$  is the permittivity of free space;  $c$  is the light velocity in vacuum;  $n_p$ ,  $n_s$ ,  $n_i$  correspond to the indices of refraction at the pump, the seeding and the generated IR wavelengths;  $\lambda_s$  and  $\lambda_i$  correspond to the wavelengths of the seeding and the idler IR pulses, respectively.

The theoretical parametric gain and absorption coefficients of pure GaSe are plotted as a function of wavelength in Fig. 4-9(a). The output pulse energies of a 3.3 mm long pure GaSe DFG from 2.4–28  $\mu\text{m}$  are presented as solid squares in Fig. 4-9(b). The energy of the infrared pulses generated at 3.5  $\mu\text{m}$  was about  $\sim 13 \mu\text{J}$  with a photon conversion efficiency of 7.3%. This DFG system has stable output with  $\pm 8\%$  power fluctuation, which is due mainly to the fluctuation of the laser and is treated as the error bars in the measurement. With the exception of the absorption band around 40–50  $\mu\text{m}$ , the output pulse energy decreases monotonically with increasing wavelength. This is attributed to a decrease in parametric gain and an increase in linear absorption loss of GaSe crystal.





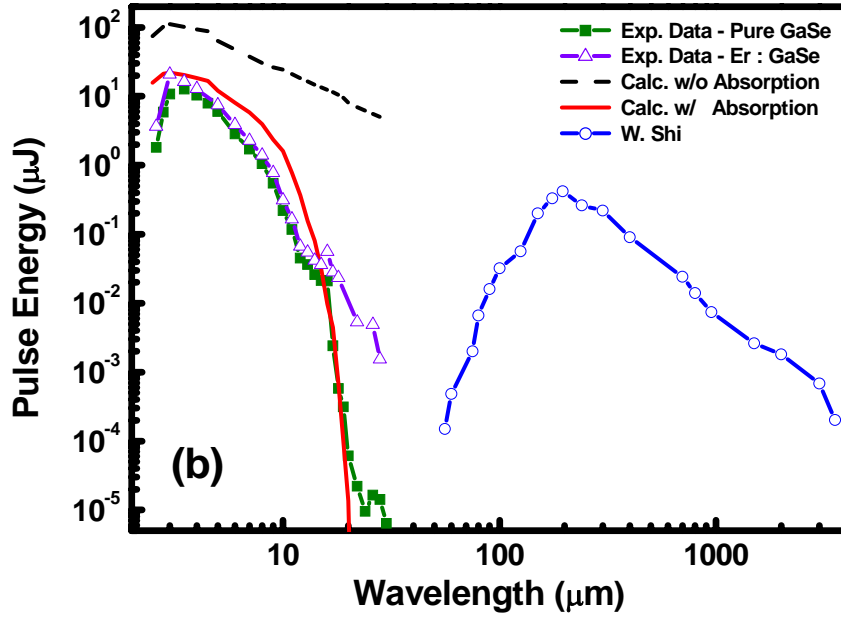


**Fig. 4-9** (a) Calculated parametric gain (dash curve), calculated infrared absorption (dot curve) and measured infrared absorption (solid curve) as a function of wavelength. (b) Measured and calculated pulse energies of the DFG generator versus wavelength. Solid squares show the measured infrared pulse energies for pure GaSe, open triangles show the measured infrared pulse energies for  $Er^{3+}$ :GaSe, solid curve and dashed curve indicate the calculated pulse energies with and without considering the crystal linear absorption coefficient, respectively. The open circles shown in the THz region are taken from Ref. [8] for comparison.

The generation of infrared pulses via down conversion can be modeled with a parametric amplification process under a depleted pump beam condition [27]:

$$I_i(r) = \left[ \left( \frac{\omega_i}{\omega_p} \right) I_p (1 - \text{sn}^2[(r - r_0)/l, r]) \right] \times \exp(-\alpha r) \quad (8)$$

where

$$1/l = \Gamma(\lambda) \sqrt{1 + \frac{I_s \omega_p}{I_p \omega_s}} \quad (9)$$

and

$$r_0/l = \frac{1}{2} \ln \left( 16 \left[ 1 + \frac{I_p \omega_s}{I_s \omega_p} \right] \right) \quad (10)$$

In Eqs. (8)-(10),  $I_p$  is the pump intensity;  $I_s$  is the seeding intensity;  $\Gamma(\lambda)$  is the parametric gain coefficient;  $\alpha$  is the absorption coefficient;  $\omega_j$ ,  $j = p, s$ , or  $i$  is the angular frequency of

the pump, the seeding and the IR pulses, respectively;  $r$  is length of the GaSe crystal. We note that  $sn$  in Eq. (8) is the Jacobian elliptic function resulting from an inversion operation of the elliptic integral [27].

By taking into account the experimentally determined temporal and spatial profiles of the laser pulses, the calculated output pulse energy without considering loss due to absorption in the crystal is presented as the dashed curve in Fig. 4-9(b). The theoretical prediction taking into account the loss is shown as the solid curve. Clearly the solid curve exhibits better agreement with the experimental data. This reflects significant effect of infrared absorption of GaSe on the DFG output. The Er:GaSe DFG generated higher output pulse energy than the pure GaSe DFG near 20  $\mu\text{m}$ , as shown by the open triangles in Fig. 4-9(b). This is attributed to lower absorption loss of Er:GaSe near 20  $\mu\text{m}$  as well as an increased second-order optical nonlinearity from erbium doping [14]. For comparison, the wavelength-dependent output data in THz region (see the open circles in Fig. 4-9(b)) are taken from the data reported by *Shi et al.* [8].

#### 4.4 Summary

We report a study of the effect of optical absorption on generation of coherent infrared radiation from mid-IR to THz region from GaSe crystal. The infrared-active modes of  $\epsilon$ -GaSe crystal at 237.0  $\text{cm}^{-1}$  and 213.5  $\text{cm}^{-1}$  were found to be responsible for the observed optical dispersion and infrared absorption edge. Based upon phase matching characteristics of GaSe for difference-frequency generation (DFG), new Sellmeier equations of GaSe were proposed. The output power variation with wavelength can be properly explained with the shape of parametric gain and the spectral profile of absorption coefficient of GaSe. The adverse effect of infrared absorption on (DFG) process can partially be compensated by doping GaSe crystal with erbium ions.

## References

- [1] A. Bianchi and M. Garbi, "Down-conversion in the 4-18  $\mu\text{m}$  range with GaSe and AgGaSe<sub>2</sub> nonlinear crystals," *Opt. Commun.* **30**, 122-124 (1979).
- [2] K. L. Vodopyanov, L. A. Kulevskii, V. G. Voevodin, A. I. Gribenyukov, K. R. Allakhverdiev, and T. A. Kerimov, "High efficiency middle IR parametric superradiance in ZnGeP<sub>2</sub> and GaSe crystals pumped by an erbium laser," *Opt. Commun.* **83**, 322-326 (1991).
- [3] A. O. Okorogu, S. B. Mirov, W. Lee, D. I. Crouthamel, N. Jenkins, A. Yu. Dergachev, K. L. Vodopyanov, and V. V. Badikov, "Tunable middle infrared downconversion in GaSe and AgGaS<sub>2</sub>," *Opt. Commun.* **155**, 307-312 (1998).
- [4] R. A. Kaindl, M. Wurm, K. Reimann, P. Hamm, A. M. Weiner, and M. Woerner, "Generation, shaping, and characterization of intense femtosecond pulses tunable from 3 to 20  $\mu\text{m}$ ," *J. Opt. Soc. Am. B* **17**, 2086-2094 (2000).
- [5] R. Huber, A. Brodschelm, F. Tauser, and A. Leitenstorfer, "Generation and field-resolved detection of femtosecond electromagnetic pulses tunable up to 41 THz," *Appl. Phys. Lett.* **76**, 3191-3193 (2000).
- [6] W. Shi, Y. J. Ding, X. Mu, and N. Fernelius, "Tunable and coherent nanosecond radiation in the range of 2.7-28.7  $\mu\text{m}$  based on difference-frequency generation in gallium selenide," *Appl. Phys. Lett.* **80**, 3889-3891 (2002).
- [7] K. Finsterbusch, A. Bayer, and H. Zacharias, "Tunable, narrow-band picosecond radiation in the mid-infrared by difference frequency mixing in GaSe and CdSe," *Appl. Phys. B* **79**, 457-462 (2004).
- [8] W. Shi, and Y. J. Ding, "A monochromatic and high-power terahertz source tunable in the ranges of 2.7-38.4 and 58.2-3540  $\mu\text{m}$  for variety of potential applications," *Appl. Phys. Lett.* **84**, 1635-1637 (2004).
- [9] T. Tanabe, K. Suto, J. -i. Nishizawa, and T. Sasaki, "Characteristics of terahertz-wave generation from GaSe crystals," *J. Phys. D: Appl. Phys.* **37**, 155-158 (2004).
- [10] V. G. Dmitriev, G. G. Gurzadyan, and D. N. Nikogosyan, *Handbook of Nonlinear Optical Crystals* (Springer, Berlin, 1997), pp. 166-169.
- [11] D. R. Suhre, N. B. Singh, V. Balakrishna, N. C. Fernelius, and F. K. Hopkins, "Improved crystal quality and harmonic generation in GaSe doped with indium," *Opt. Lett.* **22**, 775-777 (1997).
- [12] N. B. Singh, D. R. Suhre, W. Rosch, R. Meyer, M. Marable, N. C. Fernelius, F. K. Hopkins, D. E. Zelmon, and R. Narayanan, "Modified GaSe crystals for mid-IR

- applications,” *J. Cryst. Growth* **198**, 588-592 (1999).
- [13] S. Das, C. Ghosh, O. G. Voevodina, Yu. M. Andreev, and S. Yu. Sarkisov, “Modified GaSe crystal as a parametric frequency converter,” *Appl. Phys. B* **82**, 43-46 (2006).
- [14] Y. -K. Hsu, C. -W. Chen, J. Y. Huang, C. -L. Pan, J. -Y. Zhang, and C. -S. Chang, “Erbium doped GaSe crystal for mid-IR applications,” *Opt. Express* **14**, 5484-5491 (2006).
- [15] C. -L. Pan, C. -F Hsieh, R. -P. Pan, M. Tanaka, F. Miyamaru, M. Tani, and M. Hangyo, “Control of enhanced THz transmission through metallic hole arrays using nematic liquid crystal,” *Opt. Express* **13**, 3921-3930 (2005).
- [16] E. D. Palik, *Handbook of Optical Constants of Solids* (Academic, New York, 1998), Vol. III.
- [17] H. Yoshida, S. Nakashima, and A. Mitsuishi, “Phonon Raman Spectra of Layer Compound GaSe,” *Phys. Status Solidi B* **59**, 655-666 (1973).
- [18] M. Hayek, O. Brafman, and R. M. A. Lieth, “Splitting and Coupling of Lattice Modes in the Layer Compounds GaSe, GaS, and GaSe<sub>x</sub>S<sub>1-x</sub>,” *Phys. Rev. B* **8**, 2772-2779 (1973).
- [19] K. Allakhverdiev, T. Baykara, S. Ellialtioglu, F. Hashimzade, D. Huseinova, K. Kawamura, A. A. Kaya, A. M. Kulibekov (Gulubayov), and S. Onari, “Lattice vibrations of pure and doped GaSe,” *Mater Res. Bull.* **41**, 751-763 (2006).
- [20] B. L. Yu, F. Zeng, V. Kartazayev, R. R. Alfano, and K. C. Mandal, “Terahertz studies of the dielectric response and second-order phonons in a GaSe crystal,” *Appl. Phys. Lett.* **87**, 182104-1-3 (2005).
- [21] G. D. Boyd and D. A. Kleinman, “Parametric Interaction of Focused Gaussian Light Beams,” *J. Appl. Phys.* **39**, 3597-3639 (1968).
- [22] W. K. Jang, Q. Ye, D. Hammons, J. Eichenholz, J. Lim, M. Richardson, B. H. T. Chai, and E. W. Van Stryland, “Improved second-harmonic generation by selective Yb ion doping in a new nonlinear optical crystal YCa<sub>4</sub>O(BO<sub>3</sub>)<sub>3</sub>,” *IEEE J. of Quantum Electron.* **35**, 1826-1833 (1999).
- [23] K. L. Vodopyanov and L. A. Kulevskii, “New dispersion relationships for GaSe in the 0.65-18 μm spectral region,” *Opt. Commun.* **118**, 375-378 (1995).
- [24] K. R. Allakhverdiev, T. Baykara, A. K. Gulubayov, A. A. Kaya, J. Goldstein, N. Fernelius, S. Hanna, and Z. Salaeva, “Corrected infrared Sellmeier coefficients for gallium selenide,” *J. Appl. Phys.* **98**, 093515-1-6 (2005).

- [25] C. -W. Chen, Y. -K. Hsu, J. Y. Huang, C. -S. Chang, J. Y. Zhang, and C. -L. Pan, “Generation properties of coherent infrared radiation in the optical absorption region of GaSe crystal,” *Opt. Express* **14**, 10636-10644 (2006).
- [26] T. J. Wieting and M. Schluter (Eds.), *Electrons and Phonons in Layered Crystal Structures* (D. Reidel Publishing Company, Holland, 1979), pp. 338-340.
- [27] R. A. Baumgartner and R. L. Byer, “Optical Parametric Amplification,” *IEEE J. Quantum Electron.* **QE-15**, 432-444 (1979).



## Chapter 5

# Coherent generation and spectral synthesis of terahertz radiation with multiple stages of optical rectification

### 5.1 Introduction

A great amount of effort had recently been focused on developing terahertz (THz) science and technology for spectroscopy, security inspections, and biomedical imaging. Although free electron lasers and an energy-recovery linac are able to produce intense terahertz radiation in a wide frequency range [1, 2], cost effective access to these large-scale facilities is limited. For many applications, compact table-top terahertz sources are desirable. For example, a semiconductor biased with an electric or magnetic field and illuminated with an ultrashort laser pulse can produce an ultrafast current transient, which then radiates terahertz field efficiently [3, 4]. Terahertz radiation can also be generated by use of optical frequency mixing in nonlinear optical crystals [5-8]. Higher-order nonlinear optical processes, such as four-wave-mixing in plasma, can also be used [9, 10]. A variety of designs for THz emission [11-13] have been demonstrated.

Optical rectification (OR) is one of the promising methods to generate the terahertz radiation [5-7] with advantages of broadband terahertz radiation output, high saturation fluence for the pump pulses, and scalability. Generation of near single-cycle pulses centered at 0.5 THz frequency with pulse energy up to 10  $\mu$ J, 100  $\mu$ W average power, and 5 MW peak power was demonstrated [5]. A theoretical study of cascaded OR processes in nonlinear optical crystals for intense terahertz pulse generation was recently reported [14]. Similarly cascaded difference-frequency generation (DFG) had also been proposed [15]. Among many nonlinear optical crystals, GaSe is good for terahertz generation owing to its high second-order nonlinearity and wide transparency range [16]. Femtosecond terahertz pulses tunable up to 41 THz had been generated with a 90  $\mu$ m thick GaSe by use of a phase-matched OR process [6]. A narrow band terahertz radiation source with a wide tuning range had also been reported with a 2 cm thick GaSe DFG [8]. However, improving the generation efficiency of THz radiation with increasing crystal length encounters some difficulties: First, it is rather difficult to grow long GaSe crystals with good optical quality. Second, the pulse walk-off effect from the group velocity mismatch limits the effective

interaction length in nonlinear crystal. This leads to the useful length of GaSe for the generation of femtosecond terahertz radiation in the order of micrometer to millimeter. By avoiding the above-mentioned obstacles, we demonstrated in this study the generation of single-cycle high-amplitude terahertz radiation pulses by using multi-stage optical rectification in GaSe crystals.

## 5.2 Theoretical model and experimental methods

The nonlinear interacting processes between the optical and terahertz pulses in cascaded GaSe OR stages can be properly described with the coupled wave equations. Under the slowly-varying envelope approximation, the coupled-wave equations in frequency domain can be written as [14]:

$$\frac{d}{dz} E_{T,2} = -j \frac{\varepsilon_0 \mu_0 c d_{\text{eff}} \omega_{T,2}}{n(\omega_{T,2})} \int E_p(z, \omega_p + \omega_{T,2}) E_p^*(z, \omega_p) \exp(j\Delta k_{T,2} z) d\omega - \frac{\alpha_{T,2}}{2} E_{T,2}(z, \omega_{T,2}) \quad (1)$$

$$\frac{d}{dz} E_p = -j \frac{\varepsilon_0 \mu_0 c d_{\text{eff}} \omega_p}{n(\omega_{T,2})} \int E_p(z, \omega_p - \omega_{T,2}) E_{T,2}(z, \omega_{T,2}) \exp(j\Delta k_p z) d\omega - \frac{\alpha_p}{2} E_p(z, \omega_p) \quad (2)$$

where  $z$  is the propagation distance in GaSe;  $E_{T,2}$  and  $E_p$  denote the terahertz radiation field and the optical pump wave in the second-stage GaSe crystal;  $\varepsilon_0$  is the dielectric constant of vacuum;  $\mu_0$  is the permittivity of free space;  $c$  is the speed of light in vacuum;  $d_{\text{eff}}$  is the effective nonlinearity;  $\omega_{T,2}$  and  $\omega_p$  are the angular frequencies of the terahertz radiation and the optical pump wave;  $n(\omega_{T,2})$  and  $n(\omega_p)$  are the refractive index at the corresponding frequencies.  $\alpha_{T,2}$  and  $\alpha_p$  are the linear absorption coefficients of the terahertz radiation and the optical wave in the GaSe, respectively;  $\Delta k_{p, T,2}$  denotes the wave-vector mismatch between the pump and terahertz wave. The total terahertz field in time domain can be described by:

$$E_T = E_{T,1} \exp(j\omega_{T,1}\tau) + E_{T,2} \quad (3)$$

where  $E_{T,1}$  and  $E_{T,2}$  are the terahertz radiation fields from the first and the second OR stage, respectively;  $\tau$  denotes the propagation delay time between the two OR stages.

The pure GaSe crystals used for this study were grown by the Bridgman method. Raw materials were loaded in a well-cleaned quartz tube. The tube was then sealed and pumped down to below  $10^{-6}$  Torr. The crystal growth was initiated with a thermal gradient of 30 °C/cm and a growth rate of 2 cm/day. The experimental setup for our multi-stage OR is shown in Fig. 5-1. The pump laser was a 1-kHz amplified Ti: Sapphire laser with pulse energy of 700  $\mu\text{J}$  and duration of 270 fs. The typical average pump power on the GaSe crystals was about 130 mW and 150 mW for the first and second stage, respectively. The



pump beam diameter for both stages was adjusted to be about 3 mm. Both GaSe crystals were configured for non-phase-matched OR [17]. The terahertz radiation field generated from the first OR stage of 2 mm thick GaSe crystal was guided to the second OR stage of 3 mm thick GaSe. The terahertz pulses from the two OR stages were aligned collinearly with two gold-coated parabolic mirrors. We blocked the residual 800 nm laser beams with teflon plates. An indium-tin-oxide (ITO) glass plate, which can transmit the 800 nm laser pulses while partially reflects the terahertz radiation, was used as the beam combiner. The time delay between the two terahertz pulses was carefully controlled with a translation stage. An optical chopper was used in this experimental arrangement to simultaneously modulate the optical pump beams for the first and second GaSe OR stages. For monitoring the time-domain waveform of terahertz radiation, we employed the electro-optical sampling technique [18] with a 1 mm thick ZnTe crystal. Terahertz radiation generated from either the first or second stage, or both can be recorded without moving any optical element.

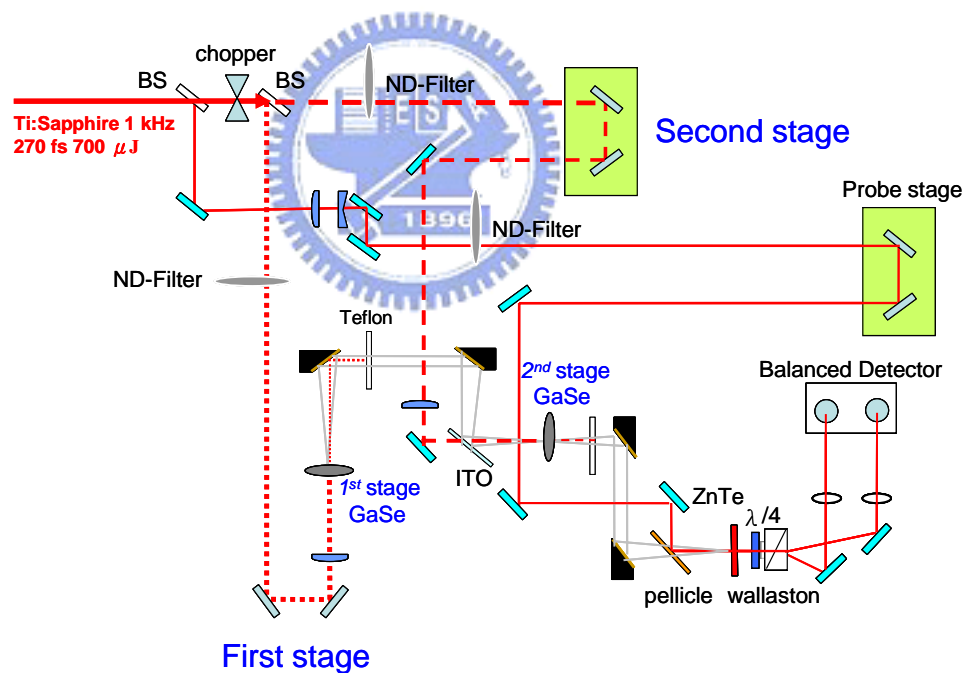


**Fig. 5-1** Schematic of coherent generation of terahertz radiation by multi-stage optical rectification in GaSe crystals. BS: Beam splitter; ND-Filter: Neutral Density filter; ITO: indium-tin-oxide glass plate;  $\lambda/4$ : quarter wave plate.

## 5.3 Results and Discussions

### 5.3.1 THz generation by optical rectification with azimuthal $\varphi$ angle dependence

Optical rectification is nonlinear optical behavior related to the second-order susceptibility. THz output from the OR is dependent on the value of the nonlinearity  $d_{eff}$ . The  $d_{eff}$  of the GaSe crystal is expressed as follows:

$$E_{THz} \propto d_{eff} = d_{22} \cos^2 \theta \cos 3\varphi \quad (4)$$

By selecting the suitable  $\varphi$  angles, THz peak electric field and the  $d_{eff}$  could be optimized. Figure 5-2 shows the THz time domain waveforms at different GaSe azimuthal  $\varphi$  angle. This relationship is attributed to the hexagonal crystal symmetry in the uniaxial crystal. It has been shown that the maximum signal is achieved when the GaSe emitter has its azimuthal angle set at  $|\cos 3\varphi| = 1$ , since the effective nonlinear coefficient of type-II phase matching is proportional to the value of  $\cos 3\varphi$ . Figure 5-3 presents the THz wave peak amplitude versus azimuthal  $\varphi$  angle for GaSe emitter.

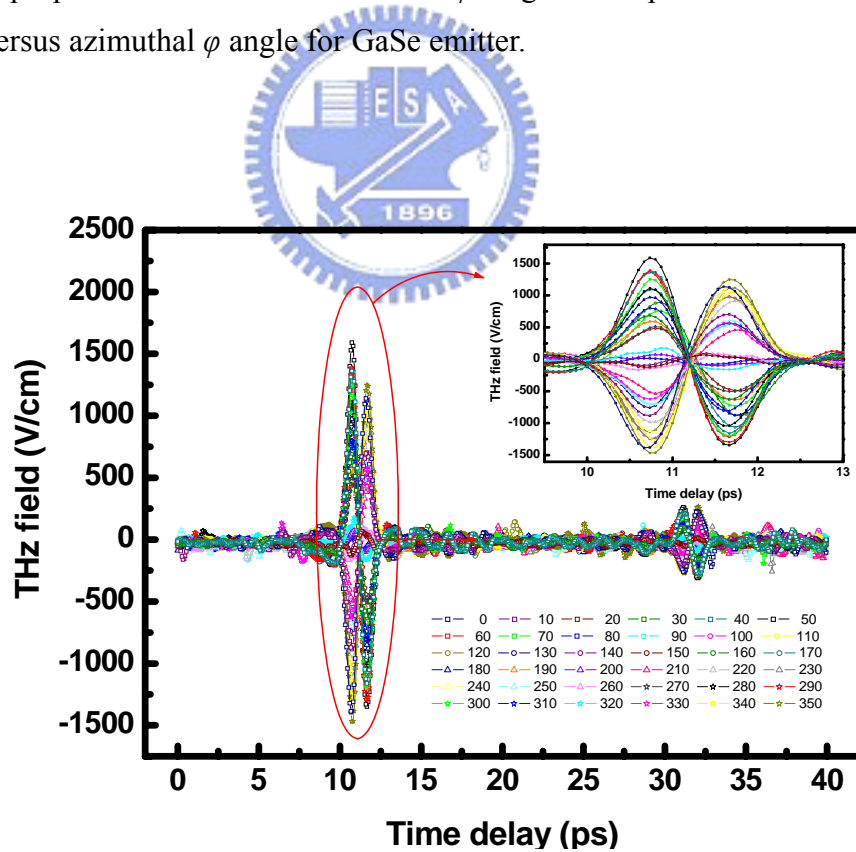


*Fig. 5-2 THz time domain waveforms at different GaSe azimuthal  $\varphi$  angle.*

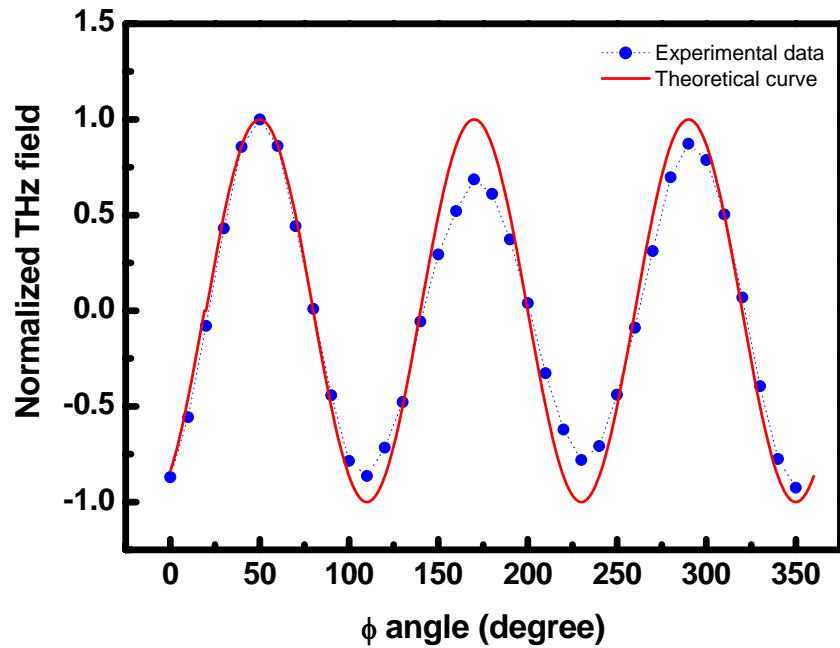


*Fig. 5-3 THz wave peak amplitude versus azimuthal  $\phi$  angle for GaSe emitter.*

### 5.3.2 High coherence between multiple stages of optical rectification

We first adjusted the terahertz pulses from the two GaSe OR stages to be overlapped spatially. The optical path length of the pump beam to the first GaSe stage was then varied to adjust the arrival time of the terahertz pulse at the second GaSe stage.

Figure 5-4 shows the field amplitude of the terahertz output from the second OR stage as a function of the arrival time of the seeding terahertz field. In this case, the terahertz field generated in the second stage is added to the incoming THz seeding field. We can also map out the seeding terahertz pulse profile by scanning the first stage delay line while blocking the pump pulse to the second GaSe crystal. The resulting seeding pulse profile was shown as the square-symbols in Fig. 5-4. High degree of mutual coherence between the terahertz fields from the two GaSe OR stages was clearly revealed.

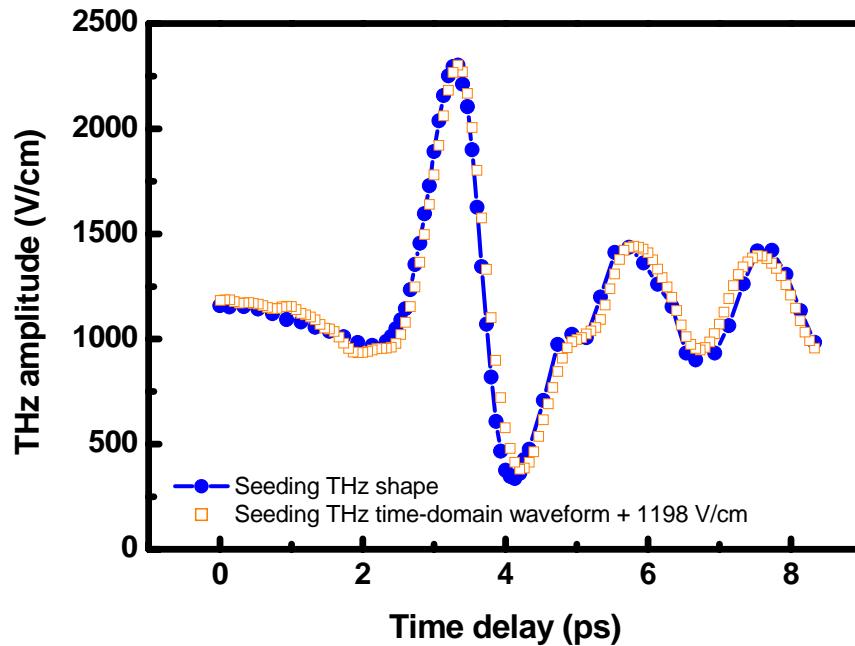
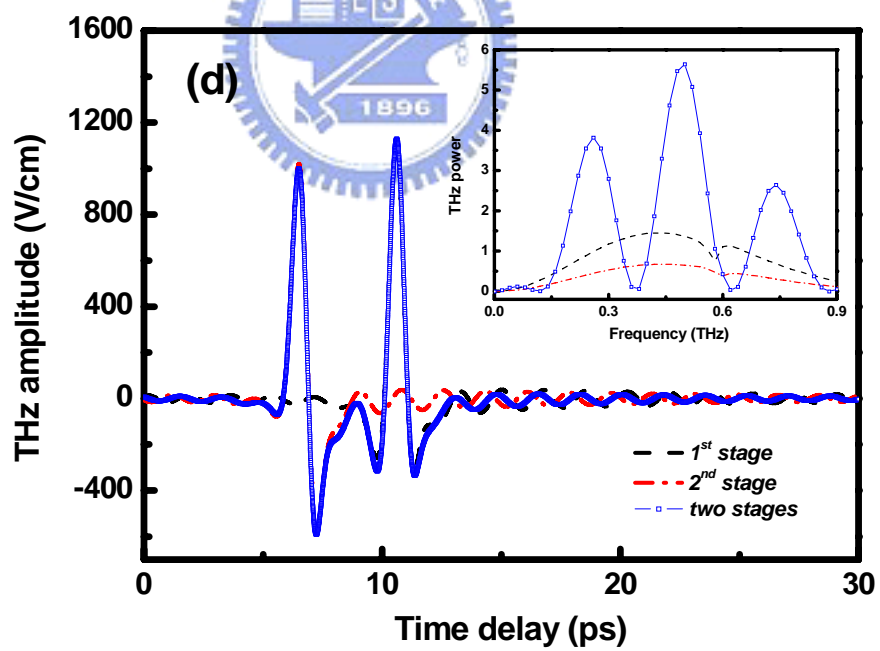
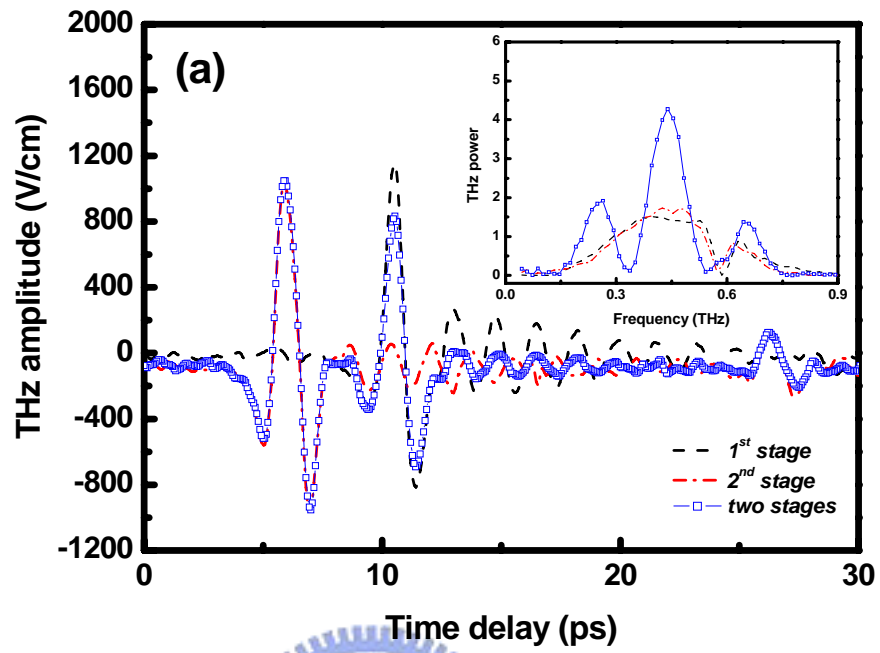


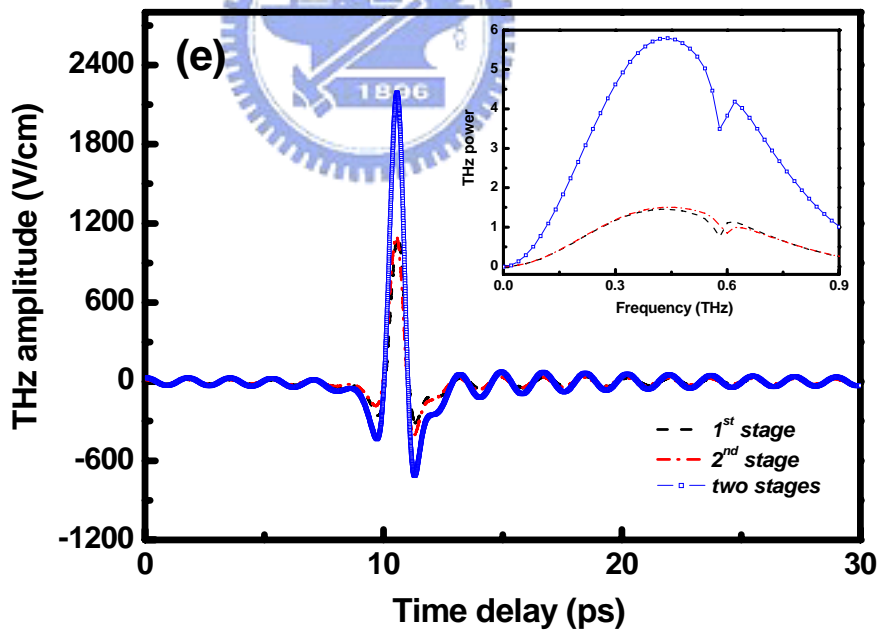
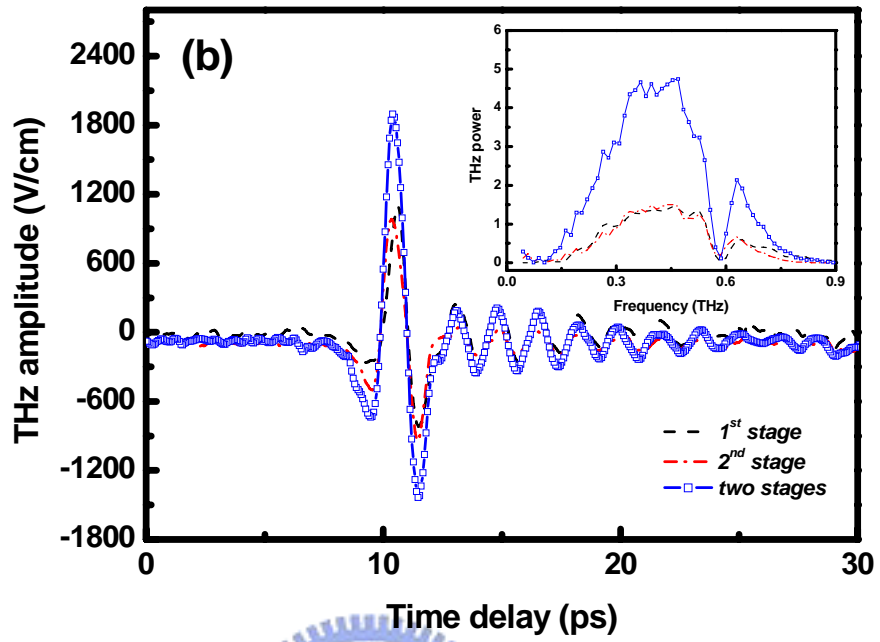
*Fig. 5-4 Time delay dependence of terahertz field amplitude after the second stage. Square-symbols present the terahertz time-domain waveform from the first stage, which is magnified for the easy comparison.*



### **5.3.3 THz coherent superposition and spectral synthesis by multiple stages of optical rectification**

Figure 5-5 shows the terahertz time-domain waveforms and the spectra at three different time delays between the two OR stages. In these figures, the signal from the first stage is presented as black dashed curve and the pulse from the second stage is displayed with the red dashed-dot line. The superposed THz pulses from both stages are shown as the blue curve with open squares. By adjusting the time delay, the terahertz fields from the two OR stages can be superposed constructively or destructively. To generate maximum terahertz field, the time delay of the two terahertz pulses should be adjusted for the best temporal overlap within 0.1 ps in our study, to yield constructive superposition over the entire spectral components involved.





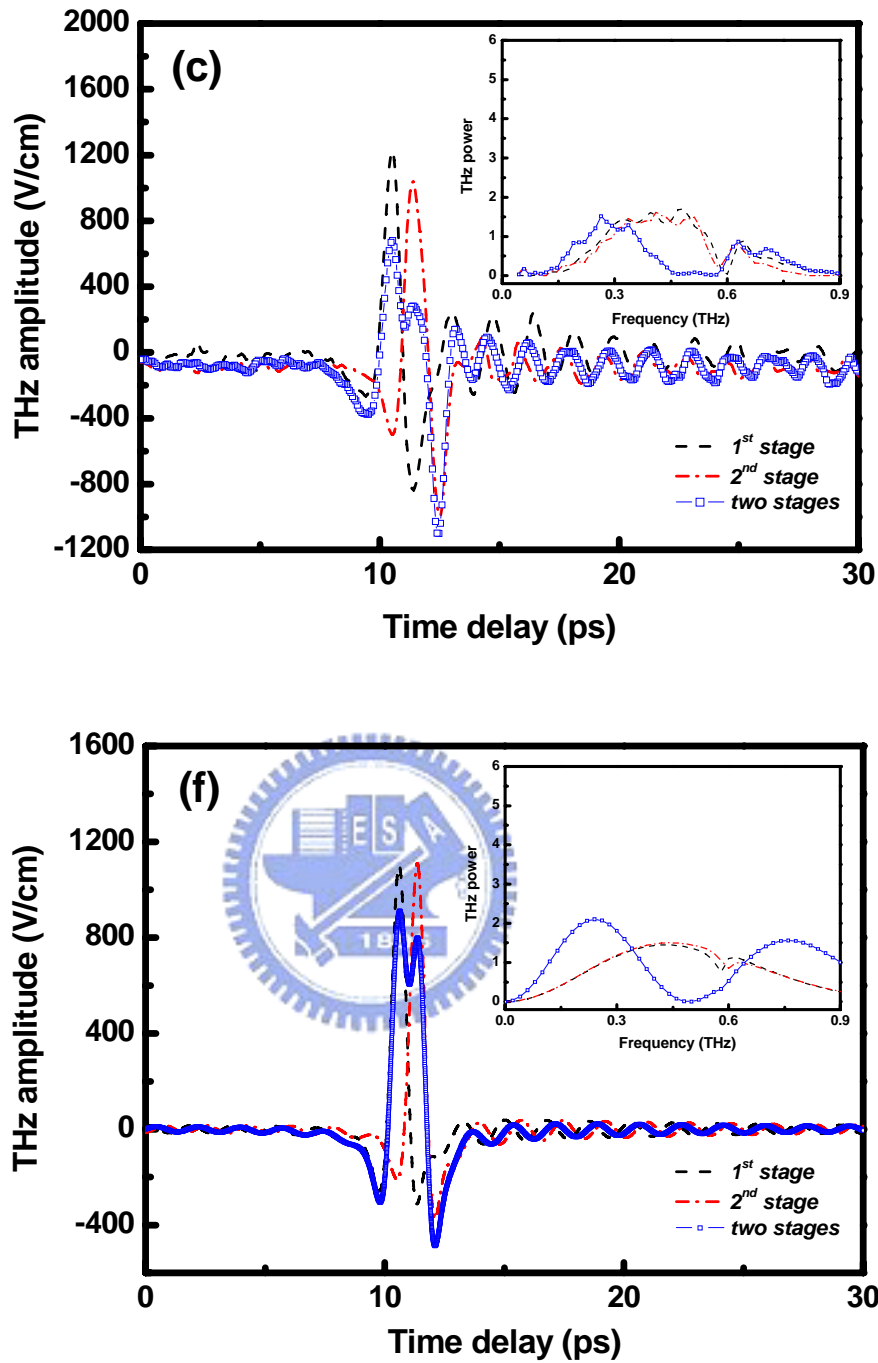


*Fig. 5-5 Terahertz time-domain waveforms from the first and second stage, and two stages. (a) (d) Terahertz pulse from the second stage leads that from the first stage; (b) (e) best overlapped between the terahertz pulses from two stages; (c) (f) terahertz pulse from the second stage lags behind that from the first stage. Inset: corresponding spectra of the terahertz radiation. Experimental measurement: (a) (b) (c); Theoretical simulation: (d) (e) (f).*



In Fig. 5-5(a), the main peak of terahertz field from the second OR stage leads that from the first stage. However, the trailing part of the THz pulse from the second stage still overlaps and interferes with the THz field from the first stage. The coherent superposition nature is more clearly revealed in the frequency domain shown in the inset of the Fig. 5-5(a). Parts of the terahertz spectral components from the two stages are constructively added to produce higher spectral power while some spectral regions superpose destructively to yield lower spectral power. Thus the coherent superposition with multiple terahertz radiation sources offers a potential for the synthesis of terahertz field. In Fig. 5-5(c), the terahertz pulse from the second stage lags behind that from the first stage in such a way that the main positive peak from the second stage overlaps with the negative amplitude of the THz pulse from the first stage. The destructive superposition yields a spectrum shown in the inset of Fig. 5-5(c). The destructive superposition is caused by out-of-phase mixing of the terahertz field from the first stage with the optical pump pulse in the second OR stage. The spectral phase content of the terahertz field can then be imprinted onto the pump pulse. In other words, when pump pulse in the second OR stage and terahertz field from the first stage are getting close and partly overlapped in the time domain, the seeding terahertz field will dominate the three-wave mixing process and lead to the output terahertz field profile variations. In the case of Fig. 5-5(c), the phase difference almost equals to  $\pi$  in the overlapped region between terahertz field from the first stage and the pump pulse in the second OR stage. Thus the terahertz field generated by the pump pulse in the second OR stage is then superposed with the first THz field to yield a much weaker terahertz radiation output.

The highest terahertz field amplitude can be obtained by synchronizing the first and second OR stages to attain constructive superposition of terahertz fields in the second OR stage. This can be done by seeding terahertz field with the correct phase at a proper arrival time relative to the optical pump pulse of the second stage. The output terahertz field possesses the property of the seeding terahertz field but with higher amplitude. The inset of Fig. 5-5(b) presents the spectra of the terahertz radiation fields to reveal the amplification nature of terahertz radiation pulse after the coherent superposition of the two stages.

The terahertz signal measured by the electro-optical sampling technique could be affected by the dispersion of the terahertz signal; the velocity-matching condition between the terahertz and optical pulses, and improper alignment [18]. The theoretical simulation of the two OR stages with Eqs. (1)-(3) is performed in order to remove the artifacts in the practical experiment. To allow for a straightforward comparison of the THz spectral profile

with the measured data, we assume a non-transform limited optical pump pulse with a spectral width  $< 1$  THz. The absorption by the optical phonon mode of GaSe at 0.586 THz was also included in our simulation. The calculation results corresponding to the three different experimental conditions are presented in Figs. 5-5(d), (e), and (f). The simulation results agree well with the experimental data shown in Figs. 5-5(a), (b) and (c). This confirms that the theoretical model used to depict the coherent multi-stage optical rectification processes in GaSe crystals is satisfactorily accurate.

### 5.3.4 Nonlinear absorption of THz wave in GaSe crystal

It is well known that linear and nonlinear optical absorption in GaSe have significant influences on THz generation process [19-21]. Free carriers can be generated via linear one-photon absorption and nonlinear two-photon absorption of GaSe pumped by a high-intensity near-infrared pulse. The terahertz radiation pulse propagating in the GaSe can then be attenuated by free carriers. To access the free carrier absorption effect at THz frequencies, we placed the optical chopper in our setup (see Fig. 5-1) at a different position such that only the probe and the first pump beam were modulated by the chopper. In this way, the THz radiation generated by the second GaSe crystal will not be detected. We measured the peak amplitude of the terahertz radiation field while varied the optical pump intensity of the second GaSe OR stage. The results, as shown in Fig. 5-6, reveal that the measured terahertz radiation field decreases when the optical pump intensity is higher than 2 GW/cm<sup>2</sup>. The decreasing THz radiation must be caused by free carrier absorption occurring in the second GaSe crystal.

From the measurement, the attenuation coefficients of the optical wave at 800 nm in GaSe by either linear absorption or nonlinear two-photon absorption were determined to be  $\alpha=1.44$  cm<sup>-1</sup> and  $\beta=1.48 \times 10^{-10}$  cm/W, respectively (see the inset (a) of Fig. 5-6). These coefficients obtained in current work are comparable to that published in Ref. [20, 21]. We can estimate the number density of free carriers  $N$  in GaSe with [21]:

$$N = \left[ \frac{F'}{\hbar\omega} \right] \left( \alpha + \beta \frac{F'}{\tau_p 2\sqrt{2}\sqrt{\pi}} \right) \quad (5)$$

where  $F'=F_0(1-R)$ ,  $F_0$  is the energy density of the optical excitation;  $\hbar\omega = 1.55eV$  ( $\lambda=800$  nm); the optical reflectivity at 800 nm wavelength is  $R=0.23$ ;  $\tau_p = \tau_{FWHM} / 2\sqrt{\ln 2}$  for the

pump pulse with pulse width  $\tau_{FWHM}$ . At our experimental condition, the number density of electron-hole pairs was estimated to be  $N=1.5\times 10^{16} \text{ cm}^{-3}$  with  $F=10 \text{ GW/cm}^2$ .

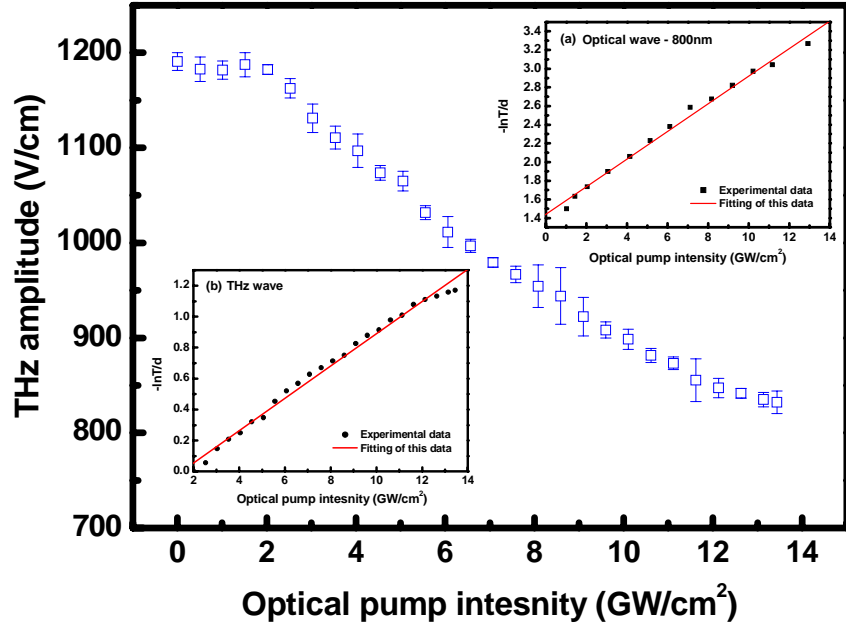


**Fig. 5-6** Terahertz radiation attenuation by the GaSe crystal under high intensity pump laser pulses. Inset (a): fitting of the experimental data for linear and nonlinear absorption coefficient of GaSe crystal pumped by 800 nm optical pulses. Inset (b): fitting of the experimental data for the absorption coefficient  $\alpha_{THz,fc}$  at terahertz frequency in GaSe crystal due to free carriers.

The absorption of terahertz radiation by the free carriers generated from the two-photon absorption of GaSe at high optical excitation level can be calculated with

$$T = \frac{I}{I_0} = \exp(-\alpha_{THz,fc} d) \quad (6)$$

Here  $I_0$  and  $I$  denote the terahertz intensity before and after the GaSe crystal under test;  $d$  is the crystal thickness; and  $\alpha_{THz,fc}$  the absorption coefficient at terahertz frequency, which is defined as

$$\alpha_{THz,fc} = \sigma_{THz} N \quad (7)$$

with  $N$  being the free carriers concentration and  $\sigma_{THz}$  the absorption cross-section of GaSe at terahertz frequency in the presence of free carriers. We can determine the absorption cross-section  $\sigma_{THz}$  by fitting the measured data to Eqs. (5)-(7), and the result are presented in

the inset (b) of Fig. 5-6. The deduced value of  $\sigma_{THz}$  lies in the range of  $(1.3 - 5.9) \times 10^{-17} \text{ cm}^2$ . *Kulibekov et al.* had reported the value of absorption cross-section for the free carriers at the optical frequencies ( $\lambda=626 \text{ nm}$ ) to be about  $(4 - 6) \times 10^{-19} \text{ cm}^2$  [21]. Compared to the optical pulses, the terahertz pulses possess the much lower photon energies ( $E=4 \text{ meV}$ ). As a result of the photon energy of THz wave is about 4 meV for 1 THz, which approximately equals to the binding energy of the excitons in many semiconductors, thus the weak terahertz signals are severely and easily absorbed by the free carriers. Accordingly, it is reasonable that the value of absorption cross-section for the free carriers at the terahertz frequencies measured in this work is two orders of magnitude larger than that published in Ref. [21].

### 5.3.5 Pump power and absorption dependence of the THz wave output

We further examined the power dependence of the terahertz radiation generated by optical rectification. Figure 5-7 shows the terahertz radiation output from the second OR stage without seeding as a function of optical pump intensity.

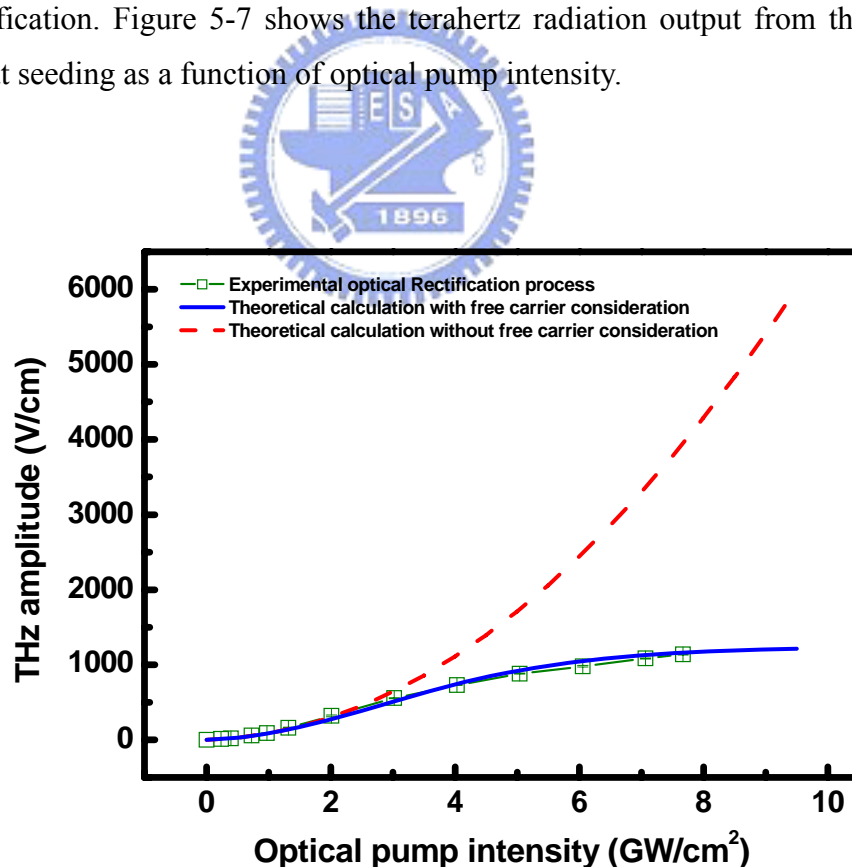


*Fig. 5-7 Output terahertz field amplitude under different pump intensity.*

A sub-linear dependence was found when the pump intensity is above  $2 \text{ GW/cm}^2$ , which can be attributed to the absorption of terahertz radiation by the free carriers generated by the pump pulses at 800 nm. All the calculation results were re-scaled properly in order to compare with the experimental data. We modeled the OR generated terahertz radiation with Eq. (1). The red curve in Fig. 5-7 indicates the terahertz output by taking into account the linear optical absorption effect only. The terahertz output increases significantly with the pump intensity. When free carrier generation from both the linear and nonlinear two-photon absorption were taken into account in the calculation, the result is presented as the blue-colored curve in Fig. 5-7. The terahertz output saturates at high pump level, agreeing well with our measured data. The excellent agreement indicates that the free carrier absorption effect places an upper limit on the terahertz radiation intensity at high pump level.

Power saturation of the terahertz radiation from ZnTe crystal at high pumping level had also been reported and was attributed to two-photon absorption of the optical excitation beam [22, 23]. The limitation on terahertz radiation output by two-photon absorption can be avoided with lower excitation level by using larger beam size. The generation of high power terahertz radiation is therefore limited only by the finite interaction length of nonlinear optical process used.

The GaSe crystal thicknesses used in this work are 2 mm and 3 mm for the first and second OR stages, respectively. The pumping level for both stages is about  $7 \text{ GW/cm}^2$ . By using one OR stage with single 5 mm thick GeSe crystal pumped at higher level of  $14 \text{ GW/cm}^2$ , the excess part of the crystal over the interaction length simply produces more free carriers and causes more power loss of terahertz radiation output. We estimated the peak electric field of the terahertz radiation output from the single OR stage to be 1224 V/cm. This value is only one half of that from two coherently coupled OR stages, which yields an output of 2285 V/cm without optimization.

Intense table-top terahertz radiation source had been demonstrated with large-aperture photoconductive switches [24]. However, some drawbacks were encountered. For example, the pulsed high voltage bias produces excess electrical noise and the terahertz output saturates at relatively low excitation fluence. Terahertz pulses with high peak electric fields can also be produced with air plasma [9]. In this method, high pump intensity up to  $\text{TW/cm}^2$  is needed to effectively generate high-order nonlinear process in the plasma. Coherently coupled OR stages reported here offers an alternative for high-intensity THz pulse generation at lower pump intensity than that used in plasma THz source. In comparison to

large-aperture photoconductive switches, the OR THz generation scheme produces broad-bandwidth THz pulses, which may be more suited for time-resolved spectroscopic applications. Micro-joule level terahertz pulse had been reported by using a large OR emitter [25]. Micro-joule level terahertz pulse could be actually obtained by enlarge the pump pulse diameter and upscale the pump pulse energy [5, 25]. In practice, the conversion efficiency of terahertz generation is usually limited by Manley-Rowe relation to the order about  $10^{-6} - 10^{-4}$  [5, 8, 9, 13, 24, 25]. Conversion efficiencies much higher than the Manley-Rowe limit had been theoretical verified by cascaded difference frequency generation processes under the assumption of ideal phase-matching condition and no absorption [14-15]. Therefore, high conversion efficiency can be achieved with multi-stage OR scheme. The multi-stage OR technique can overcome in principle the limitations on the finite interaction length and generate higher terahertz field amplitude than from one thick crystal. The price paid for the multi-stage generation of terahertz radiation is a more complex set-up and precise alignment between stages.

## 5.4 Summary

Generation of single-cycle terahertz pulses by multiple optical rectification stages using GaSe crystals was experimentally demonstrated. By properly adjusting the time delay between the pump pulses to the two OR stages, the terahertz radiation field generated by the second stage can be constructively superposed to the seeding terahertz field from the first stage. Free carrier absorption effect places an upper limit on the terahertz radiation intensity at high pump level; and the severe free carriers induced absorption cross-section for terahertz radiation is also quantitatively determined. The technique can be useful for the generation of single-cycle high-amplitude terahertz pulse, which is not limited by the pulse walk-off effect from group velocity mismatch.

## References

- [1] G. M. H. Knippels, X. Yan, A. M. MacLeod, W. A. Gillespie, M. Yasumoto, D. Oepts, and A. F. G. van der Meer, "Generation and complete electric-field characterization of intense ultrashort tunable far-infrared laser pulses," *Phys. Rev. Lett.* **83**, 1578-1581 (1999).
- [2] G. L. Carr, M. C. Martin, W. R. McKinney, K. Jordan, G. R. Neil, G. P. Williams, "High-power terahertz radiation from relativistic electrons," *Nature*, **420**, 153-156 (2002).
- [3] J. T. Darrow, X. -C. Zhang, D. H. Auston, and J. D. Morse, "Saturation properties of large-aperture photoconducting antennas," *IEEE J. Quantum Electron.* **28**, 1607-1616 (1992).
- [4] C. Weiss, R. Wallenstein, and R. Beigang, "Magnetic-field-enhanced generation of terahertz radiation in semiconductor surfaces," *Appl. Phys. Lett.* **77**, 4160-4162 (2000).
- [5] K. -L. Yeh, M. C. Hoffmann, J. Hebling, and K. A. Nelson, "Generation of 10  $\mu$ J ultrashort terahertz pulses by optical rectification," *Appl. Phys. Lett.* **90**, 171121-1-3 (2007).
- [6] R. Huber, A. Brodschelm, F. Tauser, and A. Leitenstorfer, "Generation and field-resolved detection of femtosecond electromagnetic pulses tunable up to 41 THz," *Appl. Phys. Lett.* **76**, 3191-3193 (2000).
- [7] Q. Wu and X. -C. Zhang, "Free-space electro-optics sampling of mid-infrared pulses," *Appl. Phys. Lett.* **71**, 1285-1286 (1997).
- [8] W. Shi, and Y. J. Ding, "A monochromatic and high-power terahertz source tunable in the ranges of 2.7-38.4 and 58.2-3540  $\mu$ m for variety of potential applications," *Appl. Phys. Lett.* **84**, 1635-1637 (2004).
- [9] T. Bartel, P. Gaal, K. Reimann, M. Woerner, and T. Elsaesser, "Generation of single-cycle THz transients with high electric-field amplitudes," *Opt. Lett.* **30**, 2805-2807 (2005).
- [10] J. Dai, X. Xie, and X. -C. Zhang, "Terahertz wave amplification in gases with the excitation of femtosecond laser pulses," *Appl. Phys. Lett.* **91**, 211102-1-3 (2007).
- [11] X. -C. Zhang, and D. H. Auston, "Optoelectronic measurement of semiconductor surfaces and interfaces with femtosecond optics," *J. Appl. Phys.* **71**, 326-338 (1992).
- [12] L. Xu, X. -C. Zhang, D. H. Auston, and B. Jalali, "Terahertz radiation from large aperture Si p-i-n diodes," *Appl. Phys. Lett.* **59**, 3357-3359 (1991).



- [13] A. Dreyhaupt, S. Winnerl, T. Dekorsy, and M. Helm, "High-intensity terahertz radiation from a microstructured large-area photoconductor," *Appl. Phys. Lett.* **86**, 121114-1-3 (2005).
- [14] T. Hattori and K. Takeuchi, "Simulation study on cascaded terahertz pulse generation in electro-optic crystals," *Opt. Express* **15**, 8076-8093 (2007).
- [15] M. Cronin-Golomb, "Cascaded nonlinear difference-frequency generation of enhanced terahertz wave production," *Opt. Lett.* **29**, 2046-2048 (2004).
- [16] V. G. Dmitriev, G. G. Gurzadyan, and D. N. Nikogosyan, *Handbook of Nonlinear Optical Crystals* (Springer, Berlin, 1997), pp. 166-169.
- [17] R. A. Kaindl, D. C. Smith, M. Joschko, M. P. Hasselbeck, M. Woerner, and T. Elsaesser, "Femtosecond infrared pulses tunable from 9 to 18  $\mu\text{m}$  at an 88-MHz repetition rate," *Opt. Lett.* **23**, 861-863 (1998).
- [18] Q. Wu, and X. -C. Zhang, "Free-space electro-optic sampling of terahertz beams," *Appl. Phys. Lett.* **67**, 3523-3525 (1995).
- [19] K. L. Vodopyanov, S. B. Mirov, V. G. Voevodin, and P. G. Schunemann, "Two-photon absorption in GaSe and CdGeAs<sub>2</sub>," *Opt. Comm.* **155**, 47-50 (1998).
- [20] I. B. Zotova, and Y. J. Ding, "Spectral measurements of two-photon absorption coefficients for CdSe and GaSe crystals," *Appl. Opt.* **40**, 6654-6658 (2001).
- [21] A. M. Kulibekov, K. Allakhverdiev, D. A. Guseinova, E. Yu. Salaev, and O. Baran, "Optical absorption in GaSe under high-density ultrashort laser pulses," *Opt. Comm.* **239**, 193-198 (2004).
- [22] T. Löffler, T. Hahn, M. Thomson, F. Jacob, and H. G. Roskos, "Large-area electro-optic ZnTe terahertz emitters," *Opt. Express* **13**, 5353-5362 (2005).
- [23] F. G. Sun, W. Ji, and X. -C. Zhang, "Two-photon absorption induced saturation of THz radiation in ZnTe," in *Conference on Lasers and Electro-Optics*, OSA Technical Digest (Optical Society of America, Washington DC, 2000), 479-480.
- [24] E. Budiarto, J. Margolies, S. Jeong, J. Son, and J. Bokor, "High-intensity terahertz pulses at 1-kHz repetition rate," *IEEE J. Quantum Electron.* **32**, 1839-1846 (1996).
- [25] F. Blanchard, L. Razzari, H. -C. Bandulet, G. Sharma, R. Morandotti, J. -C. Kieffer, T. Ozaki, M. Reid, H. F. Tiedje, H. K. Haugen, and F. A. Hegmann, "Generation of 1.5  $\mu\text{J}$  single-cycle terahertz pulses by optical rectification from a large aperture ZnTe crystal," *Opt. Express* **15**, 13212-13220 (2007).

## Chapter 6

# The study of terahertz optical parametric amplification in $\epsilon$ -GaSe crystals

### 6.1 Introduction

During the last decade, time-domain THz spectroscopy and imaging have become widely used techniques in several fields of physics, chemistry and biology [1]. Probably one of the most important present challenges of THz technology is up-scaling the THz pulse energy to a level suitable for nonlinear spectroscopy. So far the generation of THz pulses for studies of nonlinear phenomena usually requires complex machines. For instance, free electron lasers can deliver THz pulses with 17  $\mu\text{J}$  energy [2]; and an energy-recovery linac has produced THz pulses up to 20 W average power [3] and 100  $\mu\text{J}$  energy per pulse [4]. Nevertheless, the synchronization of two such THz pulses or of THz pulses with optical pulses with sub-picosecond accuracy is difficult [2] or is not yet possible at all [3]. Furthermore, the cost effective access to these large-scale facilities is limited.

So far photoconductive switches produce THz pulses with high energy up to 0.4  $\mu\text{J}$  [5] and higher average power  $\sim 40 \mu\text{W}$  [6]. The spectral maximum of these pulses, however, is below 1 THz. In contrast, optical rectification can generate THz pulses with spectral maximum even at a few tens of THz [7]. As usual for nonlinear processes, generation of high energy pulses requires phase-matching between the optical and the THz pulses. Quasi-phase-matching can be obtained in periodically poled  $\text{LiNbO}_3$  (PPLN) crystal. For such a situation, tilting of the pump pulse front by diffraction off a grating has been proposed to reach velocity matching in  $\text{LiNbO}_3$  [8-11]. Very recently, this method generated terahertz pulses with 10  $\mu\text{J}$  of energy, which corresponds to 100  $\mu\text{W}$  average power and 5 MW peak power [12].

As a promising nonlinear optical medium, femtosecond laser-induced plasma in gases has been studied intensively over the past several years. Recently, The generation of single-cycle terahertz pulses via four-wave mixing of the fundamental and the second harmonic of 25 fs pulses from a Ti: sapphire amplifier in air plasma was recently reported [13]. The energy of the terahertz pulses was around 30 nJ, which corresponds to the created peak terahertz electric field as high as 400 kV/cm. Recently, *Dai et al.* reported the

experimental demonstration of terahertz wave amplification in femtosecond-laser-induced air plasma [14]. The amplification effect is attributed to four-wave-mixing optical parametric processes. This demonstration provides a potential way toward intense terahertz wave sources for nonlinear terahertz optoelectronics. A peak amplification factor of about 65% is measured with total optical excitation intensity of  $8 \times 10^{14}$  W/cm<sup>2</sup>. The amplification effect occurs within a time scale of less than 400 fs of the onset of ionization processes due to the optical excitation pulse duration. Consequently, Table 6-1 shows a list of several promising methods for the generation of high power THz wave.

In nonlinear optics field, optical parametric amplification (OPA) technique has been widely applied to amplify the weak signal in the range from visible to infrared frequency spectra [15]. The high gain for the weak signal can be achieved by choosing the suitable nonlinear optical crystals. Accordingly, in this work, we attempt to enhance the weak pulse energy of THz radiation by means of the OPA technique associated with the GaSe crystal which possesses high nonlinear coefficient and low absorption coefficient at THz frequencies.



**Table 6-1 List of the numerous methods for high power THz generation**

| Method   | Paper                | Power                     | Energy                  | Electric field | Note                             |
|--|----------------------|---------------------------|-------------------------|----------------|----------------------------------|
| Free-electron lasers (FELs)  | G.M.H.Knippels(1999) | PP~1 MW                   | 17 $\mu$ J              |                |                                  |
| Energy-recovery linac<br>(subpicosecond electron<br>bunches in an accelerator) | G.L.Carr(2002)       | AP~20 W                   |                         |                |                                  |
| Laser-plasma accelerated<br>electron bunch                                     | W. P. Leemans(2003)  |                           | 100 $\mu$ J             |                |                                  |
| Pulse front tilting (OR)   | J. Hebling(2002)     | AP~1.1 $\mu$ W            | 5.5 pJ                  |                | LiNbO <sub>3</sub>               |
| Tilted pulse front (OR)<br>LiNbO <sub>3</sub><br>(Tuning range 1-4.4 THz)      | J. Hebling(2004)     |                           | 400 pJ<br>(77K)<br>3.4% |                | 10K                              |
| Tilted pulse front (OR)<br>LiNbO <sub>3</sub>                                  | A. G. Stepanov(2005) |                           | 240 nJ<br>10%           |                | (77K)<br>[ $5 \times 10^{-4}$ ]  |
| Tilted pulse front (OR)<br>0.6%MgO doped LiNbO <sub>3</sub>                    | K. L. Yeh(2007)      | AP~100 $\mu$ W<br>PP~5 MW | 10 $\mu$ J<br>45%       | 250 kV/cm      | 10 Hz<br>[ $6 \times 10^{-4}$ ]  |
| Large aperture ZnTe (OR)<br>(RR:100 MHz)                                       | F.Blanchard(2007)    | AP~150 $\mu$ W            | 1.5 $\mu$ J             |                | 3THz<br>[ $3.1 \times 10^{-5}$ ] |
| Large-aperture GaAs<br>photo-conductive switches                               | E. Budiarto(1996)    |                           | 0.4 $\mu$ J             |                | [ $8 \times 10^{-4}$ ]           |
| Photo-conductive switches  | G. Zhao(2002)        | AP~40 $\mu$ W             |                         | 95 V/cm        |                                  |
| DFM : GaSe (30 $\mu$ m)  | K. Reimann(2003)     |                           | 12 nJ                   | 1 MV/cm        | BW=30 THz                        |
| Spatial filtering technique<br>(PM-GaSe)                                       | D. F. Gordon(2006)   | PP~1.5 kW                 | 6 nJ                    |                | Tenability<br>0.7-2 THz          |
| DFG (5ns) : GaSe   | W.Shi(2004)          | PP~209 W                  | 1.045 $\mu$ J           |                | [ $5.5 \times 10^{-4}$ ]         |

|   |                     |  |                   |           |  |
|---|---------------------|--|-------------------|-----------|--|
| (GaSe: 20mm)  |                     | (at 196 $\mu\text{m}$ )<br>(at 1.53 THz) | 0.055%            |           |  |
| DFG (5ns) : GaSe<br>(GaSe: 15mm)                                    | W. Shi(2002)        | PP~69.4 W<br>(at 196 $\mu\text{m}$ )     | 347 nJ            |           |  |
| DFG (5ns) : GaP   | W. Shi(2005)        | PP~15.6 W<br>(at 173 $\mu\text{m}$ )     | 78 nJ             |           | $[3 \times 10^{-5}]$                                     |
| PM-OR (GaSe)  | R. Huber(2000)      |  |                   | 1000 V/cm | Tunable 41 THz<br>(5 $\mu\text{m}$ -3000 $\mu\text{m}$ ) |
| Semi-insulating GaAs emitter<br>(Ti:sapphire oscillator)            | G. Zhao(2002)       | AP~40 $\mu\text{W}$                      |                   | 95 V/cm   |  |
| Interdigitated electrode metal-semiconductor-metal (MSM) structure. | A. Dreyhaupt(2005)  |  |                   | 85 V/cm   |  |
| Interdigitated photoconducting device (RR:78 MHz)                   | A. Dreyhaupt(2006)  | AP~190 $\mu\text{W}$                     |                   | 1.5 kV/cm | $[2.5 \times 10^{-4}]$                                   |
| Photoconductive SI-GaAs (line excitation)                           | J. H. Kim(2005)     | AP~10 mW<br>0.1%                         |                   |           |  |
| Orientation-patterned GaAs (2 $\mu\text{m}$ pump, 100MHz, 120fs)    | G. Imeshev(2006)    | AP~3.3 mW                                |                   |           | $[1.6 \times 10^{-6}]$                                   |
| Pulsed biased GaAs  | D.You(1993)         |  | 0.8 $\mu\text{J}$ | 150 kV/cm | < 500 fs ,<br>1.5 THz                                    |
| FWM (N <sub>2</sub> )   | T. Bartel(2005)     |  | 30 nJ             | 400 kV/cm | 0.3-7 THz<br>$[6 \times 10^{-5}]$                        |
| Four-wave rectification in air                                      | D.J.Cook(2000)      |  | 5 pJ              | 2 kV/cm   | Power spectrum peaks near 2 THz                          |
| FWM   | M.Kress(2004)       |  |                   | 6.8 kV/cm |  |
| FWM in air plasma   | H. Zhong(2006)      |  |                   | 10 kV/cm  | Plasma length > 10 mm<br>Divergence angle < 10°          |
| FWM in air plasma   | X.-C. Zhang (2007)  |  |                   | 350 kV/cm |  |
| Magnetic field enhanced (InAs)                                      | N.Sarukura(1998)    | AP~650 $\mu\text{W}$                     | 6.5~8 pJ          |           | RR:80-100 MHz<br>BW=1.7 T<br>Pump:1.5W                   |
| Magnetic field enhanced (InAs)                                      | R. McLaughlin(2000) | AP~12 $\mu\text{W}$                      | 0.15 pJ           |           | RR:82 MHz<br>170K ,<br>BW=8T                             |

✧ *AP : Average Power; PP : Peak Power; RR : Repetition Rate; BW : Band Width; [ ] : Conversion efficiency*

## 6.2 Theoretical model and experimental methods

### 6.2.1 The principle of OPA process

The principle of OPA is quite simple: in a suitable nonlinear crystal, a high frequency and high intensity beam (the pump beam, at frequency  $\omega_p$ ) amplifies a lower frequency, lower intensity beam (the signal beam, at frequency  $\omega_s$ ); in addition a third beam (the idler beam, at frequency  $\omega_i$ , with  $\omega_i < \omega_s < \omega_p$ ) is generated. A schematic of the experimental configuration of collinear type of OPA is represented in Fig. 6-1. In the interaction, energy conservation

$$\hbar\omega_p = \hbar\omega_s + \hbar\omega_i \quad (1)$$

is satisfied; for the interaction to be efficient, also the momentum conservation (or phase matching) condition

$$\hbar k_p = \hbar k_s + \hbar k_i \quad (2)$$

where  $k_p$ ,  $k_s$ , and  $k_i$  are the wave vectors of pump, signal, and idler, respectively, must be fulfilled. The signal frequency to be amplified can vary in principle from  $\omega_p/2$  (the so-called degeneracy condition) to  $\omega_p$ , and correspondingly the idler varies from  $\omega_p/2$  to 0; at degeneracy, signal and idler have the same frequency. In summary, the OPA process transfers energy from a high-power, fixed frequency pump beam to a low-power, variable frequency signal beam, thereby generating also a third idler beam. To be efficient, this process requires very high intensities of the order of tens of  $\text{GW}/\text{cm}^2$ ; it is therefore eminently suited to femtosecond laser systems, which can easily achieve such intensities even with modest energies, of the order of a few micro-joules.

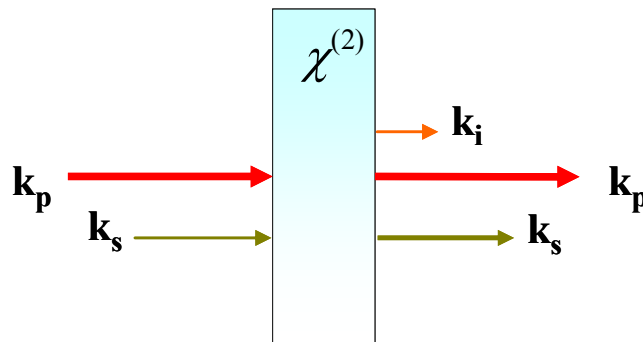


*Fig. 6-1 The experimental configuration of collinear type of OPA.*

We now address the problem of phase matching: to achieve maximum gain, we must satisfy the phase matching condition,  $\Delta k=0$ , which can be recast in the form

$$n_p = \frac{n_i \omega_i + n_s \omega_s}{\omega_p} \quad (3)$$

It is easy to show that this condition cannot be fulfilled in bulk isotropic materials in the normal dispersion region ( $n_i < n_s < n_p$ ). In some birefringent crystals, phase matching can be achieved by choosing for the higher frequency pump wave ( $\omega_p$ ) the polarization direction giving the lower refractive index. In the case, common in femtosecond OPA, of negative uniaxial crystals ( $n_e < n_o$ ), the pump beam is polarized along the extraordinary direction. If both signal and idler beams have the same ordinary polarization (perpendicular to that of the pump beam) we talk about type-I (or  $o_s+o_i \rightarrow e_p$ ) phase matching. If one of the two is polarized parallel to the pump beam, we talk about type II phase matching; in this case either the signal ( $e_s+o_i \rightarrow e_p$ ) or the idler ( $o_s+e_i \rightarrow e_p$ ) can have the extraordinary polarization [16]. Both types of phase matching can be used and have their specific advantages according to the system under consideration. Usually the phase matching condition is achieved by adjusting the angle  $\theta_m$  between the wave vector of the propagating beams and the optical axis of the nonlinear crystal (angular phase matching). As an example, we consider the case of a negative uniaxial crystal, for which type-I phase matching is achieved when [17]

$$n_{ep}(\theta_m) \omega_p = n_{os} \omega_s + n_{oi} \omega_i \quad (4)$$

which allows to compute  $n_{ep}(\theta_m)$ . Recalling the dependence of the extraordinary index on the propagation direction in uniaxial crystals

$$\frac{1}{n_{ep}^2(\theta_m)} = \frac{\sin^2(\theta_m)}{n_{ep}^2} + \frac{\cos^2(\theta_m)}{n_{op}^2} \quad (5)$$

where  $n_{ep}$  and  $n_{op}$  are the principal extraordinary and ordinary refractive indexes at the pump wavelength, the phase matching angle can then be obtained as

$$\theta_m = a \sin \left[ \frac{n_{ep}}{n_{ep}(\theta_m)} \sqrt{\frac{n_{op}^2 - n_{ep}^2(\theta_m)}{n_{op}^2 - n_{ep}^2}} \right] \quad (6)$$

## 6.2.2 Satisfactory phase matching condition

As a result of the promising optical properties of GaSe crystal in THz range, such as large birefringence, high nonlinearity and low absorption coefficient, we supposed that GaSe can be a good gain medium for the OPA process. GaSe crystal is a birefringent crystal, thus its Sellmeier equations can be express as follows:

$$n_o^2 = 7.37 + \frac{0.405}{\lambda^2} + \frac{0.0186}{\lambda^4} + \frac{0.0061}{\lambda^6} + \frac{3.1436\lambda^2}{\lambda^2 - 2193.8} + \frac{0.017\lambda^2}{\lambda^2 - 262177.5577} \quad (7)$$

$$n_e^2 = 5.76 + \frac{0.3879}{\lambda^2} - \frac{0.2288}{\lambda^4} + \frac{0.1223}{\lambda^6} + \frac{0.4206\lambda^2}{\lambda^2 - 1780.3} \quad (8)$$

where  $n_o$  and  $n_e$  is the ordinary and extraordinary refractive index, respectively;  $\lambda$  is the wavelength in micrometers.

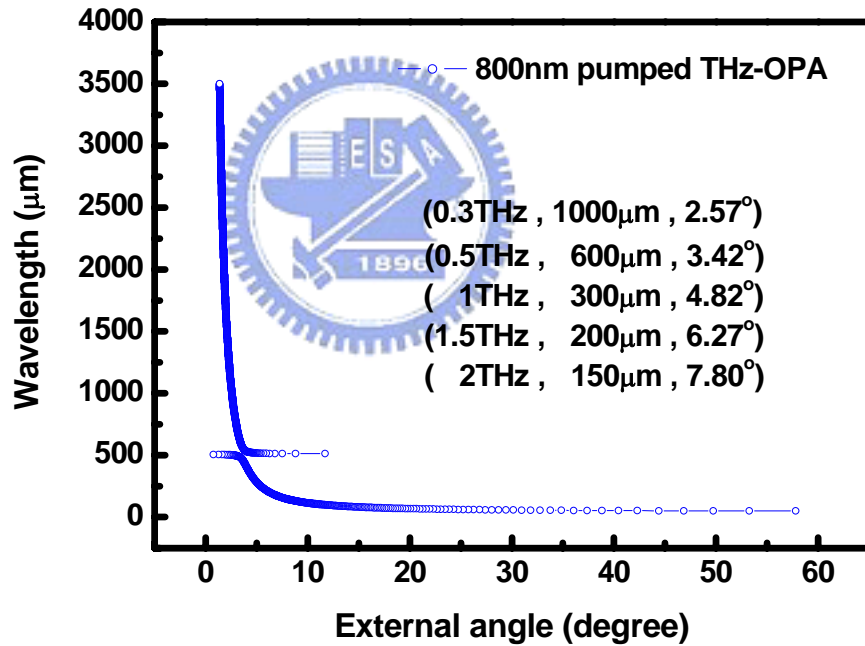


**Fig. 6-2** Seeding wavelength versus corresponding external phase matching angle.

In this OPA process, the wavelength of pump pulse is 800 nm, seeding pulse is at terahertz frequencies. In the terahertz region, we choose type-I ( $e_s + e_i \rightarrow o_p$ ) phase matching condition with collinear type OPA scheme, in which pump pulse is ordinary wave and both of signal and idler are extraordinary waves. In addition, the effective nonlinear coefficient  $d_{eff}$  of the GaSe crystal is given by



$$d_{eff} = d_{22} \cos^2 \theta \cos 3\varphi \quad (9)$$

In order to perform higher efficiency, we can set  $|\cos 3\varphi|=1$  to optimize the effective nonlinearity  $d_{eff}$ . The azimuthal angle  $\varphi$  could be selected as  $0^\circ$ ,  $60^\circ$  and  $120^\circ$ . Under the energy and momentum conservation conditions, the external phase matching angle tuning curve could be deduced, as shown in Fig. 6-2.

### 6.2.3 Experimental setup

Figure 6-3 presents the THz-OPA experimental setup. It consists of two parts, including the THz-TDS stage and OPA stage.

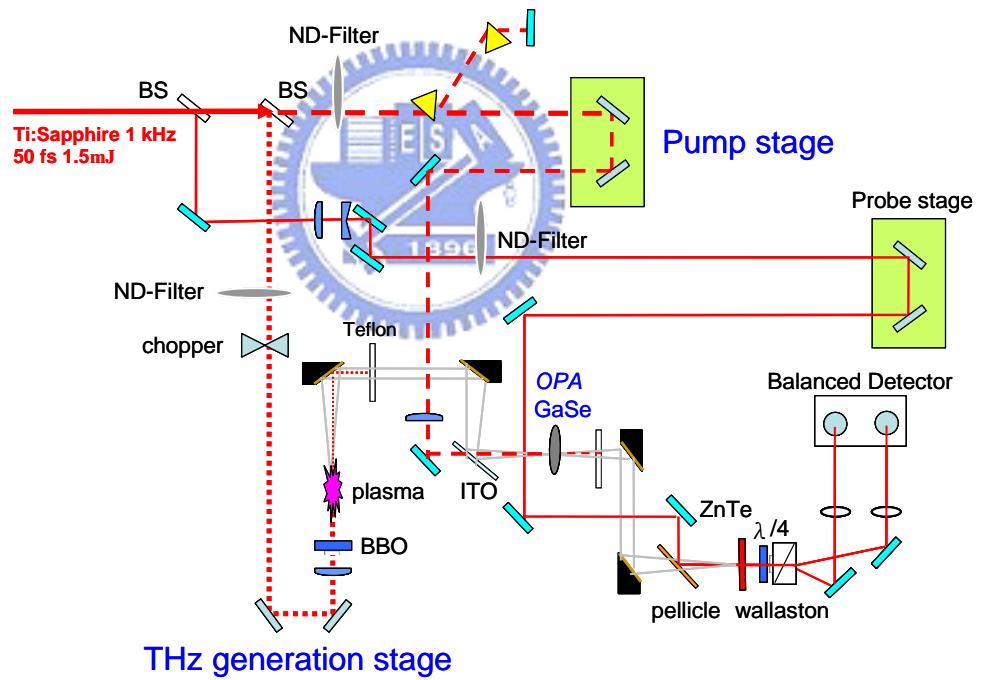


**Fig. 6-3** The experimental setup of THz-OPA.

The regenerated amplified laser is utilized as the laser source with pulse energies of 1.5 mJ and pulse duration 50 fs. The terahertz wave is generated through four wave mixing method in ionized plasma which formed by focusing the fundamental and second-harmonic of the laser pulse. The pump laser beam is adjusted for vertical polarized. The THz output

characteristics including the time domain waveform and spectral profile is shown in Fig. 6-4. The wire-grid polarizer is used to select the suitable polarization (*e-ray*) for the phase matching condition requirement in the subsequent THz-OPA process.

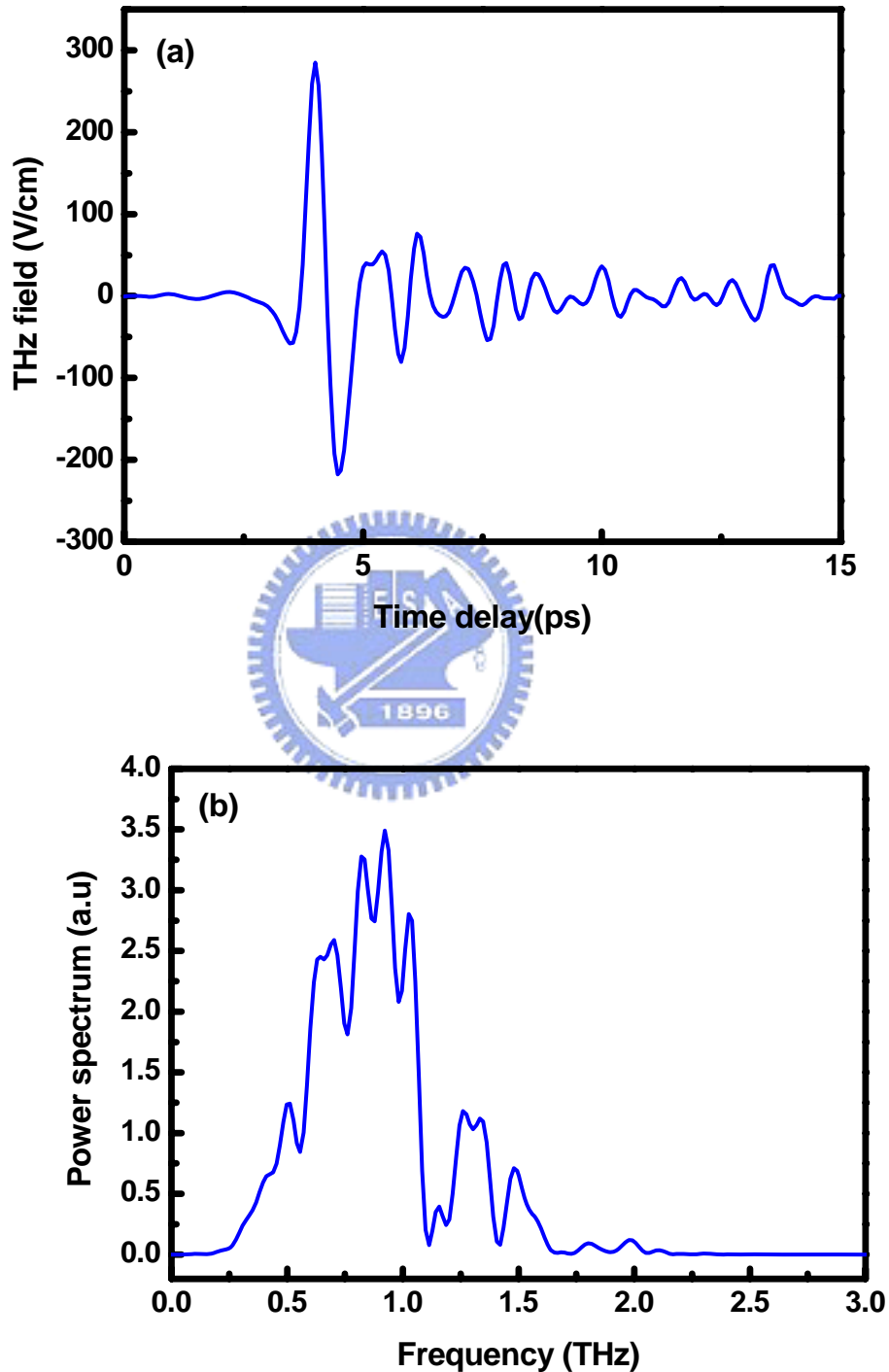


**Fig. 6-4** THz generation by use of the four wave mixing in the plasma (a) THz time domain waveform (b) THz spectrum.

In consideration of the convenient optical alignment, we replace the terahertz emitter from GaSe optical rectification of air nonlinear medium through four-wave mixing. Because the beam, including 800 nm optical beam and terahertz beam, will be converged to a point at the position of OPA-GaSe in this arrangement. The teflon plate is used to block the residual optical laser pulses. The terahertz is detected by EO-sampling with 1 mm thick <110> ZnTe crystal. The balanced detector and lock-in detection technique is applied to increase the signal/noise ratio (SNR).

In order to achieve collinear OPA scheme, the ITO glass plate is used as the beam combiner of optical and THz pulses. The pump beam is adjusted to horizontal polarized to meet the o-ray phase matching for the following THz-OPA process. Moreover, the pulse duration of the femtosecond pumped beam is stretched by prism pairs to approximately 1.5~2 ps, in order to achieve a good temporal overlapping between the optical pumped pulses and THz pulses. Then the optical pump pulses energies are adjusted to be about 220  $\mu\text{J}$  and beam diameter about 3 mm. The optical pump intensity is approximately 2  $\text{GW}/\text{cm}^2$ . Such pump intensity could avoid the free carrier absorption effect, which severely reduced the THz intensity, inside the GaSe crystal. Figure 6-5 displays the autocorrelation trace of the stretching optical pulse by prism pairs.

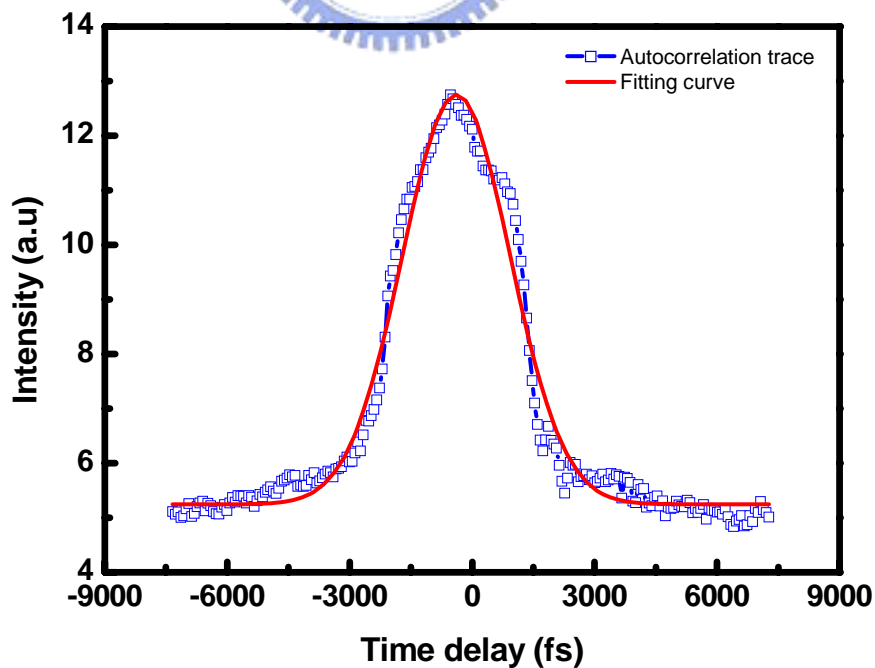


*Fig. 6-5 The autocorrelation trace of optical pump pulses after stretching by prism pairs.*

## 6.3 Results and Discussions

### 6.3.1 The characteristic of THz generation by laser induced plasma by four wave mixing

A 1 kHz Ti: sapphire laser system (Spitfire) at 800 nm with maximum pulse energy of 2 mJ, pulse duration 50 fs is employed herein. We focus the pluses through a 100  $\mu\text{m}$  thick type-I BBO crystal with a 20 cm lens, that has been phase-matched for second harmonic generation (SHG), placed at a variable distance from the focus point. The generated terahertz pulses are detected by free space EO sampling with 1 mm thick ZnTe crystal. Figure 6-4(a) and (b) presents the terahertz time domain waveform and its corresponding frequency domain spectrum, respectively. Then, we rotated the BBO crystal against the beam axis which means varying the angle between fundamental beam ( $\omega$ ) and second harmonic beam ( $2\omega$ ). Figure 6-6 shows the terahertz signal generated by four-wave mixing that is numerically subtracted the signal generated by BBO because the THz signal from BBO will overlaps the signal from plasma. We can see that the maximum signal is deviated about the angle  $\pm 40^\circ$  from the angle of maximum SHG efficiency.

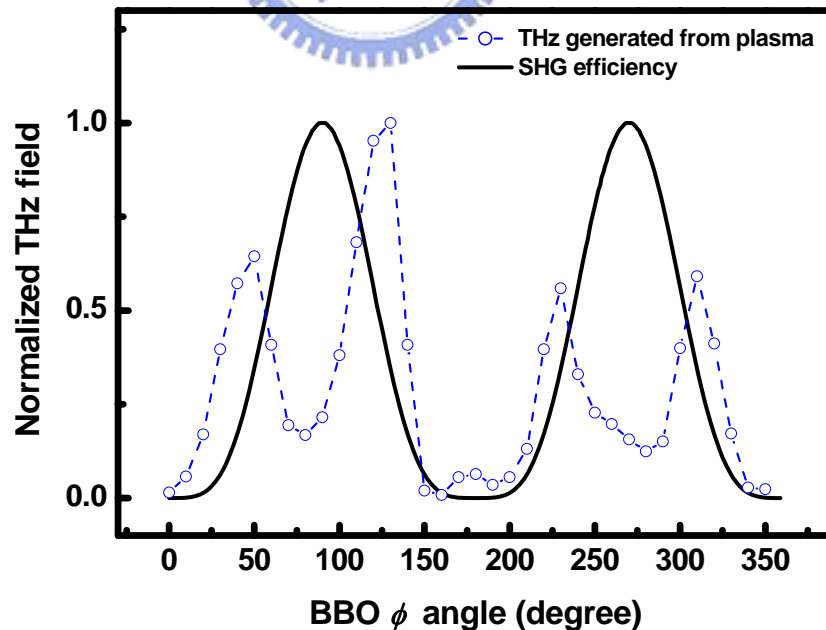


*Fig. 6-6 Terahertz signal from the focus (plasma) as a function of BBO crystal rotation angle.*

Four wave rectification predicts the following dependence of the maximal THz amplitude on relative phase  $\varphi$  between  $\omega$  and  $2\omega$  waves. The generated THz signal is also proportional to the third order nonlinearity, electric field amplitude of second harmonic wave, the square of electric field amplitude of fundamental wave:

$$E_{THz} \propto \chi^{(3)} E_{2\omega} E_{\omega}^2 \cos(\varphi) \quad (10)$$

We can change the phase by varying the distance  $d$  between BBO and the focus point. The phase shift  $\varphi$  is given by

$$\varphi = k_{2\omega}(n_{2\omega} - n_{\omega})d \quad (11)$$

where  $n_{2\omega}$  and  $n_{\omega}$  are the refractive index of air at the frequency  $\omega$  and  $2\omega$ .

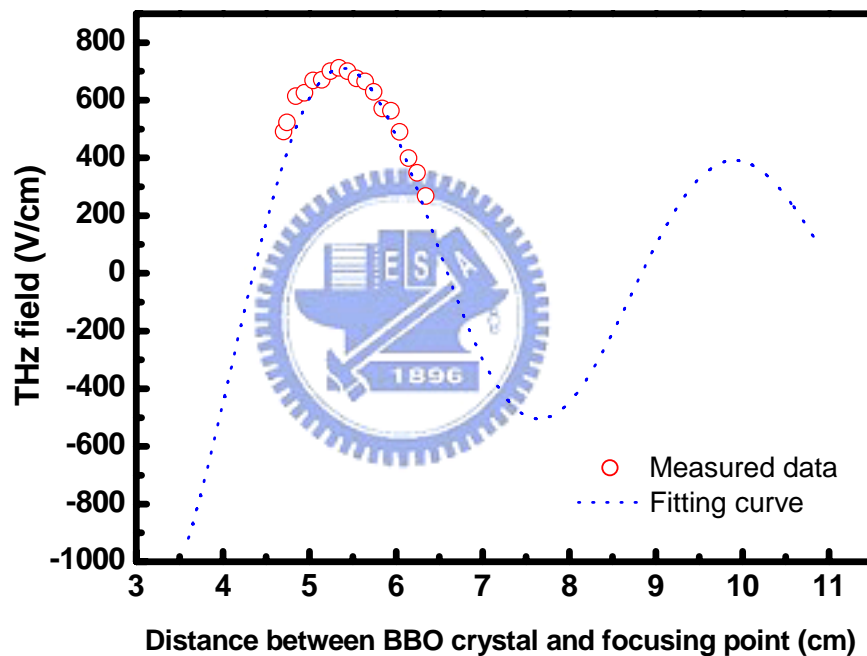


**Fig. 6-7** *Terahertz amplitude versus BBO-to-focus distance.*

Figure 6-7 presents that terahertz amplitude is varied by adjusting the distance from BBO to focus point. One can clearly observe phase-change-induced oscillations as expected from theory (dot-curve). The linear decrease of the envelope arises from the change of the SHG conversion efficiency because of the change in the beam spot size in the BBO crystal. The moving range only from 4.9 to 6.3 cm is due to the damage threshold of BBO and its dimension area. The pump beam size is larger than BBO dimension area when the distance

is larger than 6.4 cm, and close to the damage threshold of BBO crystal when the distance less than 4.9 cm. Changing the distance  $d$  is not only altering the relative phase but also changing the SHG efficiency and the beam spot size on the BBO crystal. The SHG power conversion efficiency is given by [18]

$$\eta_{SHG} = \tanh^2\left(\frac{1}{2}\kappa A_1(0)z\right) \quad (12)$$

where  $\kappa = (\omega/n)^{3/2} \sqrt{2(\mu_0/\epsilon_0)d}$  is the phase mismatch. And we can derive that

$$E_{THz} \propto \cos(\varphi) \tanh\left(\frac{1}{d}\right) \quad (13)$$

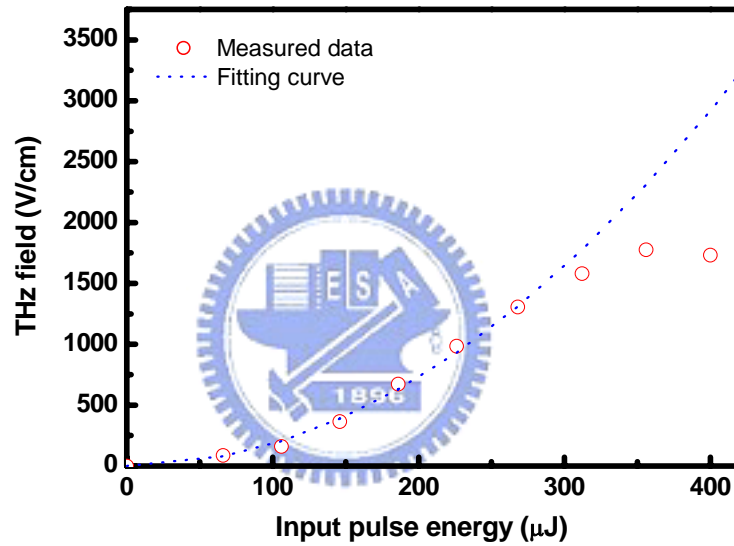


**Fig. 6-8** Terahertz amplitude versus laser pulse energy.

We measured the THz signal intensity with varying the laser pulse energy before the BBO crystal. The results are shown in Fig. 6-8, while BBO was set at the angle position that has maximum THz output and the distance  $d=5.34$  cm. By using the relation

$$E_{2\omega} \propto E_{\omega}^2 \propto I_{\omega} \quad (14)$$

Eq. (10) has the quadratic dependence

$$E_{THz} \propto \chi^{(3)} I_{\omega}^2 \quad (15)$$

The pulse energy below 300  $\mu\text{J}$  can be fitted well with Eq. (15), but the THz signal falls below the fitted quadratic curve in the higher pulse energies portion. It may be likely due to

the defocusing of the laser beam by the plasma and reduces the effective peak intensity. In addition, at larger plasma volumes, phase mismatch and THz absorption effects by free carriers could more likely be significant [18].

### 6.3.2 GaSe crystal length determination by GVM

Group velocity mismatch (GVM) between the pump beam and the signal and (idler) beam will limit the interaction length over which parametric amplification. By calculating GVM, we can quantify interaction length by the pulse splitting length, Eq. (16).

$$L_{jp} = \frac{\tau}{\delta_{jp}}, j = s, i \quad (16)$$

where  $\tau$  is the pump pulse duration,  $\delta_{jp} = 1/v_{gi} - 1/v_{gp}$  is the group velocity mismatch between signal/idler pulses and pump pulse. In this work, the wavelength of optical pump pulse is at 800 nm. The corresponding GVM are  $\delta_{ip} = 528.6$  fs/mm for idler wavelength (THz) is at 300  $\mu\text{m}$ ;  $\delta_{sp} = -9.5$  fs/mm for signal wavelength is at 802 nm. Accordingly, the selected GaSe crystal length is about 3 mm for optical pump pulse duration 1.5 ps.

### 6.3.3 Pump depleted gain prediction by taking account of the linear and nonlinear absorption

The output of the terahertz signal after the THz-OPA system can be explained by the parametric amplification process under a depleted pump beam condition [19]:

$$I_i(r) = \left[ \left( \frac{\omega_i}{\omega_p} \right) I_p (1 - \text{sn}^2[(r - r_0)/l, r]) \right] \times \exp(-\alpha r) \quad (17)$$

where

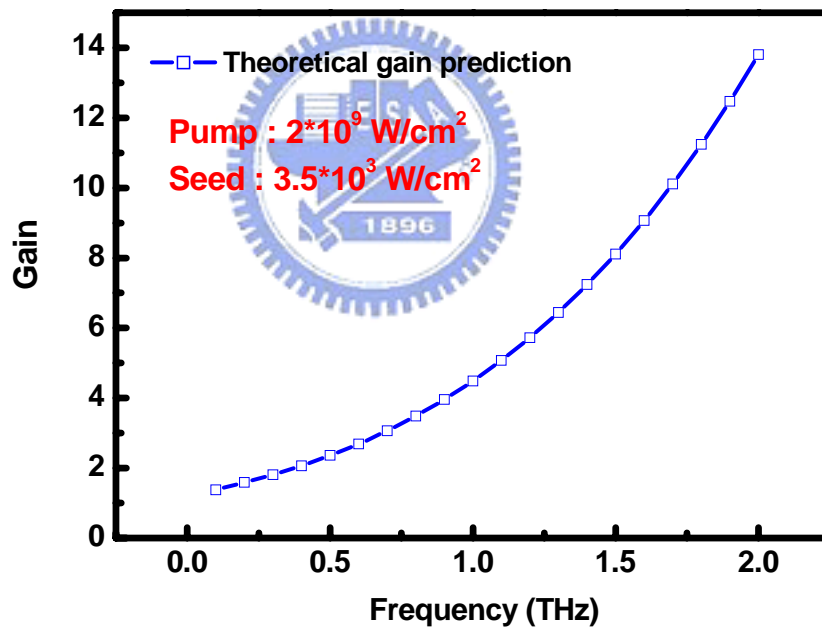
$$1/l = \Gamma(\lambda) \sqrt{1 + \frac{I_s \omega_p}{I_p \omega_s}} \quad (18)$$



and

$$r_0 / l = \frac{1}{2} \ln(16[1 + \frac{I_p \omega_s}{I_s \omega_p}]) \quad (19)$$

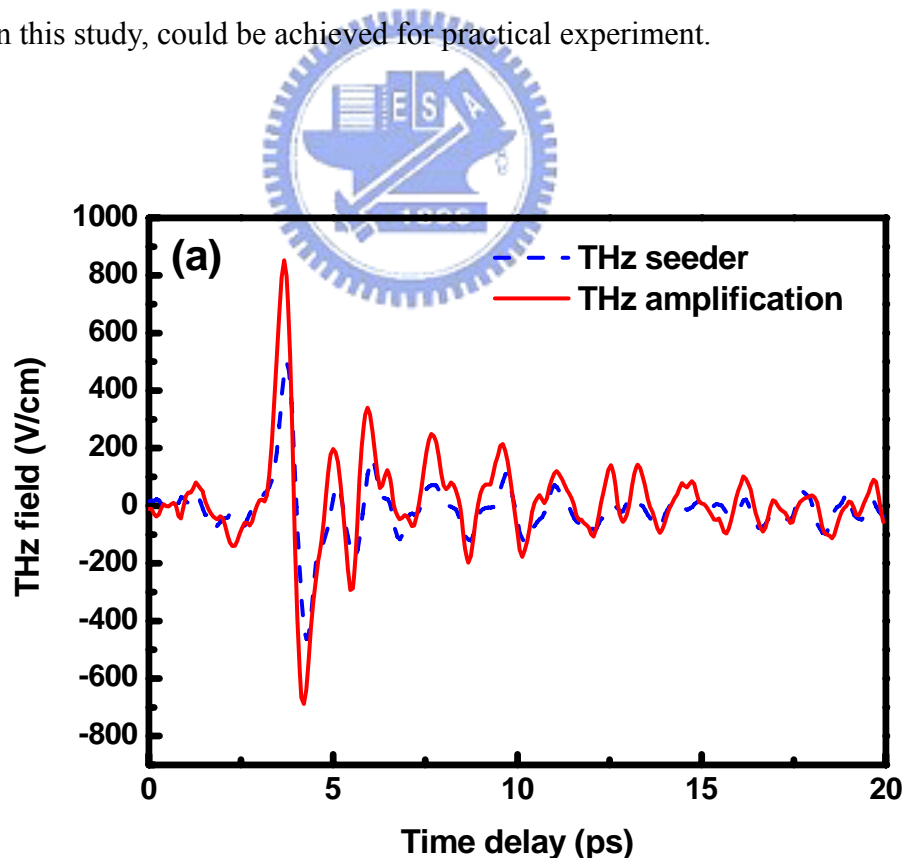
In Eqs. (17)-(19),  $I_p$  is the pump intensity;  $I_s$  is the seeding THz intensity;  $\Gamma(\lambda)$  is the parametric gain coefficient;  $\alpha$  is the absorption coefficient, which includes the linear and nonlinear absorption;  $\omega_j, j=p, s, \text{ or } i$  is the angular frequency of the pump, the signal and the idler pulses (THz wave), respectively;  $r$  is length of the GaSe crystal. We note that  $sn$  in Eq. (17) is the Jacobian elliptic function resulting from an inversion operation of the elliptic integral [19]. From the calculating results, the net gain could be expected. For instance, the pump/seeding THz intensity are set as  $2 \times 10^9 \text{ W/cm}^2$  and  $3.5 \times 10^3 \text{ W/cm}^2$ , respectively, in the calculations. Consequently, the power amplification gain magnitude could reach as high as approximately 4.5 for the central frequency located at 1 THz. The prediction gain profile is shown in Fig. 6-9.



**Fig. 6-9** Theoretical gain prediction in this THz-OPA system.

### 6.3.4 THz amplification experimental achievement

The GaSe external phase matching angles is set  $3^{\circ}\sim 5^{\circ}$ , which corresponds to the phase matching wavelength  $300\sim 1000\ \mu\text{m}$  ( $0.3\ \text{THz} \sim 1\ \text{THz}$ ). For THz-OPA system, the seeding THz time domain profile is shown as the black-line in the Fig. 6-10(a). Then the THz output signal after amplification is depicted as the red-line. Figure 6-10(b) presents the seeded and amplified THz spectrum profile. The weak THz signal can be power amplified as 2.7 times respect to the input THz signal. The experimental achievement of the power amplification gain is a little lower than that calculated from the theoretical prediction. It is likely attributed to the imperfect phase matching and the beams overlap between the optical pump and the THz seed. Besides, the gain calculation method mentioned in Section 6.3.3 is under the plane wave assumption of the THz radiation. Therefore, the predictional gain factors for every frequency components satisfy the perfect phase-matching condition. The magnitude of the gain factor might be over-estimated. Therefore, the theoretical prediction of the gain factor is even up to 4.5 at central frequency 1 THz, the lower magnitude of the gain factor, 2.7 times in this study, could be achieved for practical experiment.



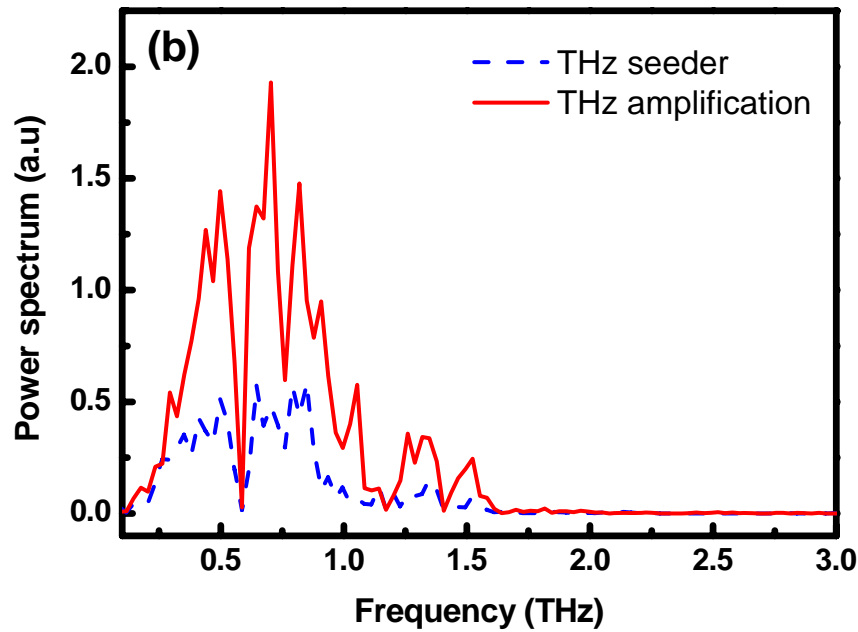


*Fig. 6-10 THz amplification by OPA process (a) THz time domain waveform (b) THz spectrum.*

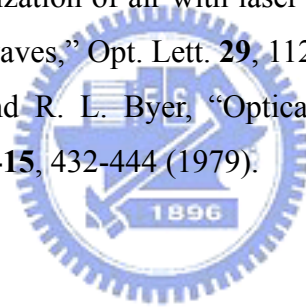
## 6.4 Summary

Femtosecond laser induced plasma in ambient air based on the third order nonlinearity is employed to construct a THz-TDS system in this study. The properties of the THz radiation from this configuration is characterized by altering the phase shift, the angle between polarizations of the fundamental (800 nm) and second harmonic beams (400 nm). The dependence of the THz signal as a function of the fundamental pulse energy before the BBO crystal is also examined. Furthermore, GaSe crystal is a promising nonlinear optical medium to perform the generation of intense THz radiation. Herein, we report the experimental demonstration of terahertz wave amplification in GaSe crystal. Terahertz power amplification factor of about 2.7 times is preliminarily performed under the phase matching condition around 1 THz. The demonstration provides a potential way to further increase the terahertz electric field for nonlinear spectroscopic applications with a desktop femtosecond laser system.

## References

- [1] P. Y. Han, X. -C. Zhang, "Free-space coherent broadband terahertz time-domain spectroscopy," *Meas. Sci. Tech.* **12**, 1747-1756 (2001).
- [2] G. M. H. Knippels, X. Yan, A. M. MacLeod, W. A. Gillespie, M. Yasumoto, D. Oepts, and A. F. G. van der Meer, "Generation and Complete Electric-Field Characterization of Intense Ultrashort Tunable Far-Infrared Laser Pulses," *Phys. Rev. Lett.* **83**, 1578-1581 (1999).
- [3] G. L. Carr, M. C. Martin, W. R. McKinney, K. Jordan, G. R. Neil, G. P. Williams, "High-power terahertz radiation from relativistic electrons," *Nature* **420**, 153-156 (2002).
- [4] W. P. Leemans, C. G. R. Geddes, J. Faure, Cs. Toth, J. van Tilborg, C. B. Schroeder, E. Esarey, G. Fubiani, D. Auerbach, B. Marcellis, M. A. Carnahan, R. A. Kaindl, J. Byrd, and M. C. Martin, "Observation of terahertz emission from a laser-plasma accelerated electron bunch crossing a plasma-vacuum boundary," *Phys. Rev. Lett.* **91**, 074802-1-4 (2003).
- [5] E. Budiarto, J. Margolies, S. Jeong, J. Son, and J. Bokor, "High-intensity terahertz pulses at 1-kHz repetition rate," *IEEE J. Quantum Electron.* **32**, 1839-1846 (1996).
- [6] G. Zhao, R. N. Schouten, N. van der Valk, W. T. Wenckebach, and P. C. M. Planken, "Design and performance of a THz emission and detection setup based on a semi-insulating GaAs emitter," *Rev. Sci. Instrum.* **73**, 1715-1719 (2002).
- [7] K. Reimann, R. P. Smith, A. M. Weiner, T. Elsaesser, and M. Woerner, "Direct field-resolved detection of terahertz transients with amplitudes of megavolts per centimeter," *Opt. Lett.* **28**, 471-473 (2003).
- [8] J. Hebling, G. Almasi, I. Z. Kozma, and J. Kuhl, "Velocity matching by pulse front tilting for largearea THz-pulse generation," *Opt. Express* **10**, 1161-1166 (2002).
- [9] A. G. Stepanov, J. Hebling, and J. Kuhl, "Efficient generation of subpicosecond terahertz radiation by phase-matched optical rectification using ultrashort laser pulses with tilted pulse fronts," *Appl. Phys. Lett.* **83**, 3000-3002 (2003).
- [10] J. Hebling, A. G. Stepanov, G. Almasi, B. Bartal, and J. Kuhl, "Tunable THz pulse generation by optical rectification of ultrashort laser pulses with tilted pulse fronts" *Appl. Phys. B: Lasers Opt.* **78**, 593-599 (2004).
- [11] A. G. Stepanov, J. Kuhl, I. Z. Kozma, E. Riedle, G. Almasi, and J. Hebling, "Scaling up the energy of THz pulses created by optical rectification," *Opt. Express* **13**, 5762-5768 (2005).

- [12] K. -L. Yeh, M. C. Hoffmann, J. Hebling, and K. A. Nelson, "Generation of 10  $\mu$ J ultrashort terahertz pulses by optical rectification," *Appl. Phys. Lett.* **90**, 171121-1-3 (2007).
- [13] T. Bartel, P. Gaal, K. Reimann, M. Woerner, and T. Elsaesser, "Generation of single-cycle THz transients with high electric-field amplitudes," *Opt. Lett.* **30**, 2805-2807 (2005).
- [14] J. Dai, X. Xie, and X. -C. Zhang, "Terahertz wave amplification in gases with the excitation of femtosecond laser pulses," *Appl. Phys. Lett.* **91**, 211102-1-3 (2007).
- [15] G. Cerullo and S. D. Silvestri, "Ultrafast optical parametric amplifiers," *Rev. Sci. Instrum.* **74**, 1-18 (2003).
- [16] V. G. Dmitriev, G. G. Gurzadyan, and D. N. Nikogosyan, *Handbook of Nonlinear Optical Crystals* (Springer, Berlin, 1997).
- [17] W. Koechner, *Solid-State Laser Engineering*, 4th ed. (Springer, Berlin, 1996)
- [18] M. Kress, T. Löffler, S. Eden, M. Thomson, and H. G. Roskos, "Terahertz-pulse generation by photoionization of air with laser pulses composed of both fundamental and second-harmonic waves," *Opt. Lett.* **29**, 1120-1122 (2004).
- [19] R. A. Baumgartner and R. L. Byer, "Optical parametric amplification," *IEEE J. Quantum Electron.* **QE-15**, 432-444 (1979).



## Chapter 7

### Conclusions and future works

The optical constants of a GaSe crystal are measured by the terahertz time-domain spectroscopy at terahertz frequencies. Based on experimental data, a modified complex ordinary and extraordinary dielectric function of GaSe is presented. A low-frequency rigid-layer phonon mode at 0.586 THz confirms the pure GaSe crystal to be in the  $\epsilon$ -phase. The transverse and longitudinal optical phonons in the reststrahlen band for the ordinary refraction index are experimentally determined to be 6.39 and 7.62 THz, respectively.

The infrared-active modes of  $\epsilon$ -GaSe crystal at  $237.0\text{ cm}^{-1}$  and  $213.5\text{ cm}^{-1}$  were found to be responsible for the observed optical dispersion and infrared absorption edge. Based upon phase matching characteristics of GaSe for difference-frequency generation (DFG), new Sellmeier equations of GaSe were proposed. The output power variation with wavelength can be properly explained with the shape of parametric gain and the spectral profile of absorption coefficient of GaSe. The adverse effect of infrared absorption on (DFG) process can partially be compensated by doping GaSe crystal with erbium ions.

We propose and experimentally demonstrate the generation of single-cycle terahertz radiation with two-stage optical rectification in GaSe crystals. By adjusting the time delay between the pump pulses employed to excite the two stages, the terahertz radiation from the second GaSe crystal can constructively superpose with the seeding terahertz field from the first stage. The high mutual coherence between the two terahertz radiation fields is ensured with the coherent optical rectification process and can be further used to synthesize a desired spectral profile of output coherent THz radiation.

A THz-TDS system based on laser induced plasma in ambient air is also constructed in this study. A THz amplification process could be achieved by optical parametric amplification technique. High gain can be performed under the theoretical calculation. Herein, we report the experimental demonstration of terahertz wave amplification in GaSe crystal. Terahertz power amplification factor of about 2.7 times is preliminarily performed under the phase matching condition around 1 THz. The demonstration provides a potential way to further increase the terahertz electric field for nonlinear spectroscopic applications with a desktop femtosecond laser system.

The recommendation in future work is represented as follows:

In this dissertation, the generation of mid- to far-infrared radiation has been performed by use of the GaSe crystal. Especially, the severe effect of the free carriers has been identified to reduce the output and performance of the THz emission systems, including the multiple-stage optical rectification and terahertz parametric amplifier. Therefore, in fundamental, the elimination of the intrinsic nonlinear absorption of the free carrier is the important issue to study. If the concentration of free carriers could be reduced, the performance of the high-power terahertz producer must be improved. The intense terahertz light source can be expected.

In practice, it could be devoted to perform the terahertz phase modulator. The external angles of the optical axis of the GaSe crystal between the direction of incident terahertz light are as a function of the phase shift. This relationship could be further determined for the convenient application to the scientists.

A simple calculation and design has been done for the prediction of the maximum energy output of the terahertz radiation from the multiple stage optical rectification system. In photon factory (NCTU), the Spitfire could be operated under 10 Hz repetition rate, 800 nm central wavelength, 50 fs. The laser pulse energy could be as high as 15 mJ. After the theoretical calculation, a design case is preliminately proposed to achieve the maximum terahertz output from this technique:

The total laser pulse energy is divided to three parts for the three-stage optical rectifications. The pulse duration is stretched to 280 fs, focusing spot size is about 7mm, and the GaSe crystal length is 570  $\mu\text{m}$  for each stage. The conversion efficiency for each stage is about  $\sim 2 \times 10^{-5}$ . After the coherent superposition of terahertz electric fields in the time domain, the intense single-cycle terahertz pulse could be yielded. Therefore, in our prediction, the maximum pulse energy of terahertz radiation output by means of the multiple stage optical rectification is as high as 300 nJ.